UNIVERSITÀ
DEGLI STUDI
DI PADOVA

Sede Amministrativa: Università degli Studi di Padova
Sede Consorziata: Università degli Studi di Roma “SAPIENZA”

Dipartimento di: Ingegneria Meccanica e Aerospaziale

SCUOLA DI DOTTORATO DI RICERCA IN : Scienze tecnologie e misure spaziali
INDIRIZZO: Misure meccaniche per l’ingegneria e lo spazio (MMIS)
CICLO XXV

Qualitative analysis of a microtomographic apparatus and measurement of the bone tissue density with reference to microgravity conditions

Direttore della Scuola : Ch.mo Prof. Giampiero Naletto
Coordinatore d’indirizzo: Ch.mo Prof. Stefano Debei
Supervisore : Ch.mo Prof. Paolo Cappa
Co-Supervisore : Ch.mo Prof. Franco Marinozzi

Dottorando : Francesca Zuppante

CONTENTS

List of tables

ABSTRACT

Computed Thomography is a relatively new field in the area of non destructive imaging. It allows to reconstruct the internal structure of opaque objects without destroy them. This is a great advantage compared to conventional microscopy techniques, any optical or electronic microscope, in fact, provides information on the internal structure of samples only if samples are properly processed and sectioned. Information about three-dimensional structure could be obtained by the image of a surface or a combination of several thin slices, but in both cases information cannot be certain since methods of cutting and preparation can dramatically change the structure of the sample. Microcomputed tomography, commonly referred to as μCT, like conventional computed tomography is based on the collection of projections of X rays through a specimen and the application of tomographic principles to reconstruct the 3-D structure of the specimen. It is based on the interaction of X-rays with matter. The attenuation of X-rays, passing through an object, is dependent on the density and atomic number of the object under investigation. This radiation is converted in a radiographic image of the object. Images obtained from different angles are analyzed by an algorithm called Filter back projection in order to reconstruct a virtual slice through the object. When different consecutive slices are reconstructed, a 3D visualization can be obtained.

The term "micro" denotes a scanning system much higher in resolution than conventional clinical scanners. Clinical tomographic scanners may have resolutions on the order of a millimeter or less. However, high-resolution μCT scanners may have resolutions below five microns.

The high resolution of this system makes it useful in the analysis of small objects such as trabecular bone samples. Trabecular bone consists of a complicated three-dimensional network of plates and rods, arranged in a lattice-like network. The architectural parameters of trabecular bone could be strongly influenced by aging or bone diseases such as osteoarthritis or osteoporosis.

Until recently, information about these structural parameters of trabecular bone were only available by histomorphometry, a destructive procedure limited to two-dimensional analysis. Nowadays Micro-CT, because of its capability to allow three-dimensional and non destructive analysis, found large applications in pre-clinical bone research. The increasing incidence and prevalence of bone pathologies on the population, increases the interest of improve an accurate bone characterization by Micro-CT. Micro-CT system, object of this study is the Skyscan 1072,

located at the Technology and Health Department of the Italian National Institute of Health. One of the goal of this research is set at optimizing the system for the analysis of bone samples.

The first part is dedicated on determining the resolution of the system. The performance of an imaging system is usually described by the measurement of its Modulation Transfer Function or MTF which gives a description of how much contrast at a specific spatial frequency is maintained by the imaging process. The second part of this study is focused on the process of images reconstruction, fundamental in a Micro-CT analysis. Micro-CT images are affected by several artifacts which will be widely discussed in the following chapters. One of the most difficult artifact is beam hardening. It depends on the polychromatic X-ray tube used in these systems. The X-rays beam investing the sample is composed of X-rays with a spectrum of different energies. The attenuation of an X-ray depends on its energy, the lowest X-ray energies are preferentially absorbed. Assuming that the grey level of CT images corresponds to the linear coefficient of attenuation, which is constants depending on the material, because of the beam hardening, the attenuation of a given material is not strictly proportional to its thickness. This implies visual distortions on the images and the consequent origin of quantitative problems. In order to better understand the effect of beam hardening on Micro-CT images, the filtered back projection algorithm will be implemented in LabVIEW (Version 8.2). The Skyscan 1072 allows to correct the effect of beam hardening during the process of images reconstruction by the definition of a proper parameter. In order to define the correct value of this parameter for a bone sample analysis, a comparison between the results of both the algorithm implemented and the Skyscan reconstruction software will be evaluated.

After the optimization of the system for bone analysis, nineteen trabecular bone samples, extracted from femoral heads of eight patients subject to a hip arthroplasty surgery, will be analyzed. The main problem of bone analysis by micro-CT is the processing of the reconstructed cross-sections images for the sample morphometric analysis. The post-processing of the images for the morphometric characterization usually requires a process named binarization of the images which consists on the definition of a threshold value of grey-level, necessary to distinguish bone from background. The choice of this value is a crucial task since a standard method doesn’t exist. Moreover, the inhomogeneity of bone causes another problem during the binarization process. Binarization associates each pixel of the image to bone or air, not considering that each pixel can be composed by both of them. This effect is called Partial Volume Effect and it affects especially pixels at the edges of the analyzed sample. In order to avoid problems related to the binarization, the main goal of this study is the evaluation of a new

method for the histomorphometric analysis of bone sample from the direct processing of the grey level histogram of the images.

Finally, the last part of this research will be dedicated on the remodeling process of bone. The remodeling of bone is an important research topic because of its importance in the study of bone pathologies such as osteoporosis. Osteoporosis is a bone disorder characterized by an inadequate amount and faulty structure of bone, resulting in fractures from relatively minor trauma. It leads to a bone mineral density (BMD) reduction, a bone microarchitecture deterioration and an alteration of the amount and variety of proteins in bone. Aging is the main factor of osteoporosis incidence but in the last years, another factor related to long-duration spaceflight, has been considered. Because of the difficult in reproducing in-vivo space conditions, the development of numerical models is a good alternative for the remodeling process study.

SOMMARIO

La Tomografia Computerizzata è una nuova tecnica di imaging che consente la ricostruzione e l'analisi della struttura interna di oggetti opachi senza che questi vengano in alcun modo danneggiati. La possibilità di analizzare campioni senza modificarli o danneggiarli conferisce a questa nuova tecnica un grande vantaggio rispetto alle tecniche di microscopia tradizionale. I microscopi ottici ed elettronici infatti, consentono di ottenere informazioni tridimensionali sulla struttura interna dei campioni analizzati ma l'opportuna preparazione dei campioni richiesta può modificarne drammaticamente la struttura interna. La Micro Tomografia Computerizzata ha lo stesso principio di funzionamento della tradizionale Tomografia Computerizzata, una corretta analisi delle proiezioni del fascio di raggi X ottenute dall'attraversamento del campione e l'applicazione dei principi base di tomografia consentono di ottenere la struttura tridimensionale dell'oggetto in esame. Attraversando la materia, il fascio di raggi X subisce un'attenuazione proporzionale alla densità e al numero atomico del materiale attraversato. La radiazione attenuata è convertita in livelli di grigio nelle corrispondenti immagini radiografiche generate. Il campione viene investito dal fascio di raggi X secondo diverse angolazioni in modo tale che il successivo processamento delle proiezioni con opportuni algoritmi permetta la corretta ricostruzione della struttura tridimensionale dell'oggetto. Il termine "micro" sta ad indicare l'elevata risoluzione del sistema microtomografico. Mentre la Tomografia tradizionale permette di raggiungere risoluzioni massime dell'ordine del millimetro, la microtomografia consente di raggiungere risoluzioni molto minori, dell'ordine dei micron. Questa caratteristica rende la microtomografia adatta all'analisi di oggetti di piccole dimensioni, quali ad esempio campioni di osso trabecolare in cui le dimensioni medie delle trabecole sono paragonabili alla risoluzione del sistema. L'elevata incidenza sulla popolazione mondiale di patologie ossee, come ad esempio l'osteoartrite o l'osteoporosi, hanno spinto molti ricercatori ad approfondire la possibilità di ottenere un'accurata caratterizzazione ossea tramite l'utilizzo della microtomografia. Il microtomografo utilizzato in questa ricerca è lo Skyscan 1072, presente presso il Dipartimento di Tecnologia e Salute dell'Istituto Superiore di Sanità.

Il primo obiettivo di questa ricerca sarà uno studio approndito del microtomografo a disposizione al fine di ottimizzarne l'utilizzo per l'analisi di campioni ossei. Come prima analisi si misurerà la risoluzione dello Skyscan 1072. La valutazione delle performance di sistemi per acquisizioni di immagini può essere valutata con il calcolo della Funzione di Trasferimento della Modulazione (MTF) dello strumento. La MTF descrive in modo completo la perdita di informazione nel processo che va dall'acquisizione alla visualizzazione dell'immagine al

diminuire delle dimensioni dell'oggetto indagato. Essa definisce la relazione tra la risoluzione di contrasto e la risoluzione spaziale del sistema. La seconda parte di questo studio preliminare sarà focalizzata sul processo di ricostruzione delle immagini. La ricostruzione delle immagini è uno step fondamentale nell'analisi microtomografica. E' noto che le immagini provenienti da questo tipo di analisi sono affette da artefatti di diversa origine. Uno degli artefatti più dannosi e anche più difficile da rimuovere è il beam hardening. Il fascio di radiazione X che investe il campione è solitamente un fascio policromatico ovvero composto da raggi X di diversa energia. Nell'attraversare l'oggetto, i raggi con energia maggiore sono meno attenuati rispetto ai raggi di minore energia e quindi viene rilevato un valore dell'attenuazione tanto minore quanto maggiore è lo spessore del materiale attraversato. La presenza del beam hardening causa distorsioni nelle immagini create e conseguenti errori nell'analisi quantitativa delle stesse. Al fine di capire l'effetto di questo artefatto sulle immagini e correggerlo al meglio per l'analisi di campioni ossei, l'algoritmo di retroproiezione filtrata, comunemente utilizzato per la ricostruzione di immagini tomografiche, verrà implementato in LabVIEW (Version 8.2).

Uno dei principali problemi dell'analisi microtomografica di campioni ossei è il post-processing delle immagini per la valutazione dei parametri istomorfometrici. I programmi generalmente utilizzati richiedono una previa binarizzazione delle immagini. La binarizzazione richiede la definizione di un valore di soglia dei livelli di grigi al fine di evidenziare gli oggetti ossei nell'immagine. La scelta di questo valore è un argomento di ricerca tutt'ora aperto e non esiste un metodo standard per la sua definizione. Il processo di binarizzazione introduce un ulteriore problema relativo alla definizione dei bordi degli oggetti nell'immagine. Binarizzare significa associare ogni pixel a osso o non-osso, non considerando che alcuni pixel, specialmente quelli relativi al bordo di un oggetto, non sono facilmente associabili a una delle due classi.

Al fine di eliminare il problema della binarizzazione sopra esposto, l'obiettivo principale di questa ricerca sarà lo sviluppo di un nuovo metodo per l'analisi istomorfometrica delle ossa, basato sull'analisi diretta dell'istogramma dei livelli di grigi dell'immagine.

L'ultima parte della ricerca sarà dedicata al processo di rimodellamento delle ossa. Capire come l'osso reagisce ai carichi esterni è molto importante in quanto consente di avere maggiori informazioni nello studio delle patologie ossee, quali ad esempio l' osteoporosi. L'osteoporosi è una patologia ossea caratterizzata da una perdita di massa ossea e resistenza causata da fattori nutrizionali, metabolici o patologici. Lo scheletro è soggetto ad un maggiore rischio di fratture patologiche, in seguito alla diminuzione di densità ossea e alle modificazioni della microarchitettura delle ossa. L'invecchiamento, nonostante sia il principale fattore di incidenza di

questa patologia, non è l'unico. Negli ultimi anni, si è posta particolare attenzione all'elevata percentuale di insorgenza di questa malattia in soggetti che hanno partecipato a missioni spaziali di lunga durata. In condizioni di microgravità, il tessuto osseo, non essendo sollecitato da carichi esterni, va incontro ad aumento del catabolismo e perde l'1- 2% del calcio totale dopo solo qualche settimana di microgravità. Non è semplice riprodurre queste condizioni in esperimenti in-vivo, una possibile alternativa è lo sviluppo di modelli numerici per la simulazione del processo di rimodellamento osseo.

CHAPTER 1

Bone anatomy and physiopathology

1.1. Bone tissue

Bone tissue is, as cartilage, a connective tissue specialized in the support of the human body. Mineralization is one of the peculiarity of the bone tissue since the intercellular matrix is mainly composed of mineral crystals like calcium phosphate. The presence of minerals, as well as the abundance and the particular distribution of the organic components of the intercellular matrix, gives this tissue high mechanical properties. The high resistance to pressure, tensile and torsion, makes this tissue an ideal material for bones formation, which are the support structure of the organism. Moreover, because of the high content of calcium salts, bone tissue represents the main deposit of calcium ion for the metabolic needs of the whole organism[1].

1.2. Architectural organization of bone tissue

Depending on the size and the arrangement of the collagen fibers, two varieties of bone tissue can be define, fibrous and lamellar bone tissue. The first one is characterized by the presence of collagen fibers of significant size which are interwoven in all directions. Fibrous bone tissue is firstly deposed during development and repair processes, then it is quickly reabsorbed and replaced with lamellar bone. Instead of the fibrous bone, this second one is composed of fibers of collagen and osteocytes organized in ordered and superimposed layers. These layers form lamellae which, depending on the arrangement, generate two different kind of lamellar tissue, the first one is characterized by a limited number of parallel lamellae, in the other one lamellae are arranged concentrically around a central canal, called Haversian canal, that contains a blood vessel. Each structure composed of Haversian canal and its related lamellae is named osteon and it is the basic unit of the lamellar tissue. Osteons are organized to lie along lines of mechanical

stress, and an alteration of stress patterns in living bone results in a realignment of osteons, a unique and adaptive property of bone known as Wolff's law. Bone is also composed of lacunae, small cavities of the bone mineral matrix that contain osteocytes. Lacunae are interconnected by thread-like canals termed canaliculi. Lacunae and canaliculi constitute a continuous system of cavity within the bone that allows the metabolic and gas exchanges between the blood flowing in the vessels contained in the tissue and cells. The external and internal surface of bone is surrounded by connective tissue membranes. Externally, it is covered by a thin fibrous layer, named periosteum, which provides for bone nutrition. Blood vessels and nerves reach the tissue flowing through it, so it provides to bone formation during growth and after fractures. A similar thin layer of connective tissue, endosteum, cover the surface of the marrow cavity and trabecular structure of bones.

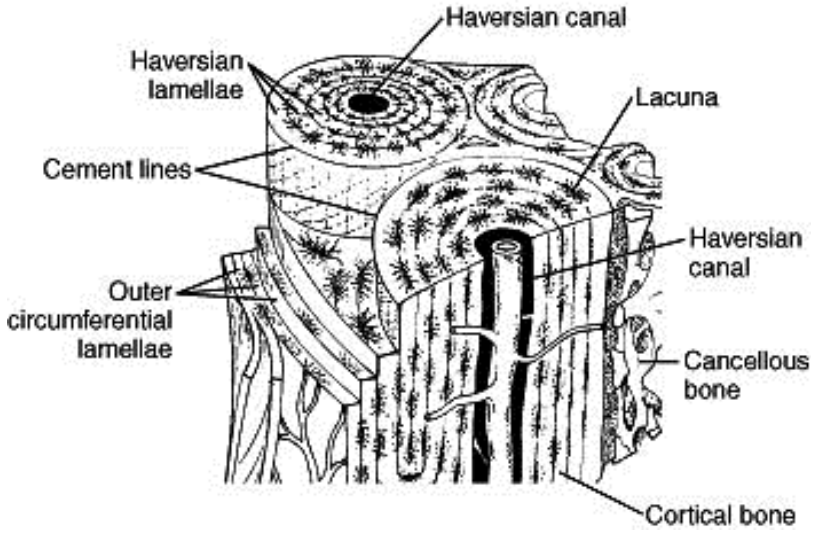

Figure 1. Osteon or lamellar bone: the normal type of adult bone.

1.2.1. Osteon: structural unit of compact bone

Osteon is the basic unit of compact bone, it appears as a long cylindrical structure of about 200-250 μm in diameter, whose longitudinal axis tends to be arranged parallel to the lines of force applied on bone. Thus the femur, which supports the weight of the body and is therefore subject to forces applied in the longitudinal direction, is mainly composed of osteons arranged parallel to its major axis. Similarly, osteons tend to arrange parallel to each other in the skeletal parts where tension forces are dominant.

Osteons are independent functional units, their cells feed from the blood vessel in the Havers channel so the process of bone reabsorption involving an osteon, influences only marginally

neighbors osteons. However, blood vessels of contiguous osteons are linked by branches which run perpendicularly to the Haversian canals in canals called Volkmann canals.

During remodeling processes which bone is continuously subjected, preexisting osteons can be reabsorbed, in whole or in part, and in the formed cavities, new osteons are deposed. Gaps between adjacent osteons are therefore occupied by portions of previous osteons which are the remains of previous reabsorption. These gaps are called interstitial system[2]. Osteons and the interstitial system are limited by thin sheets, called *cement lines*. The outer and inner surface of mature bone is limited by a thin layer of simple lamellar bone, composed of some parallel lamellae, which severally constitute the outer and inner circumferential system.

1.3. Morphological organization of bone

Two different kind of bone can be formed by bone tissue: cortical bone and cancellous bone.Cortical bone, as its name implies, forms the cortex, or outer shell, of most bones. It is much denser than cancellous bone. Furthermore, it is harder, stronger and stiffer than cancellous bone. It appears as a solid mass, dense because of the presence of only microscopic channels, it is devoid of macroscopic visible cavity. The primary anatomical and functional unit of cortical bone is the osteon.

Cancellous bone typically occurs at the ends of long bones, proximal to joints and within the interior of vertebrae, it is mainly composed of trabeculae which are interconnected to form a three-dimensional structure. Their orientation is not random, it is determined by the stress to which the bone is subjected. Spaces among them, named medullary cavity, are occupied by the bone marrow.

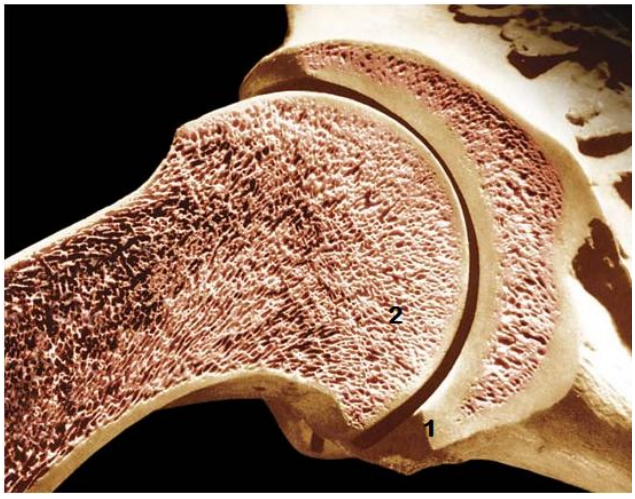

Figure 2. Different types of bone tissue:1)Compact bone; 2) Cancellous bone

In the skeleton of an adult male, about 80% of the skeletal mass is represented by compact tissue, which forms a solid cover around the bones and is responsible for the main functions of the skeleton: protection and support. The remaining 20% of the mass of the bone is given by spongy tissue.

1.4. Bone composition

Bone is composed of a mineral component (30%) and an organic matrix (70%). The organic matrix is formed by proteins, fibers and bone cells.

1.4.1 The mineral component

The mineral component of bone is composed of several crystals of calcium salts, mainly calcium phosphate but also small amounts of calcium carbonate, calcium fluoride, magnesium phosphate. Calcium phosphate is present in the form of apatite crystals, whose chemical formula is Ca_{10} $(PO_4)^{6++}$, the two positive charges are normally neutralized by binding with two hydroxide ions $(OH)^-$, forming the hydroxyapatite.

During the process of formation of hydroxyapatite crystals, calcium phosphate precipitates initially in the form of tiny amorphous aggregates. These aggregates are quickly replaced with thin needle-like crystals arranged in parallel with filamentous molecules of ground substance, called *crystal ghosts*. These crystals grow by taking the typical appearance of apatite crystals, they progressively occupy most of the space among the collagen microfibrils, permeating them. Once the crystals of apatite are formed, the deposition of new mineral occurs by the formation of new crystals or either by addition on pre-existing crystals. This phenomenon is finely regulated by bone cells through the production of specific molecules of the bone matrix.

1.4.2 Organic matrix

Fibers

The organic part of matrix is mainly composed of Type I collagen fibers. The bone collagen has a large number of cross-links that hold together the individual molecules of tropocollagen. Collagen microfibrils are arranged in transverse streak, with a period of 70 nm, and they aggregate to form collagen fibers of significant thickness (5-10 μm) in the fibrous bone tissue. In the other type of bone tissue, called lamellar, collagen microfibrils have a major thickness (approximately 60 nm) and they do not tend to aggregate in fibrils, they form a homogeneous felt. Thick bundles of collagen fibers start from periosteum and penetrate the intercellular

substance of the cortical bone tissue. These bundles are called Sharpey fibers and their main function is to anchor the periosteum to the bone surface.

Other kind of fibers can be found in the organic matrix of bone, elastic fibers are, in small portion, in the Sharpey fibers, while reticular fibers are localized in the basal membrane that surrounds the blood vessels inside the bone.

Bone cells

Four different kind of cells can be distinguished in bone: osteoprogenitor cells, osteoblasts, osteocytes and osteoclasts. Actually, osteoprogenitor cells, osteoblasts and osteocytes are consecutive functional stages of the same cell type, which came from the differentiation of the mesenchymal cell of the connective tissues[3].Osteoprogenitor cells have an oval shape and they are located on the free bone surfaces, in the inner layer of the periosteum and endosteum and near the capillaries. They have an high reproducing capability, that mainly occurs during the body growth. During their differentiation, osteoprogenitor cells become osteoblasts.

Osteoblasts have a size of about 15 - 30 μm and present a globular or polyhedral shape. They are responsible for the synthesis and deposition of the organic molecules of new bone intercellular material. Osteoblasts are joined together and with the nearest osteocytes through gap junctions. Thanks to these junctions, molecules and signals for the coordination of the metabolic activity or for the deposition of bone matrix and its mineralization can be exchanged. Osteoblasts are also involved in bone remodeling processes. In fact, these cells can start the reabsorption of the bone matrix indirectly, since they produce soluble factors that activate osteoclasts, the cells responsible for bone reabsorption, or either directly, secreting proteolytic enzymes able to separate the components of the organic matrix bone.

Osteocyte is a cell composed of a biconvex lens body shape and several cytoplasmic branches. Osteocytes are trapped within intercellular material, in cavities called lacunae and they communicate with other osteocytes as well as with free bone surfaces thanks to filamentous protoplasmic branches that occupy long, meandering channels (canaliculi) through the bone substance. The final parts of the branches are connected with those of the surrounding osteocytes by gap junctions.

Non-mineralized osteoid tissue occupies the thin space between the membrane of the cell body and the mineralized matrix. Water and dissolved substances (respiratory gases and metabolites), necessary for the nutrition of the cells, are able to reach all the osteocytes, even the most distant from blood vessels, through the osteoid tissue gaps and the canaliculi. At the end of its life cycle,

the osteocyte retracts its branches and degenerates. The maintenance and the remodelling of the mature bone is the main function of these cells.

Differently from these cells, osteoclasts are giant (100-200 μm) and multinucleated cells. Working from bone surfaces, they are responsible of the bone reabsorbtion, which is caused by a direct chemical and enzymatic attack. The erosive action of osteoclast occurs with the formation of the Howship lacuna on the bone matrix. Once a first lacuna is formed, the osteoclast moves on an adjacent portion of the bone and form a new lacuna. The activation of more osteoclasts can reabsorb large portions of bone in a short time. The osteoclast function is finely regulated by hormonal factors[4].

1.5. Osteogenesis of bone

The bone tissue should not be considered as a stable and definitive structure. As any other tissue, it is continuously renewed by an incessant work of demolition and rebuilding that changes its shape and structure, in order to fit it to needs. This continuous modelling of the bone tissue architecture comes from the action and proliferation of osteoblasts, which allows the processes of construction, and the opposite action of osteoclasts which causes the processes of destruction.

Osteogenesis always occurs involving the replacement of a pre-existing tissue, which can be both the mesenchyme or a differentiated connective tissue. Bone osteogenesis processes are predominant during prenatal life and they continue throughout the period of development.

There are two major ways of bone formation, the intramembranous ossification which is the direct conversion of mesenchymal tissue into bone and the endochondral ossification, the mesenchymal cells differentiate firstly into cartilage, and then this cartilage is later replaced by bone. Intramembranous ossification is mainly characteristic of the flat bones of the skull. This process starts from the proliferation and differentiation of the mesenchymal cells into osteoblasts, that secrete a collagen-proteoglycan matrix in order to bind calcium salts. In this way, the pre-bone (osteoid) matrix becomes calcified. Most of the osteoblasts were trapped in the lacunae of the calcified matrix becoming osteocytes. New osteoblasts differentiate and place themselves on the surface of newly formed bone, which grows gradually in thickness. At the same time, the differentiation of osteoclasts induces the dissolution of fibrous bone that will be later replaced with lamellar bone by new contingents of osteoblasts. The mechanism of intramembranous ossification involves also bone morphogenetic proteins and the activation of a transcription factor called CBFA1.

Endochondral ossification is an indirectly process of osteogenesis because it firstly involves the formation of cartilage tissue from aggregated mesenchymal cells, and then the subsequent replacement of cartilage tissue by bone[5]. The process of endochondral ossification can be divided into different stages. First, the mesenchymal cells condense into compact nodules and differentiate into chondrocytes, the cartilage cells. Chondrocytes proliferate rapidly to form the model for the bone. As they divide, the chondrocytes secrete a cartilage-specific extracellular matrix. When the chondrocytes stop dividing, they increase their volume dramatically, becoming hypertrophic chondrocytes. Hypertrophy alters the produced matrix by adding collagen X and more fibronectin to enable it to become mineralized by calcium carbonate. The cartilage matrix is eroded by osteoclasts that induce the enlargement of the lacunae of the cartilage. Blood vessels reach these cavities and together with the mesenchymal cells, differentiate in osteoblasts which finally begin forming bone matrix on the partially degraded cartilage[6][7][8]. Eventually, all the cartilage is replaced by bone. Endochondral ossification occurs in the formation of skeletal components such as the vertebral column, the pelvis, and the limbs which are first formed of cartilage and later become bone.

1.6. Bone remodeling

Bone tissue is an active tissue in which there is a constant balance between the reabsorption of existing bone (mediated by osteoclasts) and the deposition of new bone (by osteoblasts).These continuous processes of reabsorption and deposition are finalized to fit it to mechanical load applied on it. Furthermore, bone is the most important reserve of calcium in the organism so this processes contribute to the calcium regulation. The results of these phenomena are detectable microscopically but they do not involve changes of the macroscopic shape of bone. Remodeling may also occur in bones fully formed in response to intense and prolonged mechanical stress, repair of fractures or some diseases.

Remodelling begins with the recruitment of osteoprogenitor cells, which are induced to differentiate into osteoclasts in the region where reabsorption of bone is necessary. Activated osteoclasts break down bone matrix opening long cylindrical cavities named reabsorption cavities. These events require the presence and the active participation of osteoblasts and bone endothelial cells. New osteoblasts are differentiated from osteoprogenitor cells and adhering to the walls of the cavities, they lay subsequent layers of bone that will form the concentric lamellae of a new osteon. Therefore, examining a cross-section of lamellar bone is possible to distinguish: mature osteons, in which the deposition is over, new osteons which are forming,

characterized by a large Haversian canal and the presence of osteoblasts in a row along the bone surface facing the canal and reabsorption cavities, which are characterized by the presence of osteoclasts adherent to the bone walls.

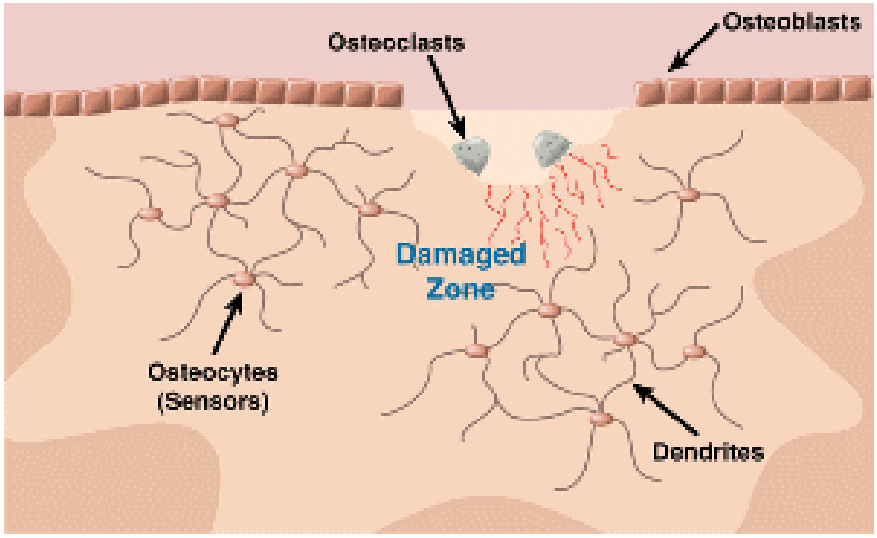

Figure 3. Bone remodeling: osteocyte cells sense the physical loading environment to which the skeleton is subjected, while osteoclast cells remove bone material that is no longer needed or that has been damaged, and osteoblast cells form bone. The process is coordinated by a communication network consisting of osteocytes in contact with each other, as well as with osteoblasts and possibly osteoclasts, to maintain strong, healthy bone.

1.7. Quantification of the cancellous bone architecture

The study of the cancellous bone architecture is an extended research topic in the last years, since the spatial and geometric properties of trabeculae affect mechanical properties of bone. Giving some examples, many studies confirm that porosity is inversely and exponentially proportional to the bone strength[9], or osteons where collagen fibers are oriented in the longitudinal direction are stronger and stiffer in tension than those where fibers are oriented in the transverse direction[10].

It is known that trabecular arrangement in a cancellous bone tissue is not uniform, the orientation and the degree of anisotropy change between different anatomical sites and between different individuals. This phenomenon could be explain considering that trabecular arrangement is not random but related to the load they should resist. Trabeculae are arranged in the same direction of the load, creating an intense network of struts and bridges, in which isostatic lines were naturally formed. Since the trabecular architecture is so important in the analysis of bone, the main histomorphometric parameters that allow to entirely described a bone sample are reported below[11].

Total volume,TV (mm^3) represents the total of volume examinated;

Bone volume, BV (mm^3) represents the volume occupied by bone in the sample analyzed;

Percent bone volume, BV/TV(%) represents the proportion of the volume occupied by bone;

Bone surface, BS (mm^2) represents the surface occupied by bone in the sample;

Bone specific surface, BS/BV (mm^{-1}) is the ratio of solid surface to its volume. It is a useful basic parameter for characterizing the thickness and complexity of the structure;

Bone surface density, BS/TV (mm^{-1}) is the ratio of solid surface to the total volume of the sample;

Trabecular thickness, Tb.Th (mm) is the average thickness of the trabeculae in the analyzed sample;

Trabecular separation, Tb.Sp (mm) is the average distance between trabeculae;

Trabecular number, Tb.N (mm^{-1}) is the number of trabeculae per unit of lenght;

Trabecular bone pattern factor, Tb.Pf (mm^{-1}) is an inverse index of connectivity, which was developed and defined by Hahn[12] for application to trabecular bone. It calculates an index of relative convexity or concavity of the total bone surface, on the principle that concavity indicates connectivity (and the presence of "nodes"), and convexity indicates isolated disconnected structures (struts). Lower Tb.Pf signifies better connected trabecular lattices while higher Tb.Pf means a more disconnected trabecular structure;

Structure model index, SMI indicates the relative prevalence of rods and plates in a three dimensional structure such as trabecular bone. SMI involves a measurement of surface convexity. This parameter is important in osteoporotic degradation of trabecular bone which is characterized by a transition from plate-like to rod-like architecture;

Euler number, Eu.N(mm^{-1}) is an indicator of connectedness of a three dimensional complex structure. It is a measure of how many connections in a structure can be severed before the structure falls into two separate pieces;

Degree of anisotropy, DA. Isotropy is a measure of three dimensional symmetry or the presence or absence of preferential alignment of structures along a particular directional axis. Apart from percent volume, DA of trabecular bone is probably the most important determinants of mechanical strength;[13]

Fractal dimension, FD is an indicator of surface complexity of an object, which quantifies how the object's surface fills space;

Porosity, Po (%) is an indicator of how many pores are in the structure[14].

1.8. Mechanical properties of cancellous bone

Cancellous bone tissue is a highly porous material, characterized by a complex internal structure composed of different elements (collagen fibers, lamellae, etc.). This subdivision is important to understand the mechanical behavior of the tissue since each level contributes with different mechanical properties. It can be considered a composite material where trabecular structure is the matrix and bone the filling material.

Trabecular structure is the one that essentially provides mechanical resistance of bone. Trabeculae are composed of hydroxyapatite crystals integrate in a matrix of collagen fibers, and create a rigid but also ductile material. The average thickness of a trabecula is 150-200 μm and in some cases, trabeculae may follow a preferred orientation.

The mechanical behavior of the cancellous bone tissue is best described as viscoelastic. The elastic part of this behavior is referred to the ability of the trabeculae to recover the complete initial geometry after the release of a load that did not exceed the elastic limit, the viscous behaviour is referred to phenomena such as permanent deformation resulting from particular mechanical stress.

A standard experimental techniques to measure *in vivo* the elastic constants of cancellous bone tissue doesn’t exist, however, an estimation of these properties can be measured by in vitro studies such as mechanical tests on bone samples taken from different anatomical sites and belonging to donors with different physical characteristics or a post-processing of sample images acquired by various methods (DEXA, CT, MRI).

In the last years, many research on bone have been focused on understand which factors determine the mechanical properties, how these properties are maintained, and how bone reacts to changes in its environment. The standard technique for studying mechanical properties of cancellous bone is the compressive test. However, the description and comprehension of the mechanical properties of bone is a difficult issue. Firstly, because of the bone mechanical anisotropy, the variation of the mechanical properties with the loading orientation implies a complexity in the definition of them. A meticulous description of anisotropic elastic properties may, in the general case, involve up to 21 elastic constants and, using a traditional experimental approach, this description is virtually impossible. Moreover, the mechanical tests are influenced by inherent errors and problems, such as specimen geometry, continuum assumption, viscoelasticity and temperature effects which affect the accuracy of the measurements.

The accuracy of the measurement is also influenced by the trabecular architecture. It is known from Wolff's law that bone architecture is strongly related to its mechanical characteristics, bone

changes its external shape and internal architecture in response to stresses acting on it. To avoid problems related to mechanical tests, according to Wolff's law, it is possible to study the mechanical characterization of bone analysing changes in its architectural parameters. One of the most studied architectural parameter is density. Several studies demonstrate how most elastic properties and strength are well predicted by density. However, comparing results obtained from the analysis of different anatomic regions or orientation, an equation describing the relation between density and mechanical properties cannot be define.

As well as density, other architectural parameters should be studied. Connectivity and anisotropy are fundamental because of the characteristic structure of bone. The connectivity of cancellous bone is more important since it has been hypothesized that a primary reason for decreasing strength and stiffness in osteoporosis is caused by a loss of trabecular elements and consequently a loss in connectivity. Also trabecular parameters such as trabecular thickness, trabecular density or trabecular separation are interesting. All of these aspects require 3-D information, and some of the properties have to be examined in 3-D space. Recent development in 3-D imaging of cancellous bone allows the direct study of 3-D architecture and mechanics. This provides for a wealth of possibilities and effectiveness evaluation of architectural properties. [13]

1.9. Bone pathologies: Osteoarthritis and osteoporosis

The evolution of bone mass during life follows height growth. It can be divided in three phases, an increase of bone mass during the first twenty years of life; a period of consolidation, characterized by a continuous and slow rise up to 35-40 years of age and finally a decrease that continues for the entire life. The loss of a certain amount of bone mass is physiological and unavoidable with age and this reduction is called osteopenia. However, when this process becomes particularly intense and prolonged, enough to induce fractures or trauma, it is called osteoporosis (OP).

Osteoporosis is a bone disorder characterized by an inadequate amount and faulty structure of bone, resulting in fractures from relatively minor trauma. It leads to a bone mineral density (BMD) reduction, a bone microarchitecture deterioration and an alteration of the amount and variety of proteins in bone [15][16].

With aging, other disease like osteoarthritis (CA) can occur. It is a metabolically active process that involves all joint tissues (cartilage, bone, synovium, ligaments and muscle), but mainly knees, hips and small hand joints are the peripheral sites most commonly affected. It is caused by

the breakdown and eventual loss of the cartilage of one or more joints. With aging, the water content of the cartilage increases, and the protein composition of cartilage degenerates. Eventually, cartilage begins to degenerate by flaking or forming tiny crevasses. In advanced cases, there is a total loss of cartilage cushion between the bones of the joints. Repetitive use of the worn joints over the years can irritate and inflame the cartilage, causing joint pain and swelling. Loss of the cartilage cushion causes friction between bones, leading to pain and limitation of joint mobility. Inflammation of the cartilage can also stimulate new bone outgrowths (osteophytes) to form around the joints[17][18].

Coxo-arthritis (CA) and osteoporosis (OP) are diseases of increasing incidence and prevalence with age and considerable associated morbidity [19][20]. These pathologies and their consequent risk of fracture depend not only on the bone mass (quantity of the mass) but also on the trabecular micro-architecture (quality of the mass). Because of their considerable incidence on the population, several studies analyzed how these diseases affect bone histomorphometric parameters [21][22].

Ding et al. [23], comparing specimens of proximal tibiae from healthy donors and donors affected by osteoarthritis (OA), demonstrated that OA specimens present an higher bone volume fraction and trabecular thickness and a lower bone surface to volume ratio than healty specimens. Fazzalari and Parkinson [24] obtained same results analyzing femoral head specimens from osteoarthritic donors and healty donors. Osteoarthritic specimens showed a significant decrease in trabecular number together with an increase in trabecular thickness and separation. Parfitt and Mathews [25]devised a new method for examining the structural changes that occur in trabecular bone in aging and in osteoporosis. Trabecular bone volume was calculated by the measurement of two indices, mean trabecular plate thickness (MTPT) and mean trabecular plate density (MTPD). Their work confirmed that osteoporotic specimens present a reduction in trabecular bone volume that was mainly due to a further reduction in plate density. Same results were observed by Chappard and Josselin[26]comparing twenty four transiliac bone biopsies from patients with corticosteroid induced osteoporosis (CSIOP) with specimens obtained in control subjects.

1.9.1 Osteoporosis

Many factors can increase the incidence of osteoporosis disease, one of the main factor is the age. With the age increasing, the rate of bone reabsorption remain constant but the rate of bone formation, however, decreases causing an inadequate amount of bone. Moreover, the incidence

of osteoporosis is more frequent in a female than in a male adult. More factors can explain this difference. Firstly women have a lower peak bone mass and a lower muscle mass than men. Moreover, bone loss is accelerated during menopause and also during the reproductive age. Even the smaller diameter of female bone contributes to increase the fragility of the skeleton. Other risk factors that may affect the incidence of osteoporosis can be related to eating habits and lifestyle. A low consumption of calcium-rich foods, an excessive alcohol consumption, a sedentary lifestyle and smoking could increase the risk of osteoporosis.

Another factor that has been much studied in the last years is related to long-duration spaceflight. Loss of bone mass is a well-known medical complication of long-duration spaceflight. Although this bone loss may not be sufficient to cause a notable increase in fracture risk immediately on return, the resulting degradation of the bone structure may result in a marked increase in fracture risk at more advanced ages due to age related osteoporosis. Space flight is a reality for more than 40 years but studies on the effects of microgravity on physiological conditions are relatively recent. At the end of spaceflight, humans and laboratory animals show abnormalities of the system including reduction of skeletal bone formation and mineralization, osteopenia and reduced bone strength. Thus bone loss and fracture risk are a scenario of medical priority in the design of missions spatial long-term. Several studies have shown that during the orbit space, the conditions of almost weightlessness (microgravity) cause a reduced use of the muscular-skeletal system. Approximately 1-2% of the skeleton is lost each month, with variability related to the age and individual characteristics, it was also shown that the recovery after the flight usually requires a long period. However, the effects of microgravity on the health of the skeletal system are not yet sufficiently known, both for the limitations imposed by space flight experiments and the difficulty in reproducing space conditions on the ground. A lot of studies on this topic were conducted reproducing space conditions with bed rest, which is a medical treatment involving a period of consistent (day and night) recumbence in bed. However, the effects of spaceflight on bone metabolism are profoundly different from those caused by in vivo studies such as reduced bed rest, restraining, resection of nerve bundles. Other studies used mathematical models of bone remodeling to simulate a specific bone disease, by disrupting the steady state or balance in the normal remodeling process, and to simulate a therapeutic strategy[27][28][29].

CHAPTER 2

Technology of a Micro Computed tomography

2.1. About tomography

Computed Thomography is a relatively new field in the area of non destructive imaging. It allows to reconstruct the internal structure of opaque objects without destroy them. This is a great advantage compared to conventional microscopy techniques. Any optical or electronic microscope, in fact, provides information on the internal structure of samples only if samples are properly processed and sectioned. In this case, information about three-dimensional structure could be obtained by the image of a surface or a combination of several thin slices, but in both cases information cannot be certain since methods of cutting and preparation could dramatically change the structure of the sample. Microcomputed tomography, commonly referred to as μCT, like conventional computed tomography is based on the collection of the projections of X rays through a specimen and the application of tomographic principles to reconstruct the 3-D structure of the specimen. The term 'micro' denotes a scanning system that is much higher in resolution than conventional clinical scanners. While clinical tomographic scanners may have a millimeter resolutions or less, high-resolution μCT scanners may reach resolutions below five microns.

This technology is based on the interaction of X radiation with the matter, depending on the density of the material, X-rays are more or less absorbed. Absorption depends on the energy of the incident X-rays and because of this, different processes of absorption can occur. The radiation coming out from the sample, is more or less attenuated according with the density of the object analyzed and, thanks to mathematical algorithm, this radiation is used to create images. Characteristics of the internal structure of an object such as dimensions, shape, internal defects, and density are readily available from CT images.

2.2. X radiation generation

X-rays are composed of a wide band of electromagnetic radiation with wavelengths in the range 0.001nm ÷ 10 nm, to which corresponds a frequency interval of $3\ 10^{16} \div 3\ 10^{20}$. Usually X-rays can be divided into *hard rays*, wavelengths in the range 10^{-3} nm ÷ 10^{-1} nm and *soft rays*, in the range 10^{-1}nm ÷ 10 nm. Electromagnetic radiation consists of photons, each with an energy *E* inversely proportional to its wavelength:

$$E = \frac{hc}{\lambda} = h\nu$$

where h = 6,6261 10^{20}Js is Planck's constant, c = $3\ 10^{8}$ m/s is the speed of light and ν is the frequency.

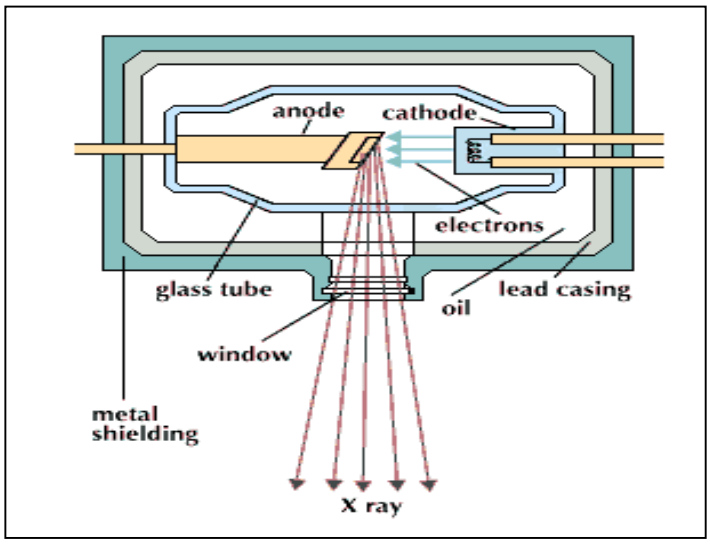

Figure 4. Schematic representation of a X-ray tube for the generation of X-radiation.

X-rays are produced by bombarding a metal target in a x-ray tube with high speed electrons accelerated by tens to hundreds of kilovolts of potential. X-rays are produced when the electrons suddenly decelerates upon collision with the metal target; these x-rays are commonly called brehmsstrahlung or "braking radiation". The emission spectrum of the X radiation, consists of two spectra: one continuous and one characteristic.

The first one is caused by the production of Brehmsstrahlung x-rays. When an electron approaches the atom target, it is deflected and braked because of the interior electrostatic fields of the atom. The energy dissipated during this breaking is emitted in the form of X-ray. This spectrum is continuous because of the countless deviations that the electron can undergo

approaching the atom. A very important feature, however, is the threshold value of the minimum wavelength to allow an x-rays emission. This value corresponds to the collision in which the incident electron loses all its energy. It depends by the kinetic energy of the incident electrons and then varying the material of the target, the shape and intensity of the spectrum can change but not the value of the wavelength threshold.

Conversely, the characteristic spectrum is caused by the characteristic x-rays and it depends on the target material. Electrons of a certain kinetic energy, hitting the atom of the target, can make the electron in the deeper layers of the atom escape and create a gap. This gap is filled by an electron of the outer layers and during this process a characteristic X photon is emitted. The gap created from this last electron is then filled by an electron which is in a more external layer, causing the emission of another characteristic line of the spectrum. This X photon are emitted with precise energies equal to the difference between the atomic energy levels of the target atoms.

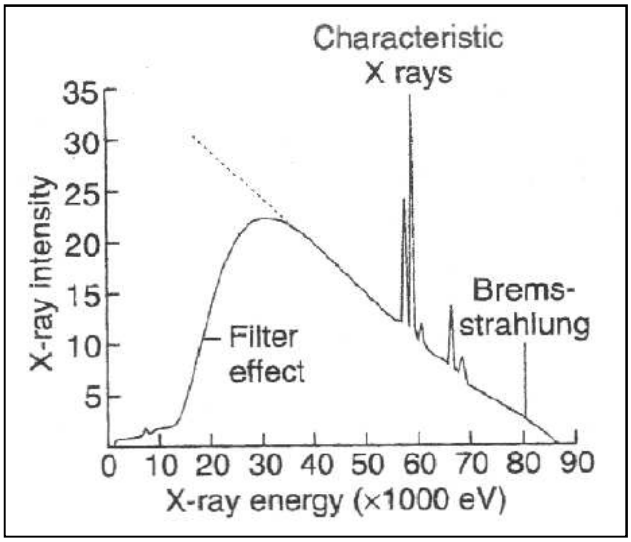

Figure 5. X-ray spectrum of a tungsten source for a tube voltage of 87 kVp.

2.3. Interaction of X-radiation with matter

X radiation is considered a ionizing radiation. The term ionizing is referred to the capability of the radiation to ionize the matter. Radiation with enough energy, during an interaction with an atom, can remove tightly bound electrons from the orbit of an atom, causing the atom to become charged or ionized. The effect of the X radiation on the matter depends on its energy. When the X radiation hits the matter is more or less absorbed and the processes that manage this interaction can be: Rayleigh scattering, Compton effect and Photoelectric effect.

Rayleigh Scattering

This kind of interaction occurs especially for low-energy X-rays, for example in mammography images (15 to 30 KeV). The energy emitted by the incident radiation makes the electrons in the atom of the matter oscillate in phase. The electron cloud of the atom immediately re-emits this energy by a photon of the same energy, but in a slightly different direction (Figure 6a).

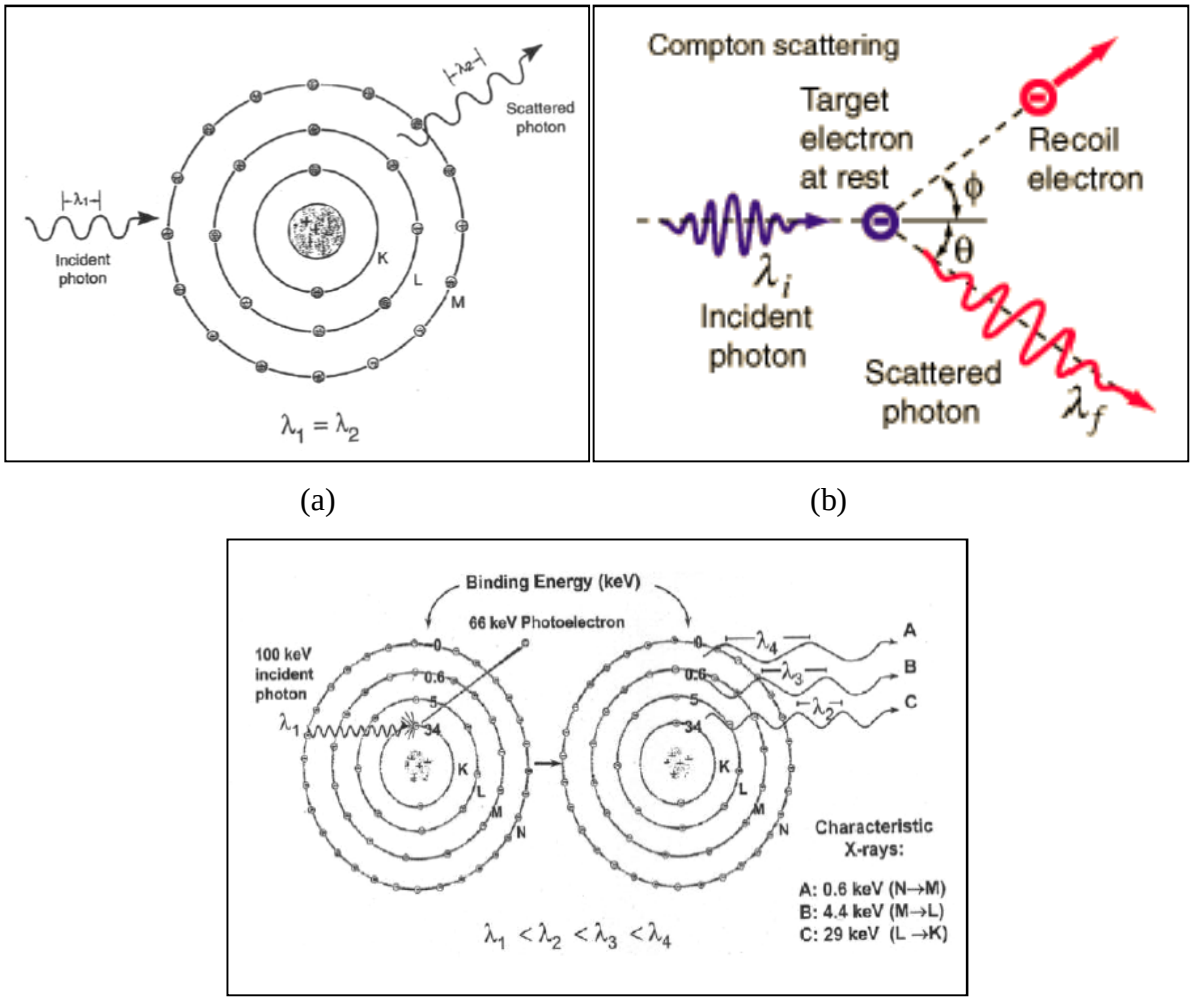

Figure 6. Different effects of the interaction X-rays-material: (a) Rayleigh Scattering, (b) Compton effect and (c) Photoelectric effect

The electrons are not removed from the atom, so this interaction causes only an excitation of the atom and the ionization doesn't occur.

In soft tissues, Rayleigh scattering generates less than 5% of the interaction with X-rays at energies greater than 70KeV, and at most 12% for energies of 30KeV.

Compton effect

Compton effect is the predominant kind of scattering in the range of photon energy, from26KeV until 30 MeV, which is usually used in diagnostics for soft tissues.

This interaction occurs mainly between photons and electrons placed in the external layers of the atom (Figure 6b). The electron is removed from the atom and a photon is scattered with a consequent reduction of energy.

For the principle of conservation of energy, the energy of the incident photon (E_0) is equal to the sum of the scattered photon energy (E_{sc}) plus the kinetic energy of the removed electron(E_{e-}):

$$E_0 = E_{sc} - E_{e-}$$

The interested electron is in the external layer of the atom so the binding energy of the electron is very small and it can be neglected.

The electron removed from the atom loses its kinetic energy by excitation and ionization of the surrounding atoms. The scattered photon passes through the matter without interaction or with further interactions such as Compton scattering or photoelectric absorption or Rayleigh scattering.

The energy of the scattered photon depends on the angle of its trajectory respect to the incident path and on the energy of the incident photon:

$$E_{sc} = \frac{E_0}{1 + \frac{E_0}{511keV}(1 - \cos\vartheta)}$$

When the Compton effect occurs at low energies, as in medical diagnostics (18 to 150 keV), most of the incident photon energy is transferred to the scattered photon which degrades the image, reducing the differences in attenuation due to the tissue.

Photoelectric effect

The photoelectric effect occurs when the energy of the incident radiation is high enough to move away an electron from the atom. All the energy of the incident photon is transferred to the electron. More exactly, the kinetic energy of the electron E_e is equal to the incident photon energy (E_0) minus the binding energy of the electron, E_b, (see Figure 6c):

$$E_0 = E_e - E_b$$

In order to have a photoelectric effect, it is necessary that the energy of the incident photon is equal or greater than the binding energy of the removed electron. After a photoelectric phenomenon, the atom is ionized, with a "lacuna" in the orbit from which the electron has been removed. This gap will be occupied by another electron which is in an orbital with lower binding energy. This phenomenon creates another lacuna in another orbital which, in turn, will be

occupied by another electron from an orbital with lower binding energy and so on. This leads to a cascade phenomenon from the outer orbit to the inner, as it schematically shown in Fig. 2.3c.

The difference in binding energy will be released each time both as characteristic x-rays, or as Auger electrons. The probability of obtaining characteristic X-ray decreases with the atomic number of the absorbing material and it is not so common with energies used in medical application.

The advantage of this effect in imaging is that it does not create additional photons which degrade the resulting image.

For low incident photon energies, the photoelectric effect is predominant in interaction with soft tissues. The process of photoelectric absorption allows to increase the difference in attenuation between different tissues with different atomic number, thus increasing the contrast between different tissues. At the energies typical of the X-ray imaging, 20-80 keV, the photoelectric effect is predominant with respect to other phenomena when the photons interact with materials of high atomic number Z, so in interaction with hard tissue as bone. Conversely, the Compton effect is prevalent in the interaction with tissues of lower atomic number, such as soft tissue and air[30][31].

2.4. Linear Coefficient of Attenuation

The Linear Coefficient of Attenuation is an indicator of the X-ray attenuation through the material. Considering the condition of a beam composed of N monochromatic photons and the thickness of homogeneous material, after crossing the thickness of matter ΔX, the beam coming out from the matter has an attenuation of ΔN given by the relation:

$$\frac{\Delta N}{N} = -\mu \Delta x \tag{2.1}$$

where μ is the linear coefficient attenuation measured in 1/cm.

Considering the limit condition for the thickness, so ΔX getting zero, the relation becomes:

$$\frac{dN}{N} = -\mu \Delta x \tag{2.2}$$

integrating this relation on the thickness matter:

$$\int_{N_0}^{N} \frac{dN}{N} = -\mu \int_{0}^{x} dx \tag{2.3}$$

with N_0 is the incident photons number.

The integration gives:

$$\ln N - \ln N_0 = \ln \frac{N}{N_0} = -\mu x \tag{2.4}$$

From this relation, a proportionality between the attenuation of the radiation and the thickness of the crossing matter is defined.

Consequently, the linear coefficient of attenuation and the number of photons coming out from the matter are calculated from these formulae:

$$\mu = -\frac{1}{x} \ln \frac{N}{N_0} \quad , \quad N = N_0 e^{-\mu x} \tag{2.5}$$

In this first case of homogeneous material, we assumed that the attenuation coefficient has been assumed constant throughout the thickness.

Considering an inhomogeneous material, the attenuation coefficient cannot be considered constant then the relationship becomes:

$$N = N_0 e^{-\int \mu x} \tag{2.6}$$

Moreover, in a real case, radiation is not monochromatic but composed of photons of different energy. The radiation coming out from the tungsten anode of the X-ray tube has a characteristic spectrum[31][32] and it is differently attenuated, depending on its energy. X-rays of higher energy are less absorbed than X-rays of lower energy. Because of this, the number of photons after the matter crossing and also the attenuation coefficient must be calculated considering the energy of the incident radiation. The number of photons coming out from the matter is then calculate by the following relation:

$$N = \int N_0(E) e^{-\int \mu(x,E) dx} dE \tag{2.7}$$

where $\mu(x,E)$ is a function of the position and the energy.

2.5. Instrumental set up and working principle of Tomography and Micro-Tomography

The first Computed Tomography has been invented in 1971 by the British engineer Godfrey Hounsfield and the South African physicist Allan Cormack. This first generation of tomography has never been used in medical application but it is useful to understand how it works.

Figure 7. Hounsfield and the first Tomography

In this prototype, the X-ray tube and a single detector are fixed to each other, the X-rays beam is collimated so that it can be considered as a single line of photons X (pencil beam).The one-dimensional beam, passing through a first line of the organic section, undergoes an attenuation$\mu(x,y)$ which is the sum of the attenuation corresponding to the μ-th along that line. The line integral is calculated and stored, then the system tube-detector is translated and another section of the patient is analyzed. The apparatus proceeds in this way until the entire patient is scanned, line by line. The collected values of line integrals generate the "projection of the anatomical section" relative to the angle for which the translation is performed . All other projections are obtained by rotating of a certain angle θ the whole tube-detector system with respect to the patient and repeating the procedure listed above. At the end, a set of projections of the patient are available. θ is the angle between two reference systems: the first one of the patient (x, y) and the second one of the tube-detector system (s, t). A theorem, discussed in the following paragraph, allows to combine together the projections and calculate the $\mu(x, y)$value at each point of the section. The disadvantage of this first tomography is the scanning times. It requires from 5 to 10 minutes per image, therefore a complete examination could take more than 24h.

All of the future developments are focused on the reduction of the execution times and so the subsequent reduction of the dose given to the patient.

In the second generation tomography, the one-dimensional beam is replaced by a narrow fan beam. Consequently a single detector is not enough, a number of 8 - 30 detectors is necessary. The higher number of detectors decreases time taken for the translation along t, then the

acquisition of an entire anatomical slice for a certain angle θ becomes faster. Nothing changes about the rotation of the tube-detector, compared to the first generation tomography.

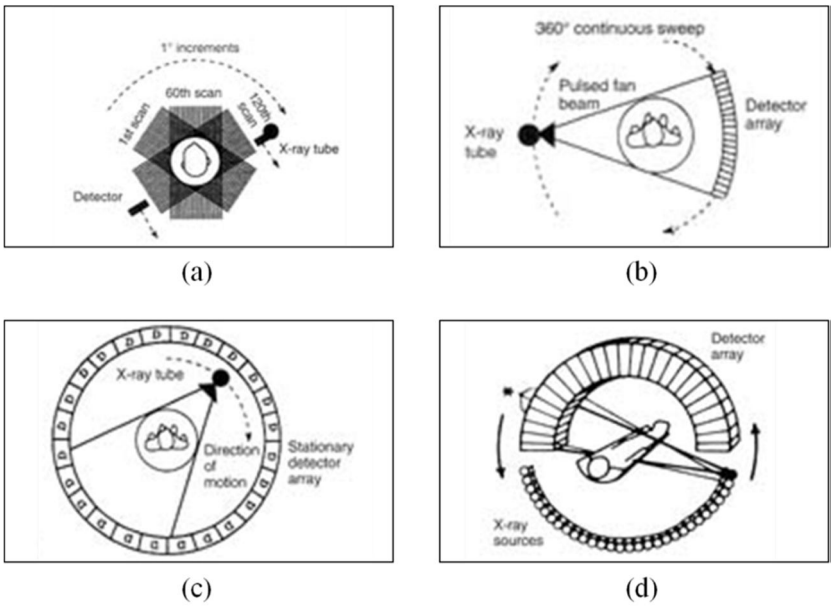

Figure 8. Schematic instrumental set-up of different generations of tomography: (a) First generation, (b) Second generation, (c) Third generation, (d) Spiral tomography

In the third generation CT system, the fan beam is large enough to scan the entire anatomical section and eliminate the translation. To use a so wide fan beam, it is necessary the presence of an arc of detectors, which still moves together with the tube. So, with a single beam emission, the entire projection of the anatomical section for a certain angle is acquired. In order to reduce the number of moving parts and so all the electronic circuitry, a ring of detectors is fixed to the gantry, which is in medical CT equipment the part that contains the rotating unit, and covers 360 degrees. The tube always emits a fan beam, but it is no fixed with the system of detectors.

Nowadays, in medical CT,3D imaging is mostly done by spiral CT. The X-ray tube rotates continuously around the patient, while the patient is slowly translated through the gantry.

Another way of 3D imaging in medicine is making use of a multi-slice scanner. This type of scanner allows to acquire multiple slices simultaneously using adjacent detector arrays[33][34].

The most striking difference between a medical CT system and a microtomographic instrument ,except for the size of the apparatus, is the instrumental set-up. In the figure below is reported the scheme of the microtomographic instrument Skyscan 1072, which is the apparatus used in this research. The source-detector system consists of a microfocus X-ray tube and a X-ray detector. The source is a X-ray tube air-cooled, having dual focal spot, respectively, 5 and 8μm. It is

composed of an additional filtration, consisting of an Aluminum foil with a thickness of l mm. Its power source can reach the maximum value of 10 Watt, the potential difference can vary in the range 20-100kV, and its amperage can vary between 0 and 250 μA. The detector is a CCD, model C4742-55-l2NRF, consisting of 1280 X 1024 pixels, air-cooled and connected to an Analog/Digital converter with 12-bit resolution. The geometry of the beam emitted by the x-rays tube is a cone beam and the CCD sensor is a matrix covering all the field of view in two directions, so with only one scan all the object is acquired.

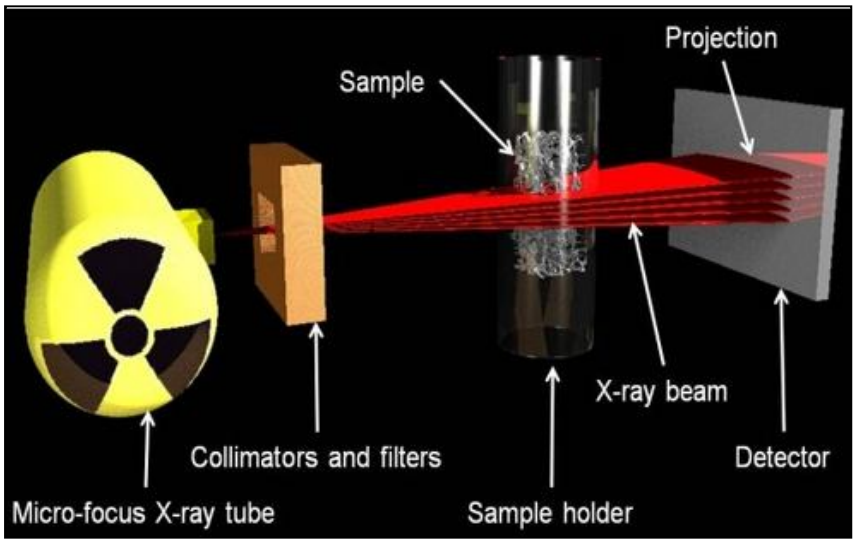

Figure 9. Main components and working principle of a Micro-CT scanner

Differently from the medical CT, instead of a rotating source-detector system, micro-tomography is composed of a static tube-detector unit and a rotating specimen holder. In this way, a more stability of the set-up is achieved with the subsequent removal of the vibrations during the acquisition. Furthermore, the holder supporting the object can also translate along the optical axis, allowing a magnification of the image of the object. Considering the absence of the vibrations and the possibility to improve the magnification of the image, this microtomography allows an enhanced resolution and it can be optimal for the analysis of small objects[35].

2.6. Image reconstruction: Back projection algorithm

The main components of a CT are an X-ray tube and a detector, the test component is placed on a turntable stage between the radiation source and the imaging system. The turntable and the imaging system are connected to a computer so that X-ray images collected can be correlated to the position of the test component. The imaging system produces a 2-dimensional shadowgraph

images of the sample just like a film radiograph. Specialized computer software makes possible to produce cross-sectional images of the test component as if it was being sliced. The imaging system provides a shadowgraph of an object, with the 3-D structure compressed onto a 2-D plane. Observing the simple case of a circular phantom acquisition, reported in Figure 10, the density data along one horizontal line of the image is uncompressed and stretched out over an area. This information by itself is not very useful, but when the test component is rotated and similar data for the same linear slice is collected and overlaid, an image of the cross-sectional density of the component begins to develop.

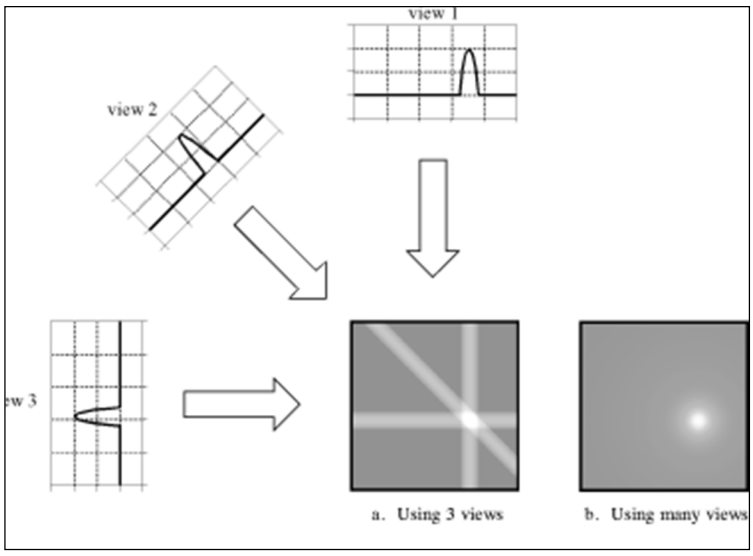

Figure 10. Projections of a point object generated by the irradiation from different scan angle.

The lighter area indicates an area of less density in the component because imaging systems typically glow brighter when they are struck with an increased amount of radiation. When the information from the second line of data is stretched across and averaged with the first set of stretched data, it becomes apparent that there is a less dense area in the upper right quadrant of the component's cross-section. Data collected at more angles of rotation and merged together will further define the feature of the test. A number of slices through the object can be reconstructed to provide a 3-D view of internal and external structural details. The 3-D image can then be manipulated and sliced in various ways to provide thorough understanding of the structure[36][37][38].

The collimated beam of radiation emitted by the X-ray source invests the sample and the interaction with the matter causes an attenuation of the radiation, proportional to the density of the matter. This attenuated radiation is collected by the radiation detector that transfers data to a computer for the final elaboration. The result of this process is the formation of a two-

dimensional image (projection) which contains information about the attenuation coefficient of the object. The sample, located on a rotating holder, is rotated in order to obtain a projection for each rotation step. The analysis of these projections by dedicated algorithm provides a set of images corresponding to the cross sections of the sample.

There are many methods of collecting projection data in order to obtain the three dimensional structure. The most simple is called "parallel projection" and is illustrated in Figure 11a. Other methods for collecting the projection data such as fan beam, and cone beam projections are shown in Figure 11b and Figure 11c.

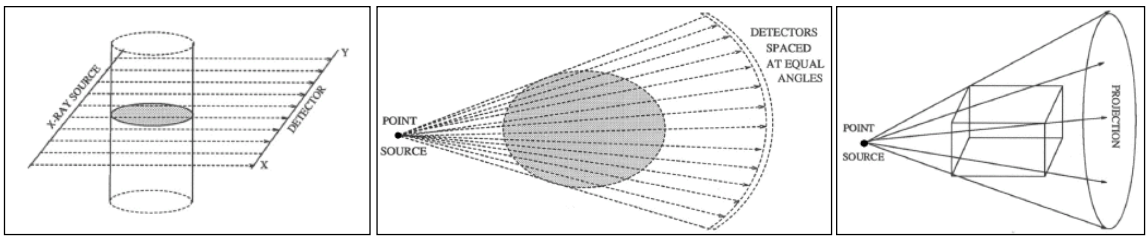

a) b) c)

Figure 11. Different methods for the collection of the projection data: a)parallel projections method; b) fan beam method; c) cone beam method.

For the reconstruction of the images, it is possible to consider always a parallel rays geometry and then modify the algorithm in a suitable way.

Considering the simple case of parallel beam irradiation, each point on the shadow image contains the information of the attenuation inside the three-dimensional object integrated along the path of the corresponding partial X-ray beam. This information is given by the line integral:

$$ln\left(\frac{I_0}{I}\right) = \int_{path} \mu(x)dy' \tag{2.8}$$

Where *dy'* is the differential path length and $\mu(x) = \mu(x,y)$ is the function describing the 2D distribution of absorption coefficients in the imaged object. The coordinate system showed in Figure 12 will be used to describe line integrals and projections.

Each line integral is described by the (θ, x') parameters. The equation of a ray that travels through the object with an angle of incidence θ and a distance x' with respect to the origin is given as:

$$xcos\vartheta + ysin\vartheta = x' \tag{2.10}$$

Mathematically a projection can be described by the Radon transform:

$$P_\vartheta(x') = \int_{-\infty}^{+\infty} \mu(x,y)\delta(xcos\vartheta + ysin\vartheta - x')dxdy \tag{2.11}$$

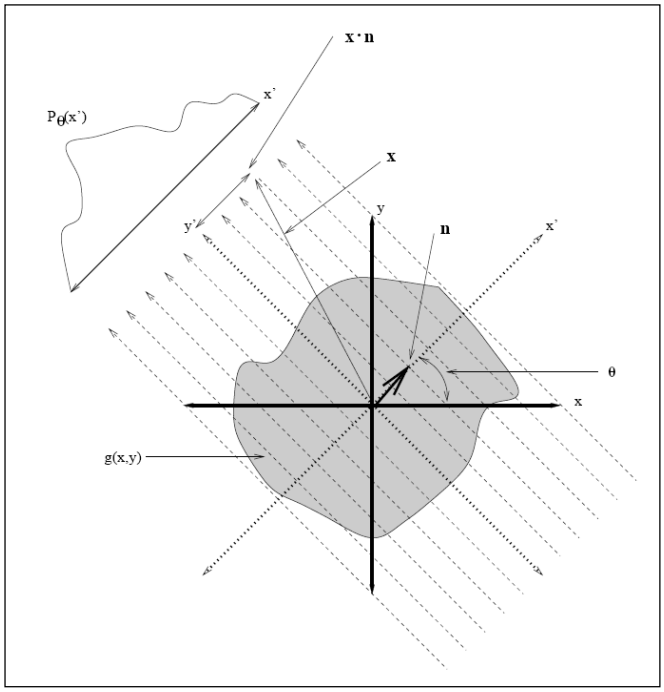

Figure 12. Coordinate system used for the description of the projections generation.

Radon assumes that, with a sufficient number of these projections obtained from different angles, it is possible to reconstruct the image of the attenuation map. To relate Radon data to a radial profile in Fourier space, the Fourier slice theorem is available. This theorem says that the Fourier transform of a parallel projection is equal to a slice of the two-dimensional Fourier transform of the original object. So the object can be correctly estimated by a two-dimensional inverse Fourier transform.

The two-dimensional Fourier transform of the attenuation can be defined as:

$$F(u,v) = \int_{-\infty}^{+\infty} \mu(x,y) e^{-i2\pi(ux+vy)} dxdy \tag{2.12}$$

and similarly the Fourier transform of a projection is:

$$S_\vartheta(\omega) = \int_{-\infty}^{+\infty} P_\vartheta(x') e^{-i2\pi\omega x'} dx' \tag{2.13}$$

By the nature of the Fourier transform, if an image *(x; y)* is rotated by an angle θ with respect to the x-axis, the Fourier transform *F(u; v)* will be correspondingly rotated by the same angle with respect to the u-axis, as it is shown in Figure 13. Therefore, the Fourier transformation of a projection along the lines that makes an angle $\theta+90°$ with respect to the x-axis depicts the Fourier transform of the image along the radial line that makes an angle θ.

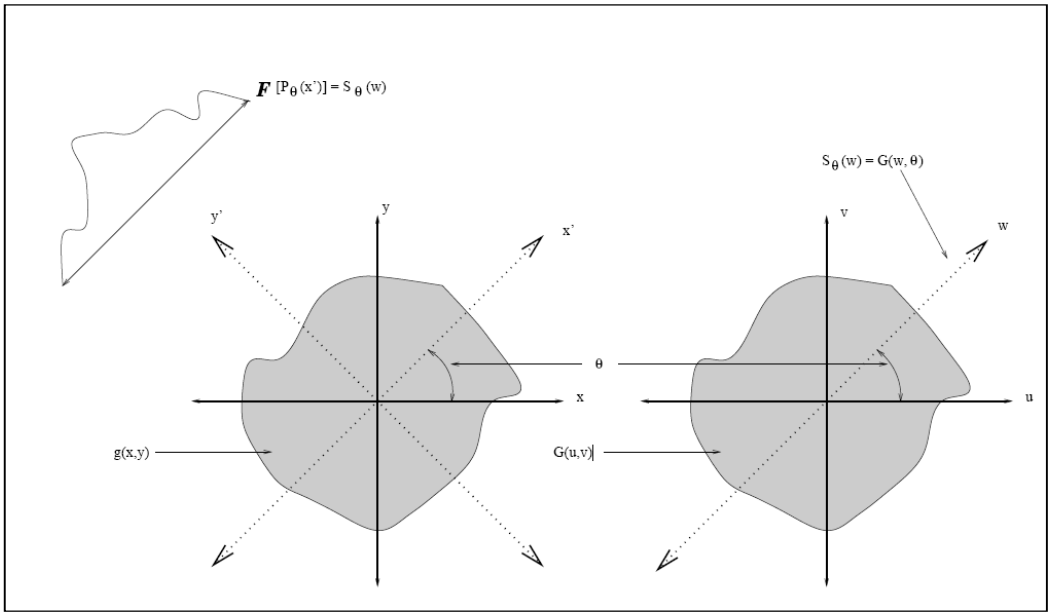

Figure 13. Schematic explanation of the Fourier theorem which is fundamental in the Micro-CT images reconstruction process.

Transforming coordinates *(x;y)* in the system coordinate *(x';y')*

$$\begin{bmatrix} x' \\ y' \end{bmatrix} = \begin{bmatrix} cos\vartheta & sin\vartheta \\ -sin\vartheta & cos\vartheta \end{bmatrix} \begin{bmatrix} x \\ y \end{bmatrix} \tag{2.14}$$

a projection along lines of constant *x'* can be written as:

$$P_\vartheta(x') = \int_{-\infty}^{+\infty} \mu(x', y')dy' \tag{2.15}$$

The Fourier transform is:

$$S_\vartheta(\omega) = \int_{-\infty}^{+\infty} \left[\int_{-\infty}^{+\infty} \mu(x', y')dy' \right] e^{-i2\pi\omega x'} dx' \tag{2.16}$$

Using the coordinate transformation in (2.14), equation (2.16) can be written in the coordinate system *(x,y)* as follow:

$$S_\vartheta(\omega) = \int_{-\infty}^{+\infty} \mu(x, y) e^{-i2\pi\omega(xcos\vartheta + ysin\vartheta)} dxdy \tag{2.17}$$

The second member of the equation represents the 2D Fourier transform at a special frequency so it can be expressed by the formula:

$$S_\vartheta(\omega) = F(u, v) = F(\omega cos\vartheta, \omega sin\vartheta) \tag{2.18}$$

Taking the Fourier transform of an object projections at different angles, the values *F(u,v)* of each projections can be determined on radial lines. Ideally, taking an infinite number of projections, the function *F(u,v)* could be known in every point of the frequency space. In practice

is impossible to take an infinite number of projections so the function *F(u,v)* can be known in a finite number of point, as can be observed in Figure14.

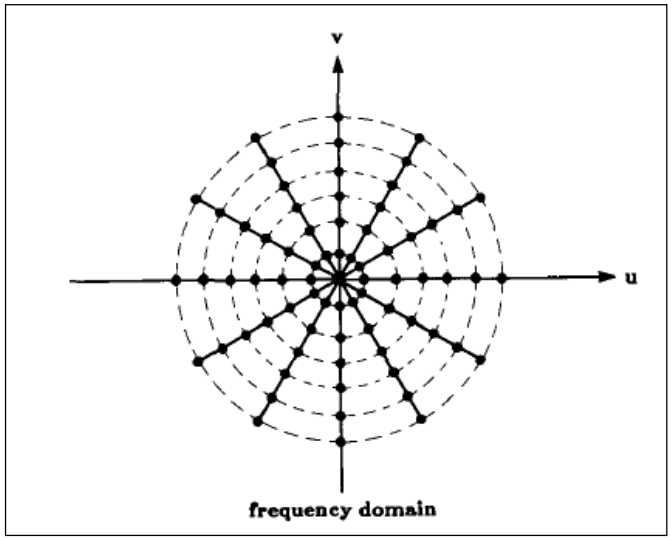

Figure 14. Points representing values of *F(u,v)* in the frequency space domain. Information at low frequencies (near the origin) is overemphasized, as compared to information at high frequencies.

At this point, it is intuitive that applying the inverse Fourier transform, the reconstructed image could be obtained.

The Filtered Back Projection algorithm uses Fourier theory to achieve at a closed form solution to the problem of finding the linear attenuation coefficient at various points in the cross-section of an object. A fundamental result linking Fourier transforms to cross-sectional images of an object is the Fourier Slice Theorem.

Considering the formula:

$$\int_{-\infty}^{+\infty}\int_{-\infty}^{+\infty}\mu(x,y)e^{-i2\pi\omega(xcos\vartheta+ysin\vartheta)}dxdy = F(u,v) \tag{2.19}$$

and applying the inverse Fourier transform, the distribution of the attenuation coefficient can be extracted:

$$\mu(x,y) = \int_{-\infty}^{+\infty}\int_{-\infty}^{+\infty}F(u,v)e^{i2\pi(ux+vy)}dudv \tag{2.20}$$

Making a coordinate transformation in the frequency domain, from rectangular coordinate system *(u,v)* to polar coordinate system *(w,θ)* and making the substitution:

$$\begin{cases} u = \omega cos\vartheta \\ v = \omega sin\vartheta \end{cases} \quad dudv = \omega d\omega d\vartheta \tag{2.21}$$

the equation (2.20) can be written as follow:

$$\mu(x,y) = \int_0^{2\pi}\int_0^{\infty} F(\omega,\vartheta)e^{i2\pi\omega(x\cos\vartheta+y\sin\vartheta)}\omega d\omega d\vartheta \quad (2.22)$$

This integral can be divided in two, considering θ from *0* to π and from π to *2*π. Considering the following property of the Fourier transform:

$$F(\omega,\vartheta+\pi) = F(-\omega,\vartheta) \quad (2.23)$$

equation (2.22) becomes

$$\mu(x,y) = \int_0^{\pi}\left[\int_{-\infty}^{+\infty} F(\omega,\vartheta)|\omega|e^{i2\pi\omega x'}d\omega\right]d\vartheta \quad (2.24)$$

Substituting the Fourier transform of the projection $S_\theta(w)$ with the two-dimensional Fourier transform $F(w,\theta)$, the following formula is obtained

$$\mu(x,y) = \int_0^{\pi}\left[\int_{-\infty}^{+\infty} S_\vartheta(\omega)|\omega|e^{i2\pi\omega x'}d\omega\right]d\vartheta \quad (2.25)$$

The formula can be written in the form:

$$\mu(x,y) = \int_0^{\pi} Q_\vartheta(x\cos\vartheta + y\sin\vartheta)d\vartheta \quad (2.26)$$

where:

$$Q_\vartheta(x') = \int_{-\infty}^{+\infty} S_\vartheta(\omega)|\omega|e^{i2\pi\omega x'}d\omega = F^{-1}\{S_\vartheta(\omega)|\omega|\} \quad (2.27)$$

The equation (2.27) can be expressed by the convolution:

$$Q_\vartheta(x') = P_\vartheta(x') * h(x') \quad (2.28)$$

and it represents a filtering operation in which the frequency response of the filter is$|\omega|$. The filter function is:

$$h(x') = F\{|\omega|\} \quad (2.29)$$

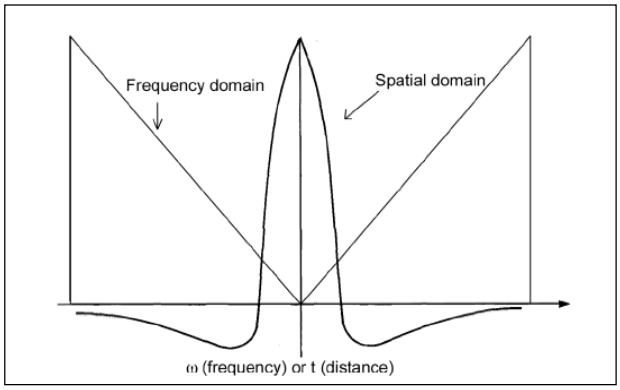

Figure 15. A good filter to linearly weigh the frequencies in the Fourier space.

Observing Figure 14, information at low frequencies (near the origin) is overemphasized, as compared to information at high frequencies. In order to linearly weigh the frequencies in the Fourier space, a filtering operation is necessary. A good filter is |w| filter (Figure 15) since it is a ramp that enhances the high frequencies and reduces the low frequencies. However, a disadvantage of this filter is the magnification of the noise in the projections data. So different modified filters can be used.

This algorithm can be used for parallel beam, in our case Micro-CT system works with fan beam or cone beam so some changes have to be introduced in order to reconstruct images [35].

2.7. Artifacts of Micro-CT images

Images reconstructed by a Micro-CT system can be distorted by some artifacts. Artifacts can seriously degrade the quality of computed tomographic images, sometimes to the point of making them diagnostically useless. To optimize image quality, it is necessary to understand why artifacts occur and how they can be prevented or suppressed. An artifact can be defined as any unphysical feature or any unrealistic distortion introduced, systematically or randomly, in the output slices during the acquisition or the reconstruction process. The reconstruction technique assumes that all the measurements are consistent, so any error of measurement will usually reflect itself as an error in the reconstructed image.

CT artifacts can originate from different kind of sources. It is possible to group the origin of these artifacts into four categories: physics-based artifacts, which result from the physical processes involved in the acquisition of CT data; patient-based artifacts, which are caused by such factors as patient movement or the presence of metallic materials in or on the patient; scanner-based artifacts, which result from imperfections in scanner function and artifacts, which are produced by the image reconstruction process. To separate the contribution of different kind of artifacts is usually a hard task. Furthermore, there are some artifacts which are always present and can never be completely eliminated: for example the so called metal artifact which produces streaks around a high absorbing detail or the scattering effect. This effect is due to scattered radiation generated from the interaction of the x-rays with the material, which induce the ionization of the material. The interaction of the x-rays is managed by different effects, depending on the energy of the incident radiation. One of this effect, the Compton effect, generates a secondary photon X which causes serious problems for the image formation because it alters the radiation coming from the object under investigation. In order to avoid this problem,

it is necessary that only the radiation which propagates along the source-detector trajectory reaches the detector.

In this study much attention is directed to those artifacts which are the most important in cone-beam geometry CT, but significantly reducible, in principle, by relatively simple operative procedures or post-processing techniques.

Maybe the most common and disturbing artifact of μ-CT systems operating by polychromatic X-ray tube is the beam hardening. Because the source emits a wide range of energies, when X-rays pass through the sample, the lower components of the spectrum are absorbed disproportionately compared to the higher ones: this causes the spectrum become harder and harder, the energy average content increases as the X-rays penetrate deeper into the object thickness, while at the same time the overall intensity drops. As a consequence of such a non linear behaviour, the attenuation properties of the sample are no more proportional to its thickness. For this reason it is absolutely difficult to carry out quantitative measurements on slices corrupted by beam hardening. The typical effect of beam hardening is the artificial brightening of the object exterior parts respect to the central ones, even if the material is perfectly homogenous (*cupping artifact*). Considering X rays passing through the middle portion of a uniform cylindrical phantom, they are hardened more than those passing through the edges because they are passing through more material. As the beam becomes harder, the rate at which it is attenuated decreases, so the beam is more intense when it reaches the detectors than would be expected if it had not been hardened. Therefore, the resultant attenuation profile differs from the ideal profile that would be obtained without beam hardening (Figure 16a). A profile of the CT numbers across a uniform cylindrical phantom displays a characteristic cupped shape (Figure 16b).

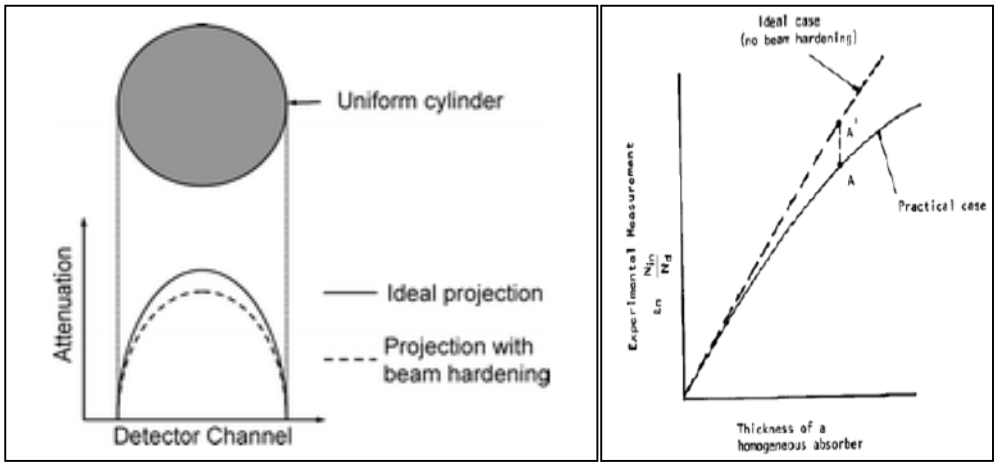

Figure 16. a) Attenuation profiles obtained with and without beam hardening for an x-ray beam passing through a uniform cylindrical phantom; b) Attenuated radiation passing through a homogeneous absorber. The attenuation

depends on the thickness of the absorber. In figure are reported the ideal case without beam hardening effect and the practical case with the influence of beam hardening.

Furthermore, in heterogeneous material, streaks can appear between two dense objects because the beam hardening extent changes form one view angle to another. They occur because the portion of the beam that passes through one of the objects at certain tube positions is hardened less than when it passes through both objects at other tube positions[40][41][42]. It's worth noticing that beam hardening artifact is strictly connected to the operating tube peak-voltage, which is related of course to the optimal energy required to scan the sample. In other words, working at low energies, the beam hardening resulting in the reconstructed slices is generally poor: it means that this artifact doesn't affect so much the low absorbing samples (polymeric foams, biological samples etc.). On the contrary, at higher energies the effect is considerable (metallic samples, bones, rocks etc.).

Another common artefact affecting CT images is the ring artifact. It appears as concentric rings superimposed to the true features of the reconstructed slice. They are generally due to the non linear response of some pixels of the detector that can occur for several reasons as drifts of the CCD elements caused by electronic or temperature instability, beam fluctuations, local overloading of the incoming photons. Ring artifacts are also strictly related to the beam hardening. The polychromatic spectrum, even when a middle energy is selected, contains single high energy photons that can impinge locally onto the detector saturating some of its pixels[43].Even if particular awareness is used during the scan in order to control the beam hardening effect, to avoid the local saturation of the CCD pixels and to appropriately acquire the flat filed images (usually by multi-frame mode to minimize the fluctuations), the ring artifacts can never be completely removed. A post-processing cleaning procedure is normally needed.

Another artifact related to the reconstruction process of the images is the undersampling of the object. The number of projections used to reconstruct a CT image is one of the determining factors in image quality. If the interval between projections is too large, information about sharp edges and small objects can be altered. This effect is reproduced on the reconstructed images by fine stripes radiating from the edge of a dense structure. Aliasing can be minimized by acquiring the largest possible number of projections per rotation.

Finally, particular attention should be done on the partial volume effect which rises from voxels containing two or more different materials. This affects especially voxels on the boundary between different materials. At each step the volume of the analyzed sample has finite dimension and its CT number is calculated as the average of the different coefficient numbers. Partial

volume artifacts cannot be eliminated, it can be only reduced by using a thin acquisition section width[44][45].

CHAPTER 3

Optimization of the Micro-CT for bone analysis

The morphological and mechanical characterization of trabecular bone is a much widespread research topic in the last years. Trabecular bone consists of a complicated three-dimensional network of plates and rods, arranged in a lattice-like network. Aging, disease process, and therapeutic agents could influence the number of elements in this network, their dimensions and connectivity, causing dramatic changes in bone strength. Until recently, information about structural parameters of trabecular bone were only available by histomorphometry, a destructive procedure limited to two-dimensional analysis. Micro-computed tomography (micro-CT) is an emerging technique for the non destructive assessment and analysis of the three-dimensional trabecular bone structure and it found large applications in basic as well as pre-clinical bone research throughout the last several years.

One of the most suitable equipment to investigate cancellous bone tissue is the Micro-Computed tomography because of its capability to reach spatial resolution as high as several microns,comparable to the size of the bone trabeculae [46].

In a micro-CT system, the X-radiation absorption coefficient, which is converted into grey levels of the image, reflects the amount of the bone mineral content so the research has been focused on the measurement of the bone volume from the analysis of the grey levels histogram of the images.

Before dealing with this issue, an accurate analysis on the Micro-CT under investigation has been done. Each step of a microtomographic analysis has been considered in order to understand how the results of the analysis can be affected by the choices of the operator.

3.1. Measurement of the resolution system

The first step of a microtomographic analysis is the acquisition of the sample. A sample placed into the micotomograph Skyscan 1072 is invested by a X-rays beam. The X radiation is attenuated, passing through the sample, and then collected by a detector. The attenuated radiation is conveniently transformed in grey-level images which contain information about the absorption coefficient of each sample point. This phase needs the operator to choose parameters related to the power source of the X-rays tube and the magnification. These parameters must be chosen considering the sample studied and the analysis required on it. About the magnification, it is important that all the sample is visible in the field of view in order to avoid artifacts on the images reconstruction.

Resolution has always been a topic of great interest since it provides a quantitative measure of the performance of imaging systems. However, two different concepts may be comprised by the term image resolution: high-contrast small-detail resolution, also called spatial resolution, for distinguishing adjacent objects of high-contrast, and low-contrast large-detail resolution, or contrast resolution, for differentiating an object from its background. A resolution measure combining both aspects is in the modulation transfer function or MTF. The MTF gives a description of how much contrast at a specific spatial frequency is maintained by the imaging process. In this way, contrast and resolution are thus combined in one standard measure.

In a micro-CT system, the resolution and consequently the quality of an image depends largely on the size of the x-rays source, then on the size of the focal spot. The focal spot size can be calculated from the measurement of the MTF.

3.1.1 Methods for the measurement of the Modulation Transfer function

One of the method for the calculation of the MTF is based on the calculation of the Point Spread Function which is, as its name suggests, the image of a single point object. This function plays an important role in the image formation theory because from the degree of blurring in the image of this point object, a measure of the quality of an optical system can be detected. Ideally, a perfect point source should be represented by a single pixel in the image, in reality, it is represented by more pixels.

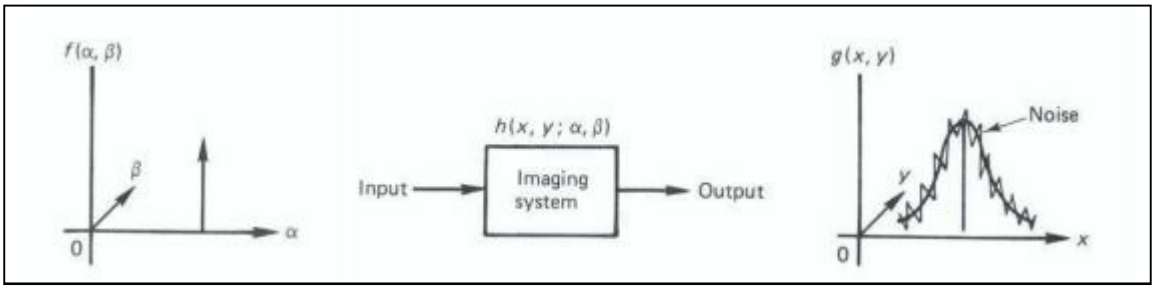

Figure 17. Blurring due to an imaging system

Mathematically, this can be expressed by the following formula:

$$g(x,y) = \int_{-\infty}^{*\infty} \int_{-\infty}^{*\infty} h(x,y;\alpha,\beta) f(\alpha,\beta) d\alpha d\beta + \eta(x,y) \quad (3.1)$$

where $\eta(x,y)$ is the additive noise function, $f(\alpha,\beta)$ is the object, $g(x,y)$ is the image, and $h(x,y;\alpha,\beta)$ is the Point Spread Function (PSF). From the PSF, information on the spatial resolution of the system can be obtain measuring its width. The most common way is the calculation of the Full Width at Half Maximum (FWHM) value, which is the width of frequency range where the signal's amplitude is equal to half of its maximum value.

To calculate the spatial resolution of a system, this method is not usually used because of its difficulty. The calculation of the PSF requires, for example, the acquisition of a very small white dot on a black background, on the image this small dot is represented only by a few pixels so its measurement could be strongly modify by the random noise.

Another method to define the spatial resolution of an imaging system is considering its Line Spread Function. It is the system response to a line which can be obtained with an infinitesimal slit in an opaque object. A correct measurement of the LSF requires a sufficiently narrow slit. Additionally, the use of a slit requires very precise fabrication and the perfect alignment of the device in the radiation beam. As for the PSF, this implies that its finite extent does not contribute significantly to the width of the image.

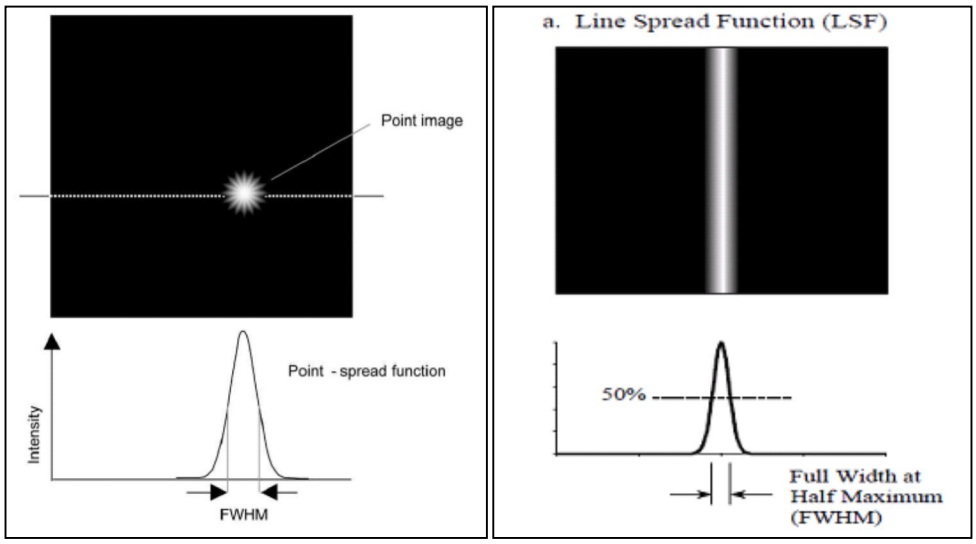

(a) (b)

Figure 18. a)Point Spread Function of an imaging system, b) Line Spread Function of an imaging system

In order to reduce technical difficulties associated with obtaining and measuring the Point Spread Function and the Line Spread Function, the method usually used for the definition of the spatial resolution of an imaging system is the measurement of its Edge Spread Function.

Differently from the other two, the edge response is simple to measure because edges are easy to be generated in images, for example using an opaque object with a straight edge. Moreover, starting from the ESF is possible to calculate the MTF by a one-dimensional FFT of the LSF, conversely, the PSF needs a two-dimensional Fourier transform.

From the ESF a measure of the resolution can be taken considering the 10% - 90% distance as it is shown in the figure below.

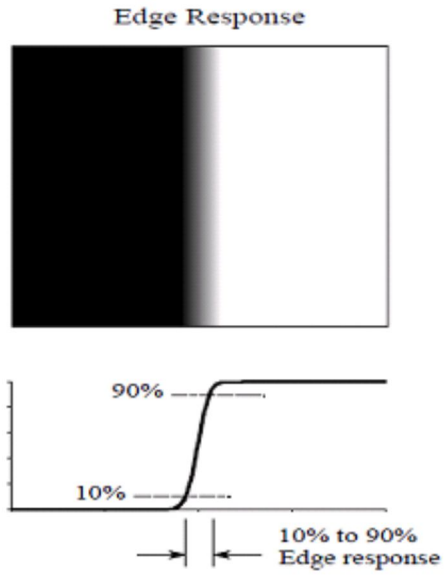

Figure 19. Edge Spread Function of an imaging system

Once the edge spread function has been determined, from its numerical derivative the Line spread Function is obtained and then a Fast Fourier Transform on the resulting LSF allows to calculate the Modulation Transfer Function. It is important to take care on select the correct number of points calculating the ESF with respect to the sampling rate in order to obtain the desired number of points in the resulting MTF. Moreover the frequency axis of the MTF must be conveniently scaled in order to represent MTF in terms of the Nyquist frequency of the imaging system. The Nyquist frequency is defined as the highest sinusoidal frequency that can be represented by a sampled signal and is equal to one half the sampling rate of the system.

From the Edge Spread Function, the LSF can be calculated as:

$$L(x) = \frac{dE(x)}{dx} \tag{3.2}$$

As a consequence, the optical transfer function along the u-axis, *O(u)*, can be determined by Fourier transformation of the LSF with respect to x.

$$O(u) = \int_{-\infty}^{+\infty} L(x) e^{-2\pi i u x} dx \tag{3.3}$$

The modulation transfer function *M(u)* is obtained as the modulus of the OTF.

$$M(u) = \left| \int_{-\infty}^{+\infty} \left(\frac{d}{dx} E(x) \right) e^{-2\pi i u x} dx \right| \tag{3.4}$$

The MTF gives a description of how much contrast at a specific spatial frequency is maintained by the imaging process.

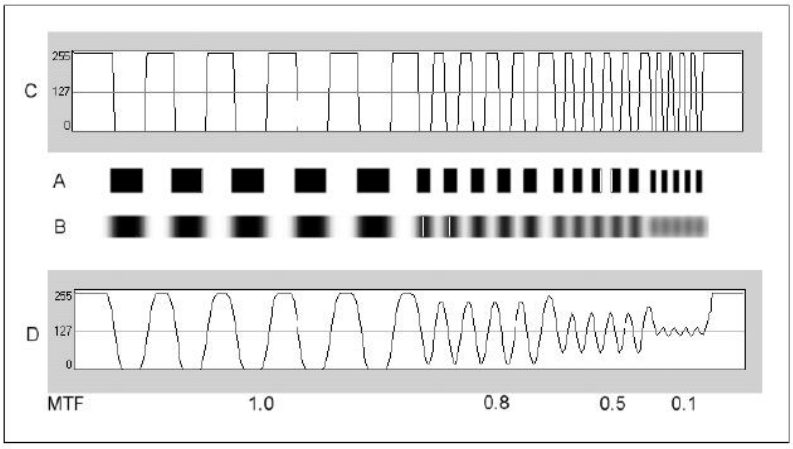

Figure 20. Response of an imaging system to a frequency modulated signal

In the optimal case, MTF value is 1, which means that the contrast of object and image is identical or thus maintained (illustrated in Figure 21). In the real case, MTF value is 1 for zero

spatial frequency and it then drops in a system-specific manner down to zero with increasing frequency.

By using the MTF, two imaging systems can easily be compared: at each spatial frequency (or 1/resolution) better contrast corresponds to the system with the higher MTF. MTF gives a measure for the decrease in contrast due to the imaging system, with increasing spatial frequency in the object (Figure 21). In this way, contrast and resolution are combined in one standard measure.

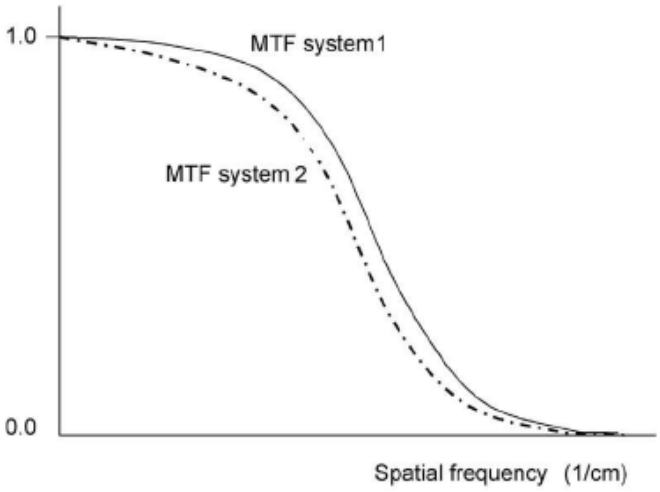

Figure 21. Modulation Transfer Function of two imaging system. MTF can be used to compare different systems.

Another value can be used as measure of the resolution of a system, this is the spatial frequency where the MTF falls to 10% of its maximum value, it is called the 10% MTF value and it is often used by manufacturers to characterize the performance of optical systems.

Since the FWHM and the 10% MTF values are both resolution measures obtained from the same data, they are not independent. In other words, there is no extra information obtained by using both measures [47][48][49].

3.1.2 Materials and methods

In order to calculate the Modulation Transfer System of the Micro-CT apparatus Skyscan 1072, a phantom made of plexiglas and aluminium has been used. The choice of these two materials depends on their characteristic attenuation coefficient, plexiglas has an attenuation range similar to that of biological tissue and water, while aluminium can be used as reference material for bone.

The edge device is composed of a 50-micron thick aluminium foil between two thin slabs of plexiglas.

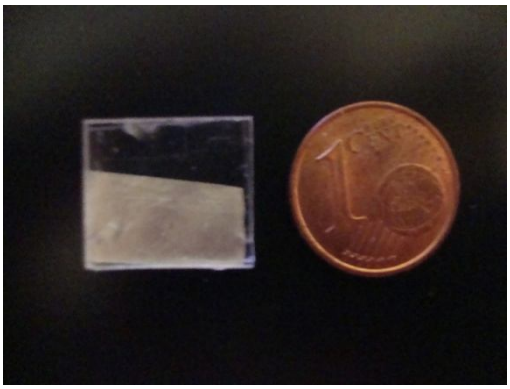

Figure 22. Edge device phantom constructed for the calculation of the Skyscan 1072 MTF. The phantom is composed of a 50-micron thick aluminium foil between two thin slabs of plexiglas.

Much care must be taken on the position of the phantom inside of the Micro-CT. To obtain a good image for the MTF calculation, it must be placed perpendicularly to the direction of the x-rays beam.

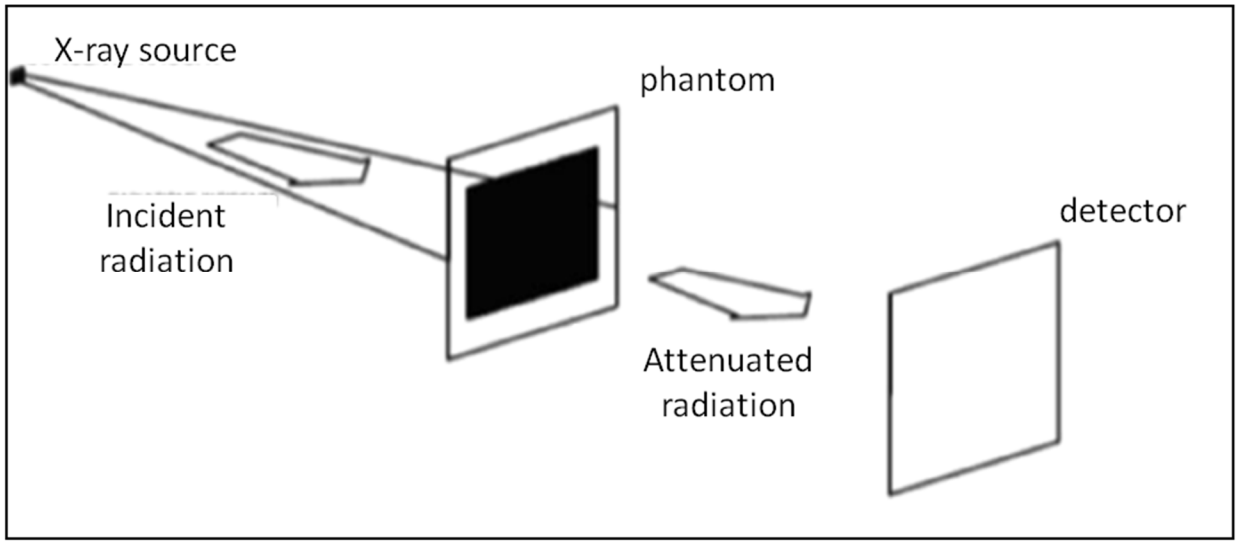

Figure 23. Position of the phantom with respect to the X-ray source and detector

Moreover, to obtain a large number of data for the detection of the edge it is important that the edge does not coincide with the columns of pixels in the reconstructed image of the phantom so the phantom has been constructed with the edge tilted four degrees from the horizontal [50][51][52][53]. The Micro-CT acquisition parameters have been chosen in order to obtain the best image for the following elaboration. In this way, values of 50 kV and 198 μA were chosen. Moreover, the acquisition has been done without the Aluminium filter for the image noise

correction because its thickness (1 mm) is bigger than the thickness of the Aluminium foil in the phantom. Considering the choice of the magnification parameter, from the literature the optimal condition for the calculation of the Modulation Transfer Function is represented by the placement of the phantom in contact with the detector. In this research, a digital image of the edge has been processed for different value of magnification in order to investigate the influence of this parameter on the MTF measurement. The values of magnification chosen for the analysis are: 15X, 35X, 55X and 75X. An image of the edge for each value is reported in Figure 24.

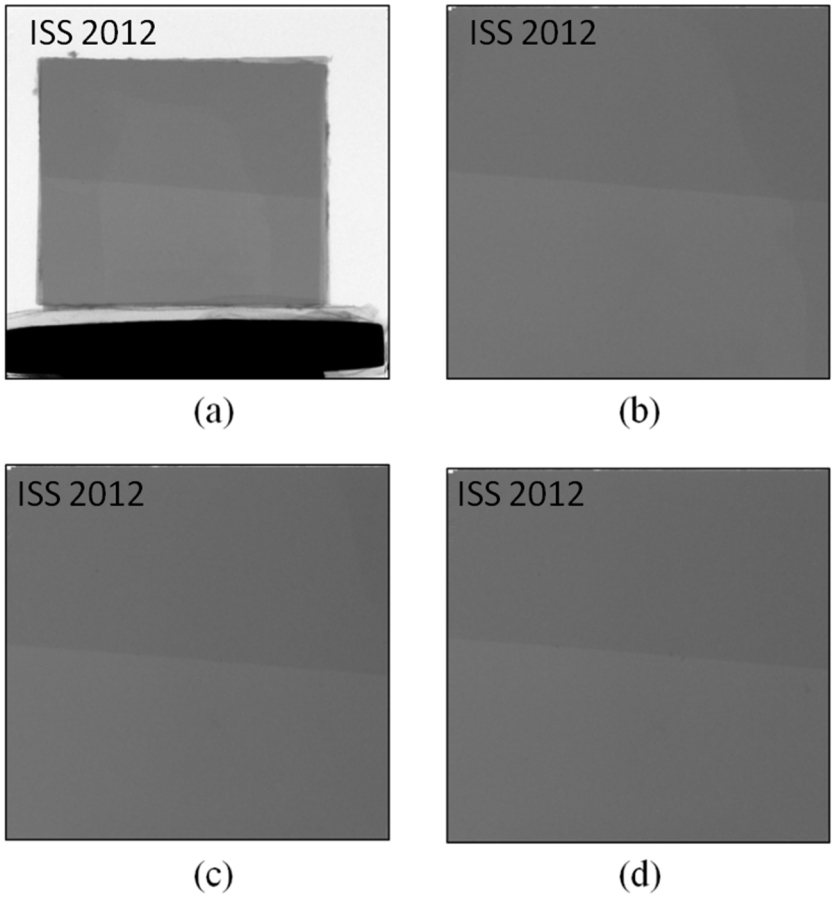

Figure 24. Edge device image for different values of magnification: (a) 15X, (b) 35X, (c) 55X, (d) 75X

The calculation of the Modulation Transfer Function from the acquired image has been done developing a code in Labview ™ 8.2. This program allows:

- the detection of the edge by a set of samples
- the calculation of the ESF for each sample and then the mean value of the ESF
- the calculation of the LSF with its FWHM and MTF.

The first step of the code requires the selection of a Region Of Interest in which the edge is detected, then the edge is identified and represented by a set of points. The number of points, so

the frequency of the edge sampling can be chosen by the operator. An higher number of points allows to obtain a more accurate measure of the MTF.

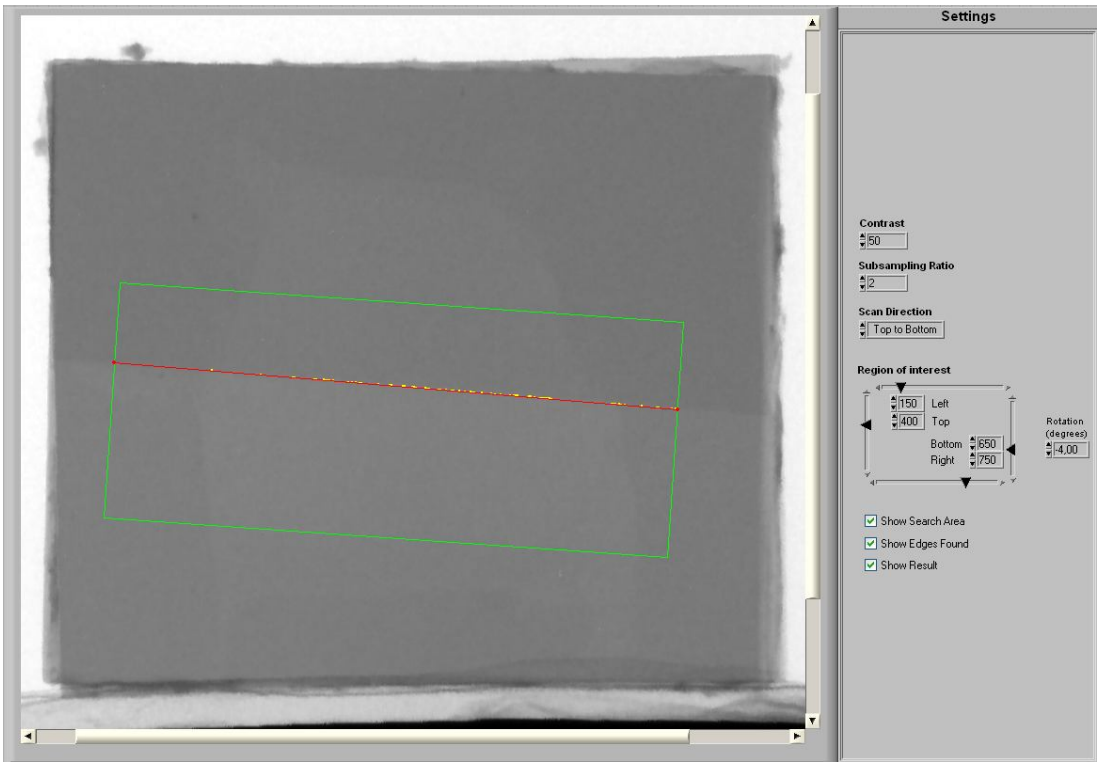

Figure 25. First part of the code implemented in LabVIEW. It allows to define the region of interest for detecting the edge and the assignment of values necessary for the detection: the contrast and the sampling ratio.

For each point of the edge, a line perpendicular to the edge and passing for the point is drawn. Averaging these curves, the ESF is then calculated. The graphs below report on the x axis the column of the image in terms of micron value, considering that each pixel side corresponds to the resolution chosen for the acquisition and on the y axis the intensity of the pixels.

From the derivative of the ESF, the LSF is obtained and then finally, from the Fourier transform of the LSF, the Modulation Transfer Function is calculated.

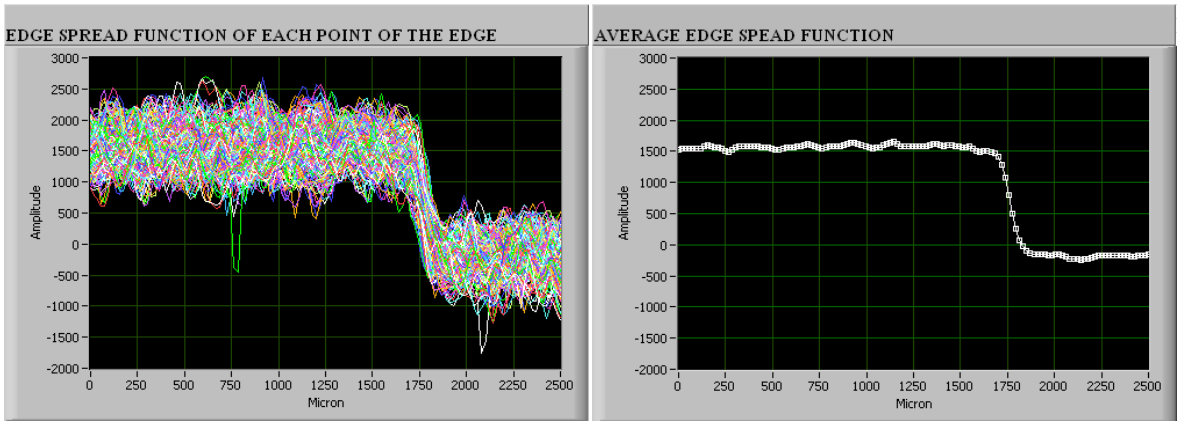

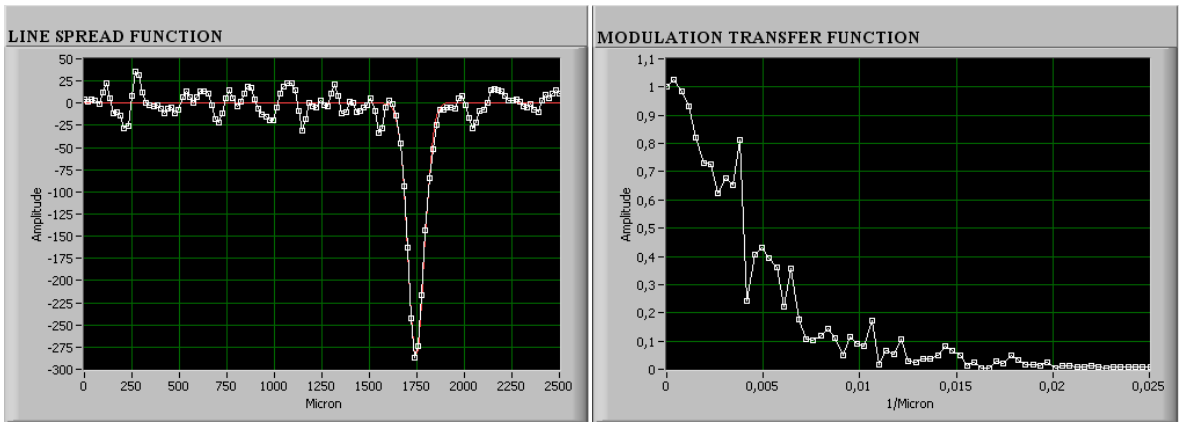

Figure 26. Results of the implemented code: a) ESF for each point of the edge; b) Average ESF of the edge device; c) LSF and d) MTF of the edge device

Ideally, the LSF of an edge is represented by a Dirac function; in the real case, the edge is not so precise and then the LSF is represented by a curve that can be assimilated to a gaussian-like function.

3.1.3 Results

Observing the Modulation Transfer Function resulting from this study, it is consistent with the MTF found in literature. The maximum value, equal to one, is in correspondence of the zero value on the horizontal axis, then the curve decreases with increasing spatial frequency. The main problem is related to the non uniformity of the edge which causes a jagged curve as it can be observed in Figure26d.

From the literature, it is known that the optimal condition for the calculation of the Modulation Transfer Function is represented by the placement of the object in contact with the detector. During the acquisition of the object, an increasing of the magnification corresponds to an increasing of the distance between phantom and detector. Theoretically, an increase of the magnification results in a falling of the MTF curve correspondent to a minor spatial frequency.

The value of spatial frequency relative to 10% of the MTF allows to correctly estimate the spatial resolution of the system. This value has been calculated for different values of the magnification, and the comparison of these values allows to know how the choice of the magnification can alter the spatial resolution of the system.

As result of the magnification increase, there is a decrease of the spatial frequency associated with the 10% MTF. From the graphs shown in Figure 27we can extract the value of the spatial frequency of our interest:

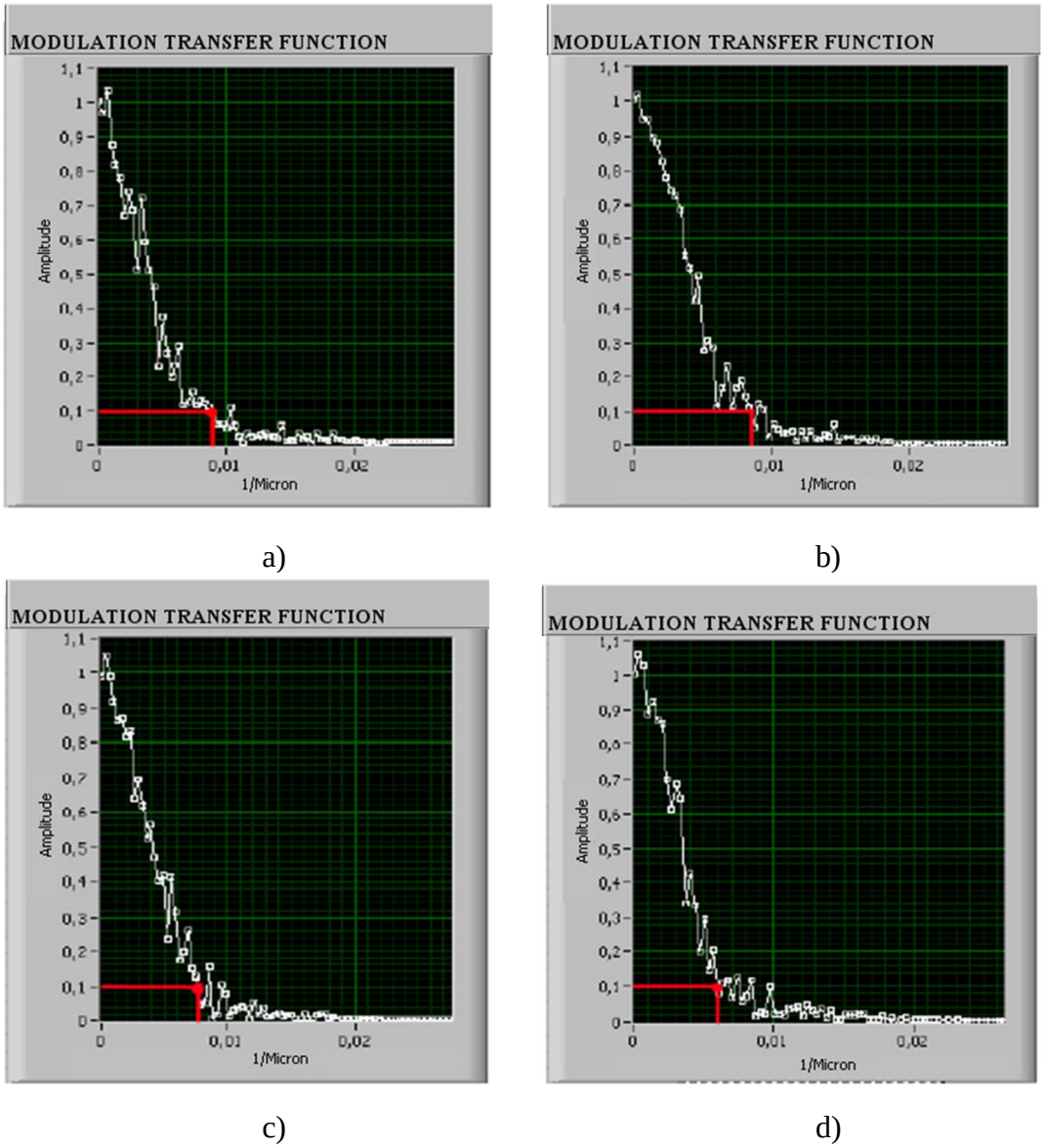

Figure 27. Modulation Transfer Function of the edge device for different values of the magnification: a) 15X, b) 35X, c)55X and d)75X

Starting from these values of spatial frequency, an estimation of the focal spot size dimension can be measured by the following formula:

$$a = \frac{1}{f(M-1)} \tag{3.5}$$

where M is the magnification value and f is the spatial frequency correspondent to the 10% of the MTF.

In Table 1 are reported the values of the spatial frequency correspondent to the 10% of the MTF and the consequent value of the focal spot size for several considered magnifications.

Magnification	Pixel size	10% MTF	Focal spot size
15 X	19,1 μm	0,009 μm^{-1}	7,936 μm
35 X	8,37 μm	0,0085 μm^{-1}	3,46 μm
55 X	5,33 μm	0,0078 μm^{-1}	2,374 μm
75 X	3,91 μm	0,0060 μm^{-1}	2,252 μm

Table 1. 10% MTF values and Focal spot size calculated for the different magnifications

As expected, the value of the spatial frequency relative to 10% MTF decreases with the increasing of the magnification. The declared value of the focal spot size of the Skyscan 1072 is 8 μm, and as has been supposed, results of this study show that the same value is calculated with the minimum magnification, placing the phantom as close as possible to the detector.

3.2. Influence of the beam hardening effect on Micro-CT images

Projection images coming out from a microtomographic acquisition must be processed in order to obtain the cross sections of the analyzed sample. Images reconstructed by a Micro-CT system can be distorted by some artefacts which have been widely discussed in paragraph 2.7. Considering the beam hardening effect the most damaging artifact for the image reconstruction, part of this research has been focused on its analysis.

The effect of beam hardening is due to polychromatic radiation. The beam, emitted by the X-ray tube, is composed of X-rays with a spectrum of different energies. The absorption coefficient is approximately proportional to the reverse of the beam energy and this implies that, passing through the patient, the lowest energy photons are preferentially absorbed. As a consequences, firstly a certain number of low energy photons contributes to increasing the dose of the patient without being useful for the image reconstruction and moreover, increasing the thickness of the crossed material, only the higher X-ray energies remain in the beam making the radiation less attenuated. Because of this, an underestimation of the value of the projection is detected.

Since the greylevels of the projection data are now not linear with the object thickness, the reconstruction produces quantitative errors and some visual distortions. In X-ray imaging the most common technique used for reducing beam hardening artifactis the placement of a ‘hardware’ filter in front of the X-ray source. The hardware filter, which is commonly a thin metal plate, reduces the low energy photons that are the predominant cause of this cupping artifact. In addition to hardware filtering, there are also several computational techniques to

reduce beam-hardening artifacts. The simplest is a widely implemented a priori, non-linear polynomial correction, during the post- processing of the images.

3.2.1 Materials and methods

The best way for the comprehension of the influence of beam hardening on images is to firstly understand how the images are reconstructed. Then, the back projection algorithm, described in paragraph 2.6, has been implemented in LabVIEW (vers.8.2). In order to do this, two codes have been implemented: the first one allows to obtain projections of the object which in this case is a two-dimensional image and the second one allows to re-obtained the initial image.

The first code simulates the irradiation of the object by an x-rays parallel beam. The object is rotated for an angle of 180 degrees with an angular step of 1 degree. In this way, a projection of the object for each angle is obtained.

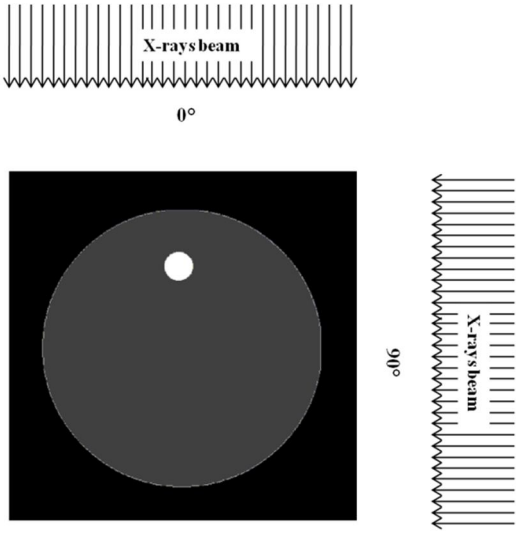

Figure 28. Irradiation of the phantom image for different angle of the scan beam

To obtained the reconstruction of the initial image, projections must be re-projected by the second code. Each profile is firstly filtered with a Kernel filter and then summarized to obtain the intensity value in each point of the image.

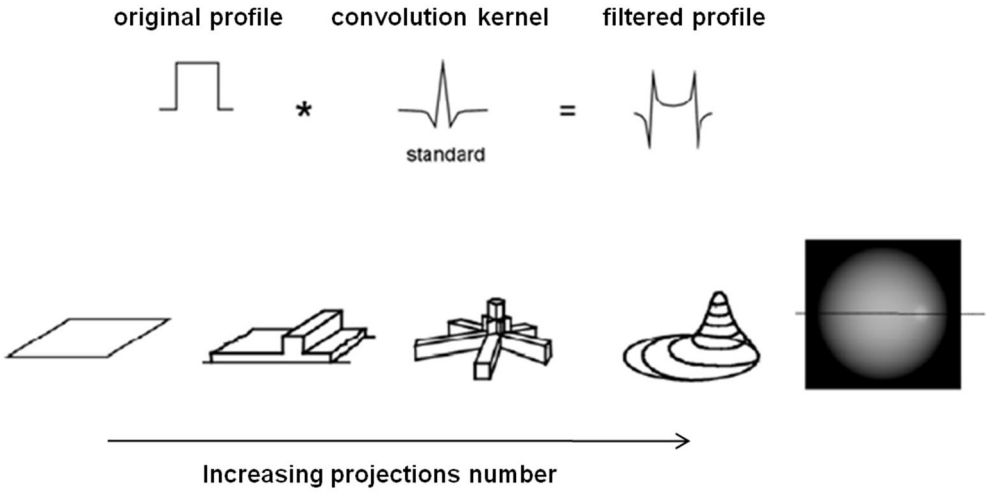

Figure 29. Schematic representation of the filtered re-projections

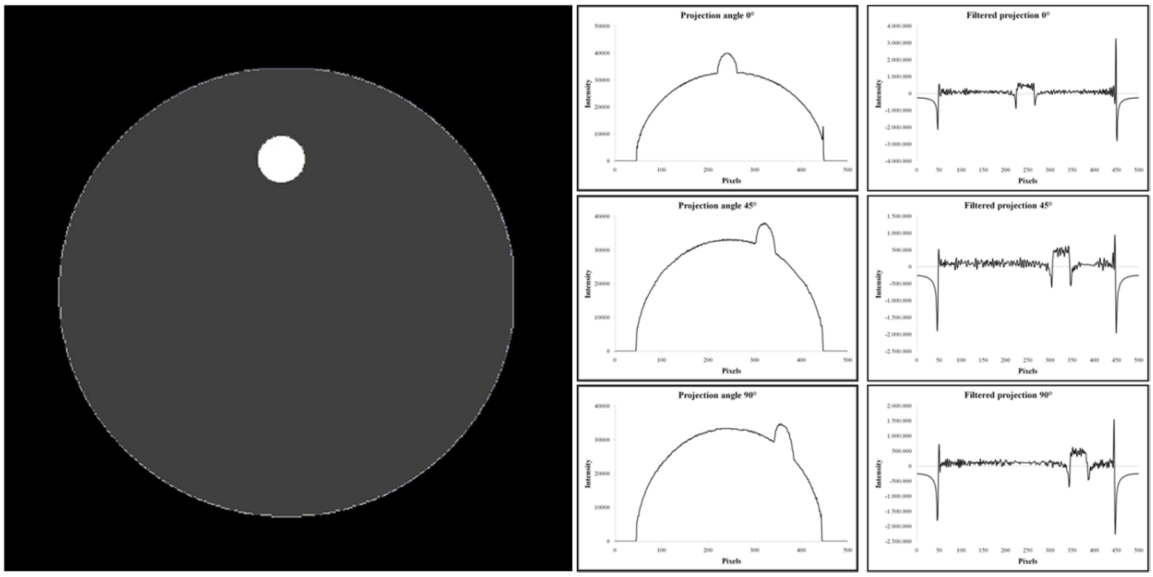

Figure 30. Projections and filtered projections of the phantom image for three scan angles as examples: 0°, 45°, 90°

Depending on the number of projections available, the reconstructed image is more or less accurate. In Figure 31 is reported the reconstruction of the image considering different number of projections.

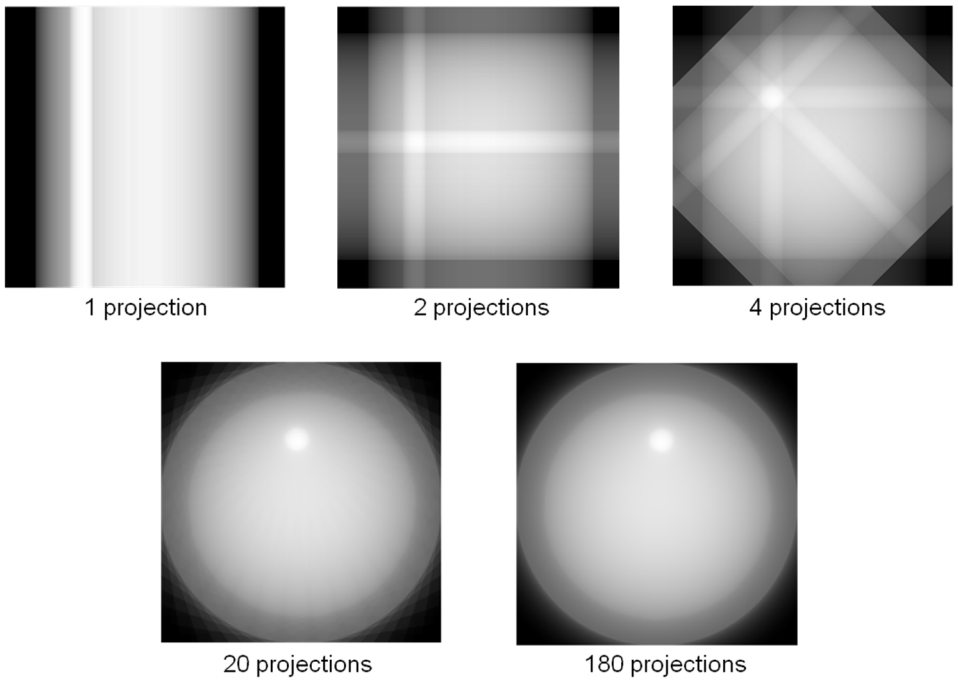

Figure 31. Image reconstructed with a different number of projections: 1, 2, 4, 20, 180 projections. High accuracy of details in the reconstructed image is achieved increasing the number of projections considered.

As reported in the figure below, image resulting is similar to the initial image, differences are in the grey level scale and in the grey crown surronding the image. This artefact is created by the rotation of the image. During the rotation, the borders of the objects become blurred and this blurring creates the grey crown.

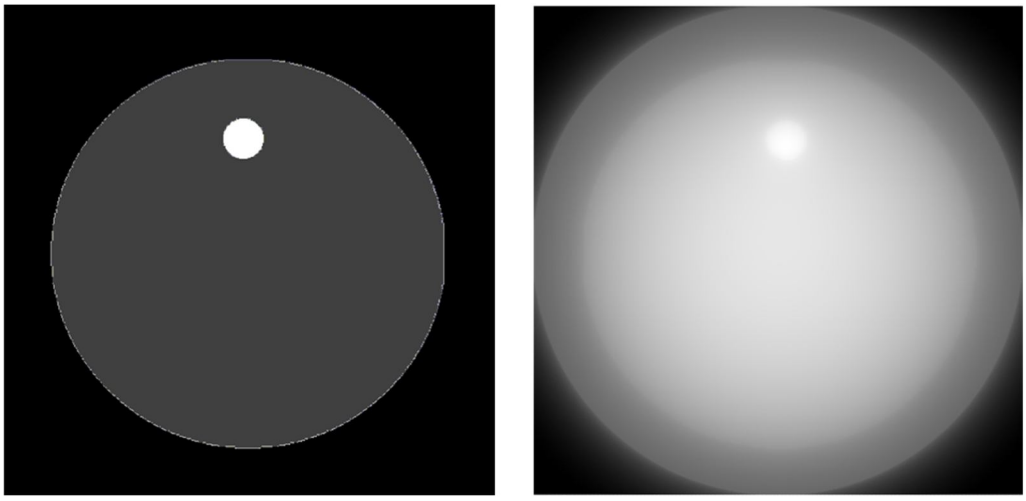

Figure 32. Comparison of phantom image and image reconstructed by the back-projection algorithm implemented in LabVIEW

After the implementation and verification of the program, the beam hardening issue has been studied[54][55][56][57][58].

As described above, the beam hardening effect can be corrected by a previous filtration during the acquisition step and a following correction software. The Skyscan 1072 allows a previous filtration inserting a filter of 1 mm of Aluminum between the X-rays tube and the object and then a second correction in the images reconstruction step. A dedicated software NRecon (Version 1.6.6, Skyscan) allows to choose a parameter for the correction of the beam hardening. This option compensates beam-hardening effect by a linear transformation in the software. A five order polynomial function is used to do beam hardening correction. Depth of correction (0, 1, ..., 100) can be selected according to the object density. The visualization of the resulting images helps the operator for the choice of the corrected value. A block for the correction of beam hardening has been inserted in the back-projection algorithm implemented in LabVIEW in order to verify the accuracy of the software NRecon used for the reconstruction.

Since the aim of this study is the evaluation of the accuracy of the micro-tomography on bone analysis, the sample chosen for this analysis is a phantom of Hydroxyapatite, which is the major component of bone. A disc of hydroxyapatite, with diameter of7 mm and thick of 3 mm, has been acquired using Skyscan 1072® micro-CT Scanner. The acquisition parameters were set at 100 kV and 98 µA, which means with the maximum power source. A resolution value of 11.72 µm was chosen in order to acquire all the sample. Projections were acquired with an angular step of 0,45° over an angular range of 180°. Using NRecon (Version 1.6.6, Skyscan)a dedicated software based on the Feldkamp algorithm[39], from these projection images in TIFF format, transversal sections of the specimen in BMP format are obtained. The distance between two consecutive sections is the double of the resolution chosen for the acquisition.

In order to eliminate the presence of other artifact, mainly present at the edges of the sample, the central slice has been chosen for the analysis.

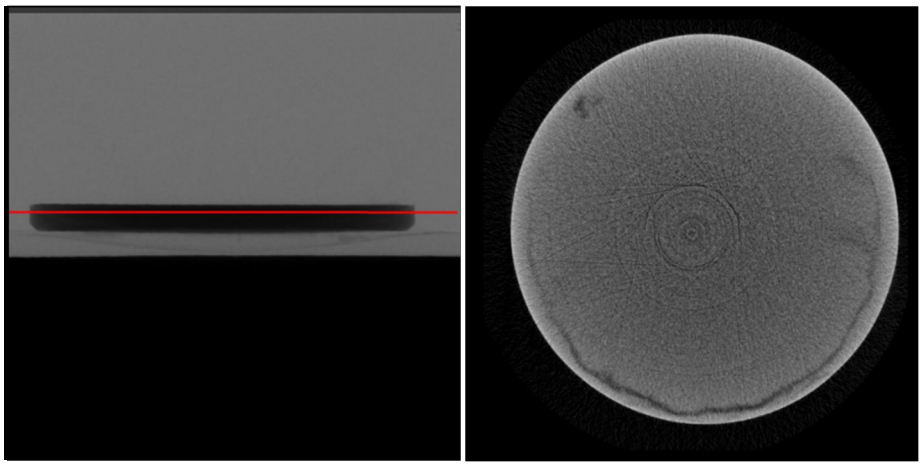

Figure 33. a) Projection of the Hydroxyapatite phantom; b) Cross-sectional image of the phantom, correspondent to the plane highlighted with a red line, reconstructed without the correction of beam hardening

The image reconstructed without the beam hardening correction has been used as input of the code implemented in LabVIEW. In the figure below are reported the input image and the output image of our implementation.

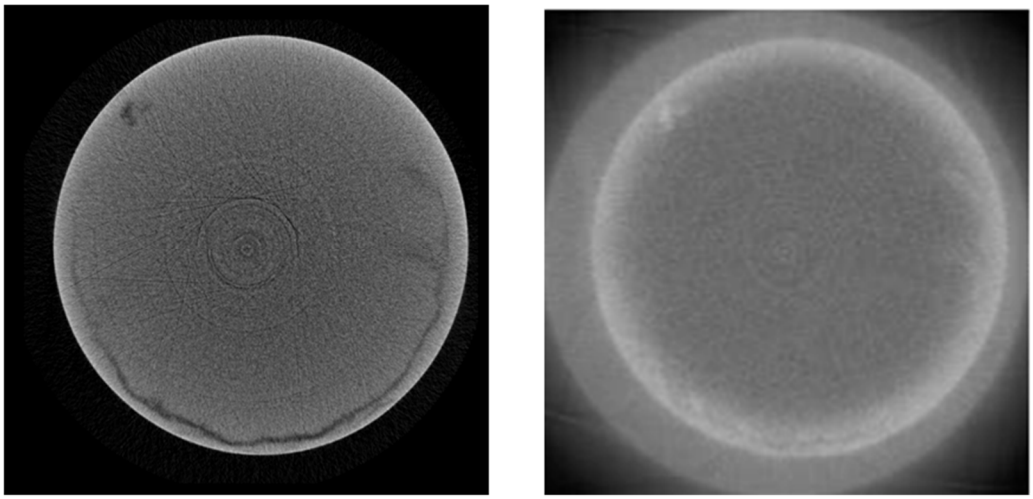

Figure 34. a) Central cross-sectional image obtained by the Skyscan acquisition and b) the same image reconstructed with the back-projection algorithm implemented

The block for the beam hardening correction implemented in the software allows to correct the effect with a percentage in the range 0 - 100% and the percentages chosen for the analysis are: 0%, 20%, 50% and 80%.

The same analysis have been done with both the Skyscan dedicated software NRecon and the implemented software in LabVIEW.

The sample analysed is a compact hydroxyapatite disc, then in order to evaluate the influence of the beam hardening effect on the results, the attenuation profile along the diameter of the disc has been studied. Results of both software are reported below.

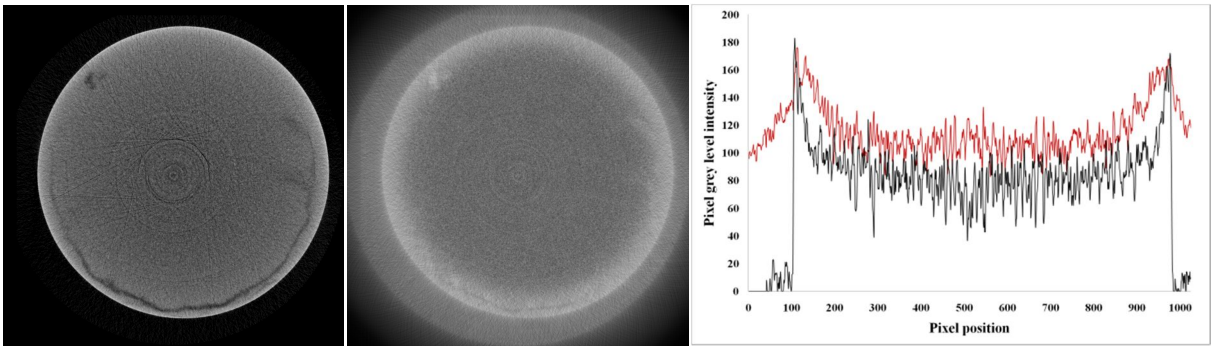

a) **b)** **c)**

Figure 35. Images without beam hardening correction from:(a) the dedicated software of Skyscan NRecon, (b) the code implemented in LabVIEW. (c) Profiles of the attenuation along the diameter of the sample (in black, profile of the first image, in red profile of the second one)

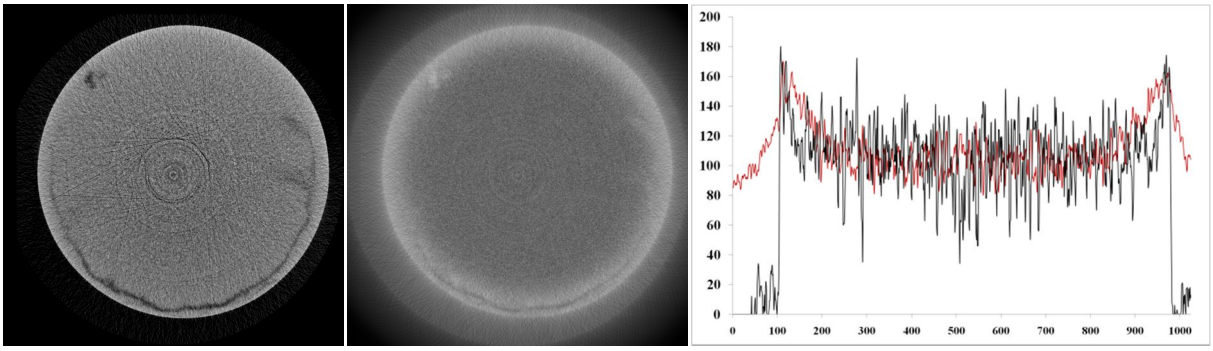

a) **b)** **c)**

Figure 36. Images with a 20% beam hardening correction from:(a) the dedicated software of Skyscan NRecon, (b) the code implemented in LabVIEW. (c) Profiles of the attenuation along the diameter of the sample (in black, profile of the first image, in red profile of the second one)

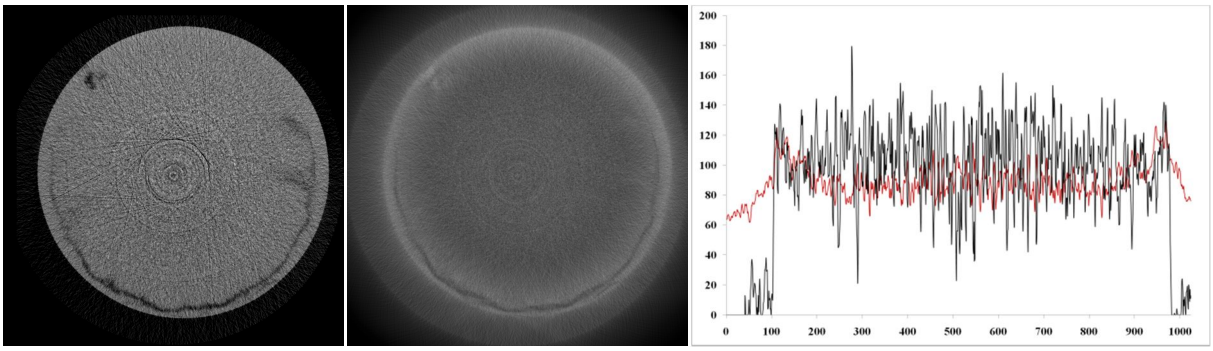

a) **b)** **c)**

Figure 37. Images with a 50% beam hardening correction from:(a) the dedicated software of Skyscan NRecon, (b) the code implemented in LabVIEW. (c) Profiles of the attenuation along the diameter of the sample (in black, profile of the first image, in red profile of the second one)

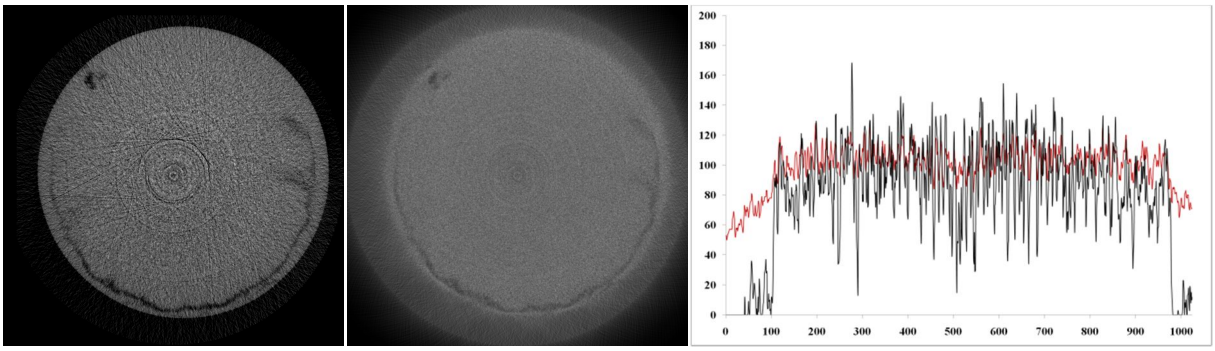

a) **b)** **c)**

Figure 38. Images with a 80% beam hardening correction from:(a) the dedicated software of Skyscan NRecon, (b) the code implemented in LabVIEW. (c) Profiles of the attenuation along the diameter of the sample (in black, profile of the first image, in red profile of the second one)

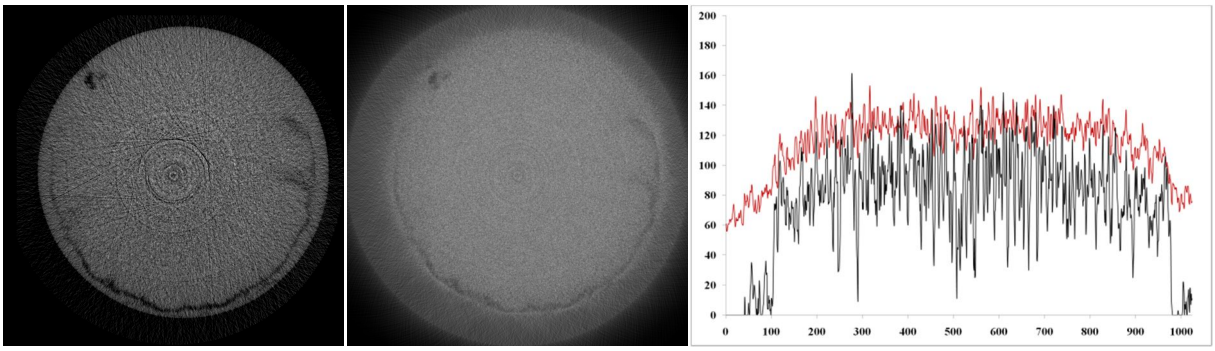

a) **b)** **c)**

Figure 39. Images with a 100% beam hardening correction from:(a) the dedicated software of Skyscan NRecon, (b) the code implemented in LabVIEW. (c) Profiles of the attenuation along the diameter of the sample (in black, profile of the first image, in red profile of the second one)

3.2.3 Results

From the comparison of the results, a good correlation can be defined. As it can be seen, attenuation profiles have the same trend. The difference observable at the beginning and at the end of all the profiles is due to the presence of the grey crown in the LabVIEW evaluation but it doesn't affect the reconstruction in the region of interest of the sample.

Since the good accuracy of the software in the beam hardening correction has been verified, results have been analysed in order to establish the correct value of correction in the analysis of bone sample. Theoretically, being the sample homogeneous and composed of only hydroxyapatite, the profile must be linear. Each profile has been interpolated with a polynomial function and the 50% correction showed the most linear function.

3.3. Conclusions

Accurate measurement of modulation transfer function (MTF) of an x-ray micro-CT system is essential for various purposes such as to determine scanner resolution or to retrieve further information about a scanned object by image-processing. In this study, a new method for MTF measurement is proposed. An edge device constructed in our laboratory has been acquired by the Micro-CT Skyscan 1072 in order to calculate the Edge Spread Function of the imaging system. From the ESF, thanks to a proper code implemented in LabVIEW, the MTF of the system has been evaluated. The focal spot size calculated from the resulting MTF was compared with the value declared by the Skyscan. This study has been repeated for different values of the magnification and a good match on the results has been found for the minimum magnification value, which means the position of the object in contact with the detector.

Focusing on the second step of a microtomographic acquisition, artifacts coming out from the reconstruction of the images have been studied. Considering the beam hardening as the most influent artifact on the images quantification measurements, it has been analyzed in order to properly correct it in the subsequent analysis of bone samples. The back-projection algorithm normally used for the reconstruction of Micro-CT images has been implemented in LabVIEW, a block for the correction of the beam hardening effect has been inserted and a slice of a Hydroxyapatite disc has been analyzed. The code implemented and the dedicated software of the Skyscan NRecon were used for the reconstruction of the sample with different percentages of beam hardening correction. Observing profiles of the reconstructed images, in both of the method a 50% of correction for the beam hardening correction has been detected as the most suitable for the bone analysis.

Considering results obtained from both the studies, the calculation of the Modulation Transfer Function and the beam hardening analysis, the accuracy of the Micro-CT Skyscan 1072 has been verified, at least for the issues interesting in this research.

CHAPTER 4

Implementation of a new method for bone volume measurement from Micro-CT images

The previous study on the accuracy of the microtomograph Skyscan 1072 reported in Chapter 3 has been necessary in order to start the main issue of this research, the development of a new method for the calculation of the volume of bone samples from the images analysis.

One of the main problem of bone analysis by micro-CT is the processing of the reconstructed cross-sections images for the sample morphometric analysis. The calculation of morphometric parameters, such as bone volume or trabecular properties usually requires a process named binarization of the images which consists on the definition of a threshold value of grey-level, necessary to distinguish bone from background. The choice of this value is a crucial task since a standard method doesn't exist. Another problem arising from the binarization is related to the inhomogeneity of bone. From the binarization process, each voxel is associated to bone or air, not considering that each voxel of the acquired image can be composed by both of them. This effect is called Partial Volume Effect and it affects especially voxels at the edges of the analyzed sample.

In order to avoid these problems, the aim of this study is the evaluation of a new method for the histomorphometric analysis of bone sample from the processing of the grey level images. This method is based on the histogram analysis and provides the splitting of the histogram in three different populations: pixels marked as bone, pixels marked as air and a third population of pixels that cannot be statistically referred to bone or air. A statistical analysis was then used in order to calculate the volume of bone sample[59][60][61][62][63].

4.1. Micro-CT images post-processing: binarization issue

Considering a generic sample of homogeneous material, its histogram is composed of two peaks, the first one centered in the greylevel correspondent to the material and the second one, representing the avoid space, centered in the last value of the histogram. In this case, the volume of the sample could be calculated as the product between the volume of a voxel and the number of material voxels (calculated from the first peak).

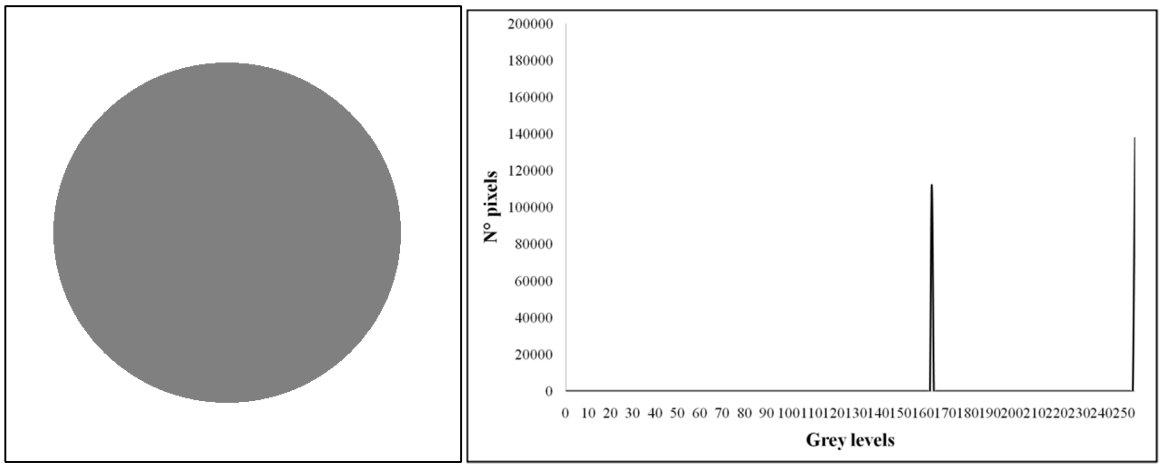

Figure 40. Histogram of a generic homogeneous material

Considering bone, it is not homogeneous and its inhomogeneity implies bone voxels represented by more than one grey level. Because of bone inhomogeneity, the grey level histogram of a bone image is composed of two ideal pulses (considering air as a second material) spread over the entire range of grey levels.

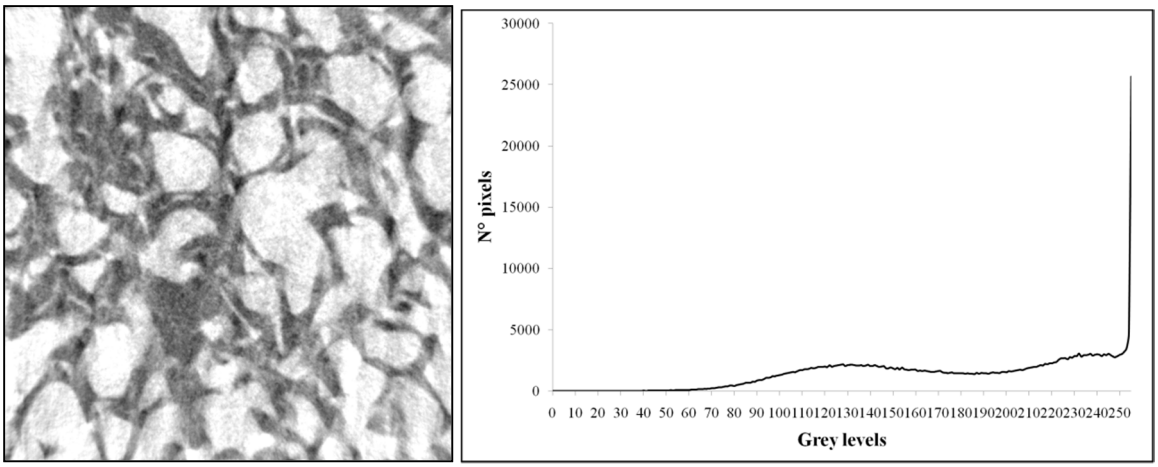

Figure 41. Slice of a cubic bone sample and its grey levels histogram

Observing the histogram, it is reasonable to choose as threshold value the minimum between two peaks. This minimum is not always clear, usually there is a region between peaks in which the histogram has a constant value and in this region the correct threshold can be detected. In order to understand the influence of this choice on the subsequent analysis, observing the histogram of the image in Figure 41, the threshold value could be chosen in the grey levels range 170-210.In Figure 42 are reported the image binarized with threshold value 170, 180, 190, 200, 210.

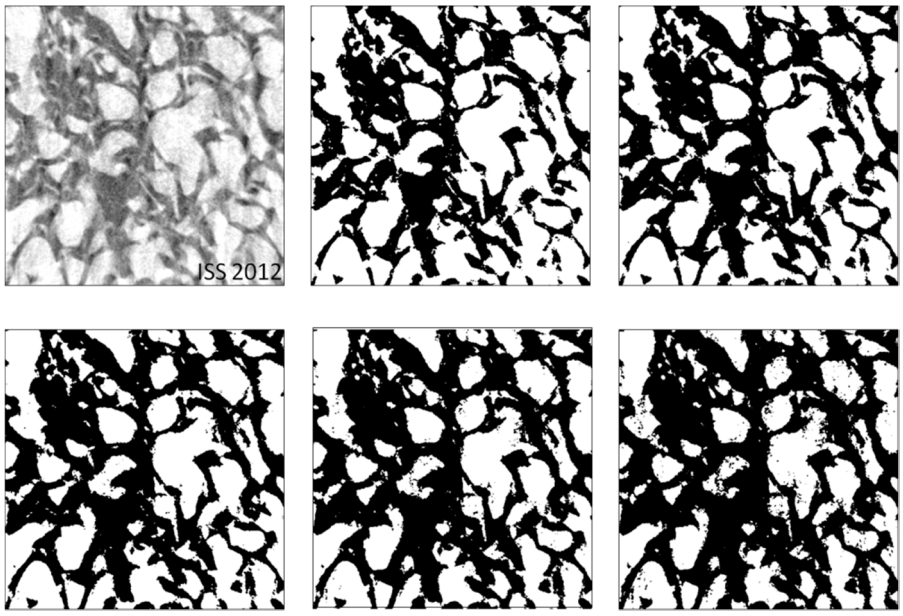

Figure 42. Cross sectional image of a bone sample and its binarization with five different threshold values chosen in the region between two peaks: 170, 180, 190, 200 and 210

From these figures, it can be observed how the wrong choice of the threshold may lead to an apparent increase or decrease of bone mass. In order to obtain a quantitative analysis of the variation of the histomorphometric parameters respect to the threshold value, the dedicated software CT-Analyser has been used to calculate the bone volume of the cubic bone sample. Ct-Analyser calculates the volume of the object under investigation using the marching cubes volume model of the binarized objects within the Volume of Interest. The marching cubes algorithm is usually used to process 3D medical data. It creates triangle models of constant density surfaces from data. Using a divide-and-conquer approach to generate inter-slice connectivity, it creates a case table that defines triangle topology. The algorithm processes the 3D medical data in scan-line order and calculates triangle vertices using linear interpolation. The gradient of the original data is normalized and used as a basis for shading the models. The detail

in images produced from the generated surface models is the result of maintaining the inter-slice connectivity, surface data, and gradient information present in the original 3D data.

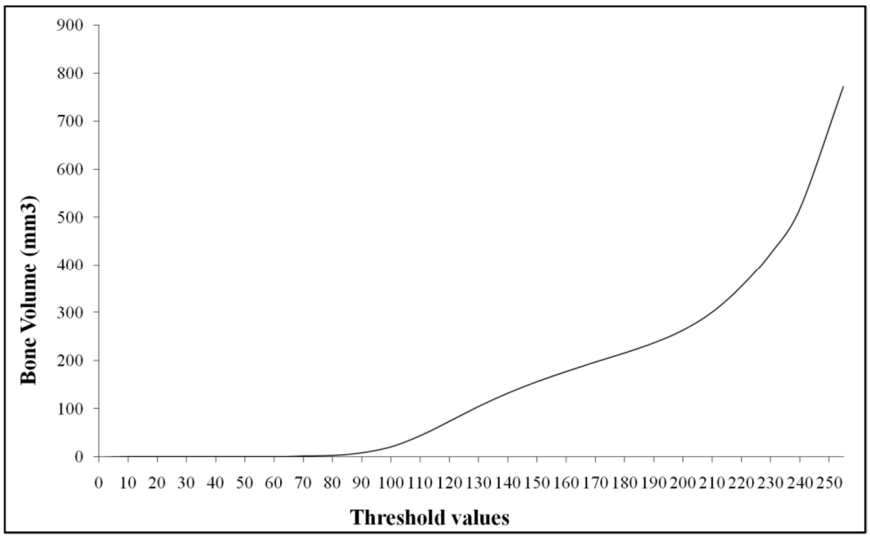

Figure 43. Bone volume measurement with a dedicated software of Skyscan respect to threshold value of binarization

The graph shows an increasing trend, explained by the fact that increasing the threshold value, the number of pixels considered as bone mass increases. A central area more linear can be detected and the most suitable threshold value must be chosen in this area. Unfortunately, in this area no singularity can be found to provide useful indications for the determination of the best threshold value so other criteria for the choice must be considered. [64]

4.2. Methods for threshold definition in images binarization

M. Ding, et al. calculates threshold value by an adaptive method which consists on the segmentation of greylevel data at different thresholds. The correct threshold is then chosen considering where the volume fraction changes the least. Other parameters can be considered to define the threshold value. For example, observing that in a certain range of grey levels, density connectivity have a constant value and structure model index is linear, the mean value of this range can be chosen as threshold value [65][66][67]. The adaptive thresholding method calculates local thresholds, considering not the complete image but limited regions. For example, starting from a voxel located on the border between solid and empty space, a string of pixels for three orthogonal directions is considered, and for each string, the histogram of gray levels is calculated. A local threshold at an intermediate point between the maximum and the minimum of

each histogram is identified, in this way for each voxel three local thresholds are defined and by the average of the three values the final threshold is determined.

Otsu algorithm is usually used to define the correct threshold. The definition of a threshold implies the separation of the grey levels image in two classes, object and background. The characteristics of these two classes are analyzed to evaluate the correct threshold *s*.

Considering the normalized histogram of the image in the form of:

$$p(k) = \frac{h(k)}{\sum_{k=1}^{2^b-1} h(k)} \tag{4.1}$$

For a fixed value of the threshold *s*, the distribution of grey levels is divided in two classes K_0 and K_1. The probability of a pixel belonging to the classes is:

$$P_0 = \sum_{k=0}^{s} p(k), \quad P_1 = \sum_{k=s+1}^{2^b-1} p(k) = 1 - P_0 \tag{4.2)(4.3}$$

The mean grey level values in the two classes are:

$$m_0 = \sum_{k=0}^{s} kp(k), \quad m_1 = \sum_{k=s+1}^{2^b-1} kp(k) \tag{4.4)(4.5}$$

and consequently, the mean grey level of the total image can be calculated as:

$$m = P_0 m_0 + P_1 m_1 \tag{4.6}$$

The variances of the two classes are:

$$\sigma_0^2 = \sum_{k=0}^{s} (k - m_0)^2 p(k), \quad \sigma_1^2 = \sum_{k=s+1}^{2^b-1} (k - m_1)^2 p(k) \tag{4.7)(4.8}$$

From these parameters, the between variance and the within variance are calculated as:

$$\sigma_B^2 = P_0(m_0 - m)^2 + P_1(m_1 - m)^2, \quad \sigma_W^2 = P_0{\sigma_0}^2 + P_1{\sigma_1}^2 \tag{4.9)(4.10}$$

Considering the between variance a measure of the separation of the classes and the within variance a measure of their consistence, threshold is chosen as the value of *s* which gives a maximum separation and consistence. Threshold value is chosen in order to maximize the ratio:

$$\eta(s) = \frac{\sigma_B^2(s)}{\sigma_W^2} \tag{4.11}$$

All of the methods presented above allow to define a threshold value for the image binarization. A correct binarization of the image is important since it allows a correct reading of the images. In medical application , for example in diagnosis of patologies in which is important the highlighting of detail with different density.

The aim of this research is not the definition of this threshold but the development of a new method for the direct measurement of morphometric parameter. The morphometric parameter take into account is the bone volume.

In this issue, Laidlaw et. al. presented a new algorithm for identifying the distribution of different material types in volumetric datasets such as those produced with Magnetic Resonance Imaging (MRI) or Computed Tomography (CT). This study started from the assumption that, due to partial volume effects, a single voxel can contain more than one material. A voxel is considered as a region instead of a single point and using Bayesian probability theory, the highest probability combination of materials within each voxel-sized region is estimated. Using information from neighboring voxels, a continuous function is reconstructed and considering the values that this function takes on within a voxel, an histogram of this function over the voxel is created. Assuming that each voxel can contain a mixture of different materials, basic functions modeling histograms of voxels is extracted. Fitting a linear combinations of these basic functions to each voxel, the most likely combination of materials can be probabilistically chosen[68].

4.3. Previous study for the Micro-CT bone volume calculation

In a previous study[69], a different method was implemented in order to define the threshold value for the binarization and calculate bone volume of the samples.

A cubic bone sample extracted from the femoral head of a patient subjected to a surgery has been acquired by the micro-tomography Skyscan 1072. A dedicated software, Nrecon (Version 1.6.6, Skyscan), has been used for the reconstruction of the images and the grey levels histogram of a single slice of the sample has been analyzed.

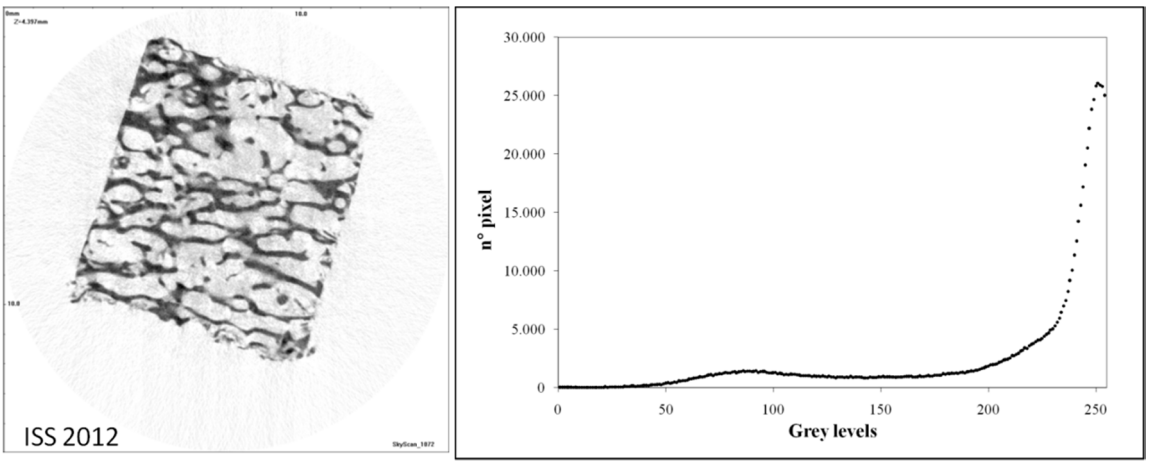

Figure 44. CT image of a trabecular bone sample and its grey levels histogram

The overall histogram is the result of three contributions from three homogeneous regions, observable in the image:

1. Region of the avoid space outside of the sample.
2. Region of the avoid space inside of the sample.
3. Region of bone.

The histogram of each homogeneous region has been analyzed.

The histogram of the external avoid space area can be assimilated to a narrow normal distribution in the range of 240-255 grey levels, having expected value equal to 255.

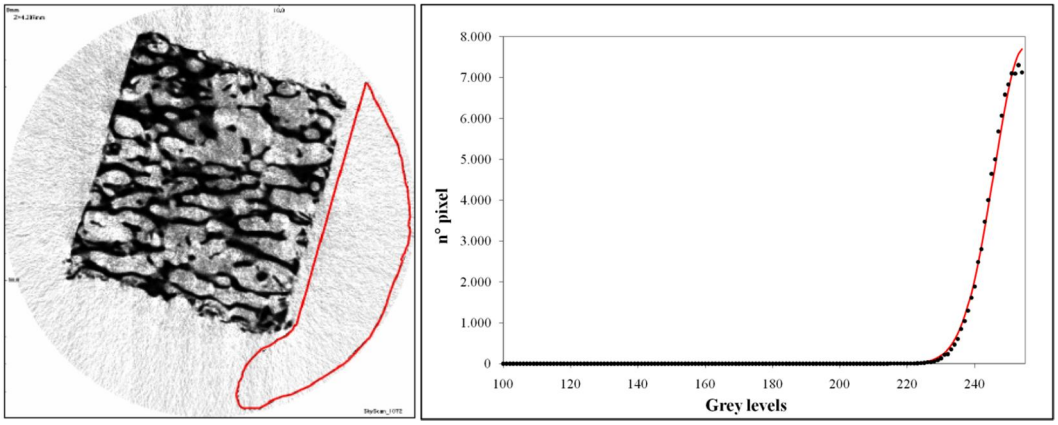

Figure 45. a) CT image of a trabecular bone slice. In red is highlighted the external region considered; b) Grey level histogram of the considered region, the red curve represents the Gaussian that fit the experimental data

Even the histogram of the internal avoid region can be approximated to a normal distribution centered around the grey level 230 and less narrow than the previous. It is more wide than the previous because, together with the noise introduced by the algorithm of backprojection, another artifact has to be considered: the partial volume effect on the border regions of the materials.

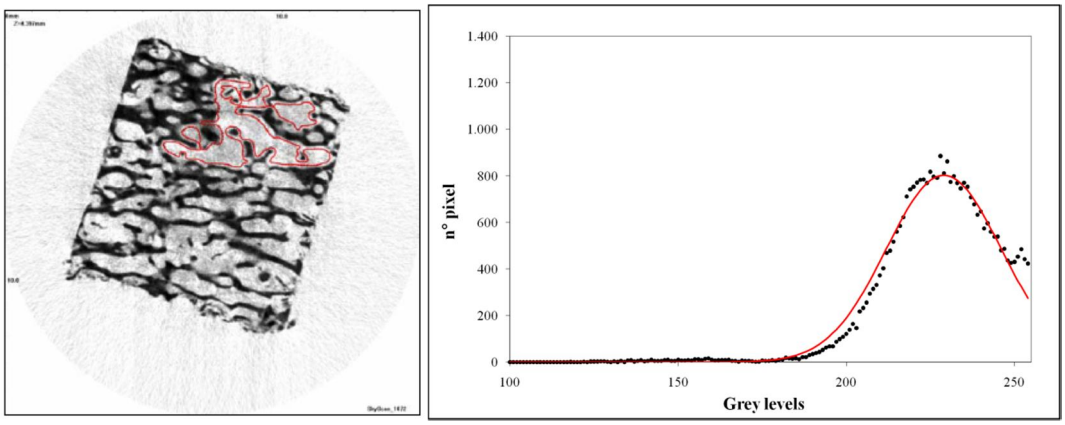

Figure 46. a) CT image of a trabecular bone slice. In red is highlighted the internal avoid region considered; b) Grey level histogram of the considered region, the red curve represents the Gaussian that fit the experimental data

Finally, the histogram of the bone region can be approximated to another normal distribution but in this case, the width of the curve is due to the inhomogeneity of bone tissue, more grey levels correspond to the same material.

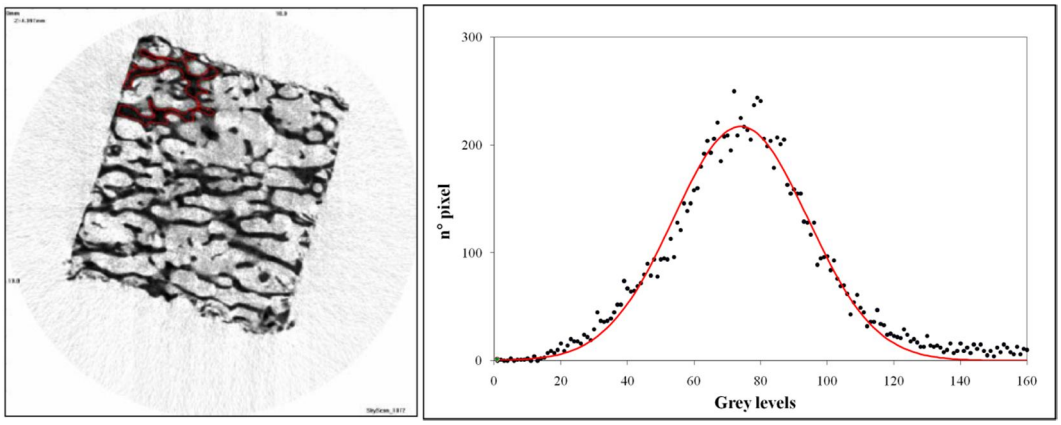

Figure 47. a) CT image of a trabecular bone slice. In red is highlighted the bone region considered; b) Grey level histogram of the considered region, the red curve represents the Gaussian that fit the experimental data

Observing the image, information useful for determining the threshold is contained in the region occupied by the sample bone, then the area of the external avoid space can be discarded. The Region of Interest (ROI) of the image considered for the evaluation of the histogram is highlighted in red in the figure below.

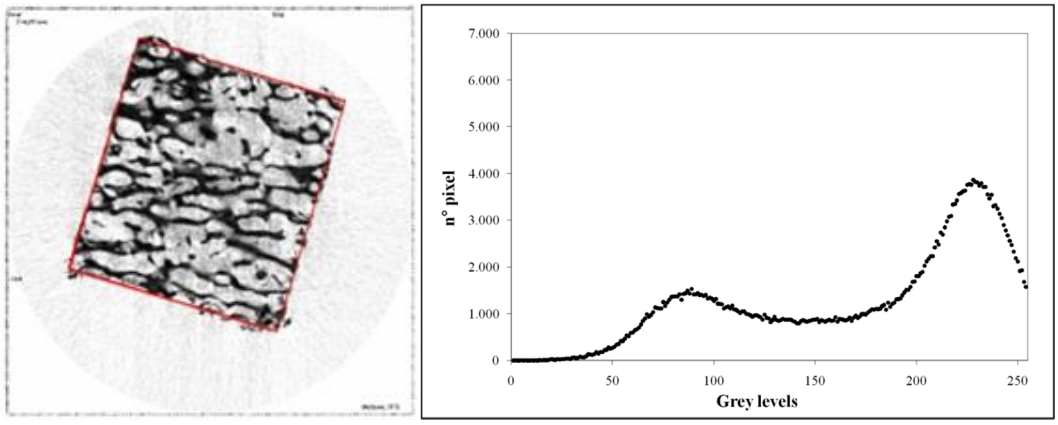

Figure 48. a) Region of interest of the CT image for the trabecular bone slice; b) Grey level histogram of the considered region

This consideration leads to the disappearance of the corresponding normal distribution on the total histogram so, in a first approximation, histogram consists of only two distribution: the first one corresponding to bone and the second one corresponding to the avoid space between bone.

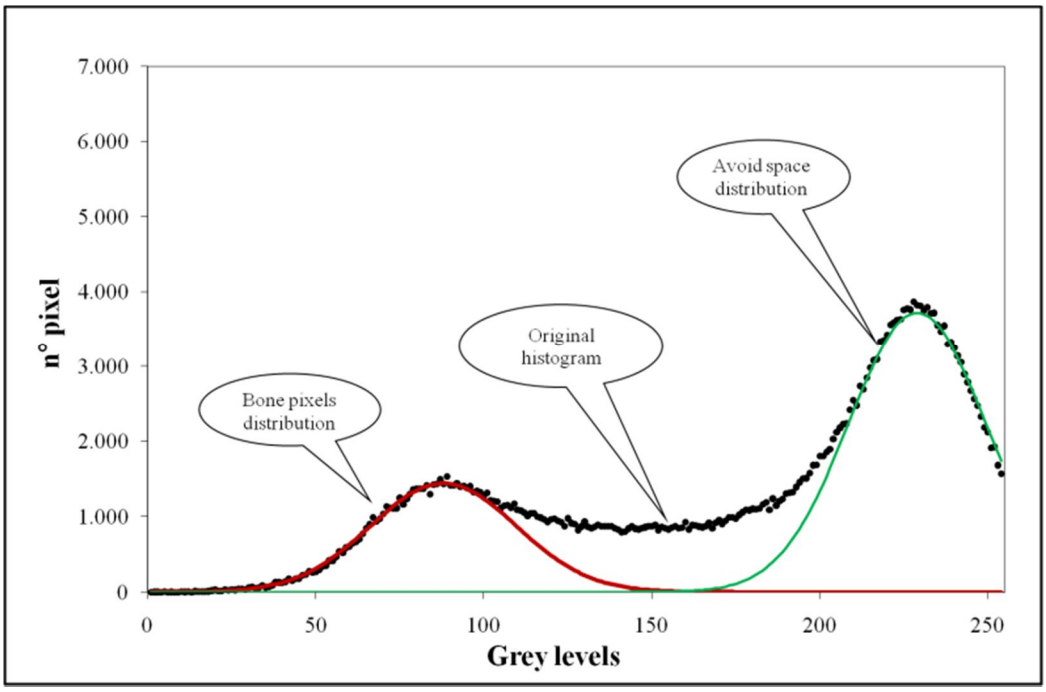

Figure 49. Normal distributions approximating the distribution of the observed datawith method of the minimum standard deviation.

As it can be seen in the graph above, there is a good correlation between the histogram and the approximating normal distributions. The intermediate region, which is not fitted by the distributions, represents pixels not associated with defined regions. Considering the histogram in Figure 49, this region is composed of pixels with a grey-level intensity comprised in the range105 ÷ 208 and in order to classify this population, only these pixels are displayed in the image below.

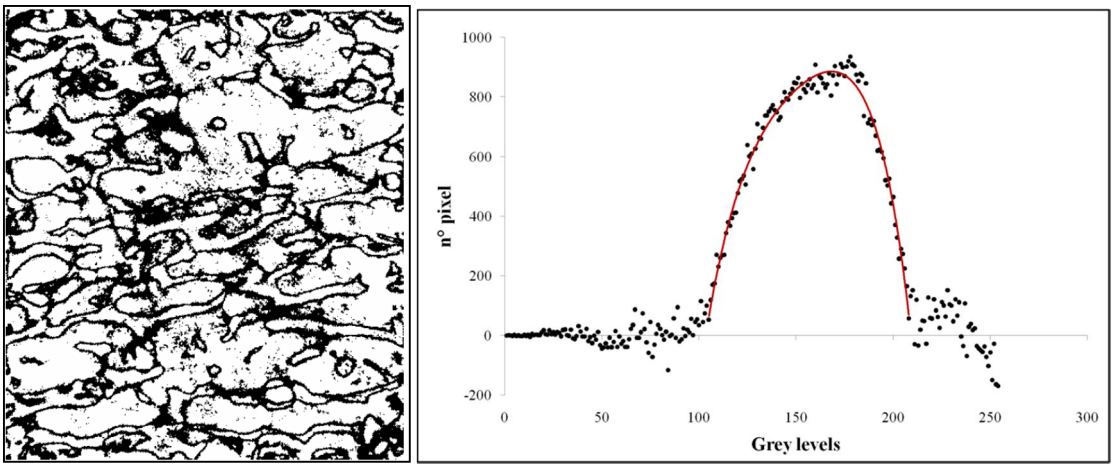

Figure 50. a) Pixels not belonging to the two main distributions of bone and no-bone; b) Grey levels histogram of these pixels and its best approximation with a polynomial function (red curve)

Despite a few pixels attributable to the artifacts that affect the image during the reconstruction, these pixels belong to the border area between bone and empty space so they can be assimilated to the Partial Volume effect. The threshold value for the binarization of the image must be chosen in this region and the choice must be taken in order to allow the better redistribution of these border pixels to the populations of bone and empty space.

To isolate this population of pixels, the normal distributions of bone and empty space have been subtracted from the total histogram and the best approximating polynomial of this curve has been calculated using the method of least squares. (Figure 50)

Assuming pixels of this intermediate population correspond to pixels at the border region between bone and avoid space, it is reasonable to divide them equally between the two populations. The grey level which allows to divide in equal parts the number of pixels of the border population has been chosen as threshold value.

This method is theoretically applicable in all cases to define histomorphometric parameters such as the volume of a bone sample. Although, the procedure illustrated above is related to a single slice of the sample. From a Micro-CT analysis, the sample is described by a few hundred slices, which are different from each other because of the irregularities of the trabecular structure and the inhomogeneity of the bone tissue. Each slice could have a different optimal threshold value, so the choice of the same value for all of them could cause an error in the estimation of the parameter.

4.4. Implementation of a new method for bone volume measurement from Micro-CT images analysis

The basic concepts of this previous study have been used, together with some theories of Laidlaw's study as references for the evaluation of a new method to measure the volume of bone samples without the binarization of the images. This algorithm allows to calculate the bone volume by the direct analysis of the grey levels histogram of the images.

In order to verify the accuracy of the implemented method, the volume of the bone specimens were also measured by an Helium pycnometer (mod. AccuPyc II 1340 Micromeritics-GA, USA).

4.4.1 Materials and Methods

Specimens microtomographic acquisition

Nineteen trabecular bone specimens were extracted from femoral heads of eight patients subject to a hip arthroplasty surgery. After being catalogued, specimens were preserved in a freezer at 10 °C for about a month. From the middle of the femur capita of each specimen a slice of about 10 mm of thickness corresponding to the frontal plane was obtained and then these slices were kept 10 hours in a freezer. Subsequently, slices were subjected to three complete cycles of dehydration with aqueous solutions having crescent percentage of ethanol, severally 70%, 90% and 99,9%, in order to defatted them. Between the dehydratation cycles, specimens were kept in a refrigerator for about 10 hours. Slices were then cut with a diamond belt saw (EXTEC Labcut 1010, Enfield CT) in order to obtain cubic specimens of about 6 mm. These specimens were further dehydrated and defatted by other three cycles with ethanol as previously described.

Trabecular bone specimens were acquired using a Skyscan 1072® micro-CT Scanner[21]. The acquisition parameters were set at 100 kV and 98 µA, with 1 mm of aluminum filter and with an isotropic voxel size in the range of 11.24 µm-14,66 µm. An angular step of 0,45° was used and 400 projections were acquired over an angular range of 180°. The cross-sectional images of samples were obtained using NRecon, a dedicated software based on the Feldkamp algorithm. From the study on the beam hardening correction reported in the third chapter, the 50% of correction resulted the greatest value in bone analysis so this value has been chosen for the reconstruction.

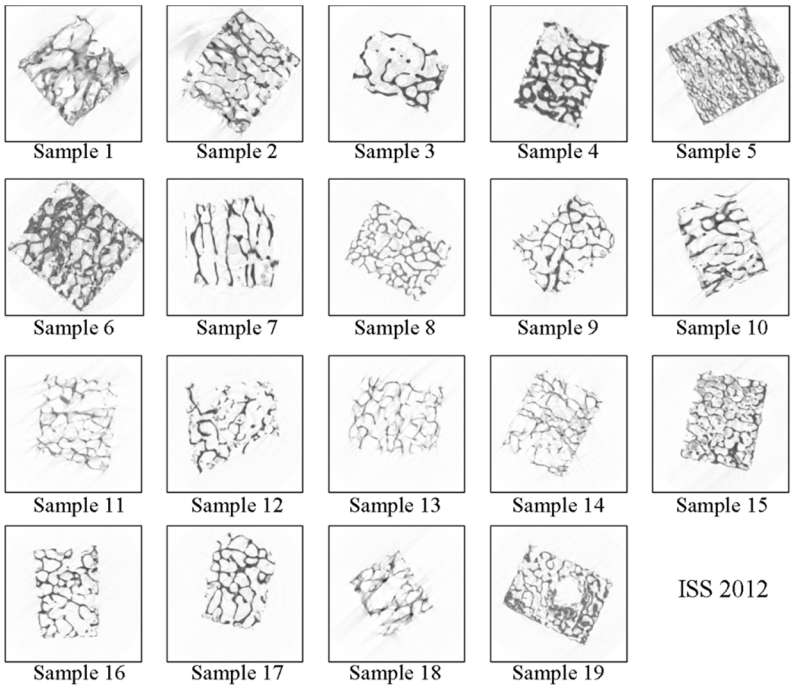

Figure 51. A single slice for each of the nineteen trabecular bone sample under investigation. Slices have been obtained with the dedicated NRecon software

After the reconstruction, data were processed by a software of Skyscan®, named Ct-Analyzer®(Version 1.11, Skyscan). This software allows to obtain histomorphometric parameters of the specimens. The main interesting parameters for the description of bone architecture are:

- Bone Volume
- Trabecular Thickness
- Trabecular Separation (Tb.Sp) which is a measurement of the average distance between trabecula and is calculated as the diameter of the largest sphere which is entirely bounded within the solid surfaces.
- Trabecular Number, expressed as the number of trabeculae per unit length.

Evaluation and analysis of the histogram

One of the nineteen analyzed bone samples is used as example for the description of the method. From the microtomographic acquisition, 400 slices describing the sample are available. In order to obtain the total grey level histogram of the sample, a code in Labview was implemented. This code sequentially reads the input images and reading the grey level value assigned to each pixel of the image, it gives as output the number of pixels associated with each grey level. As can be shown in Figure 51, images are surrounded by a big region of white pixels which are useless for the sample analysis. Observing the histogram of a generic specimen, reported in the figure below, this region considerably affects the histogram increasing the value of grey level 255.

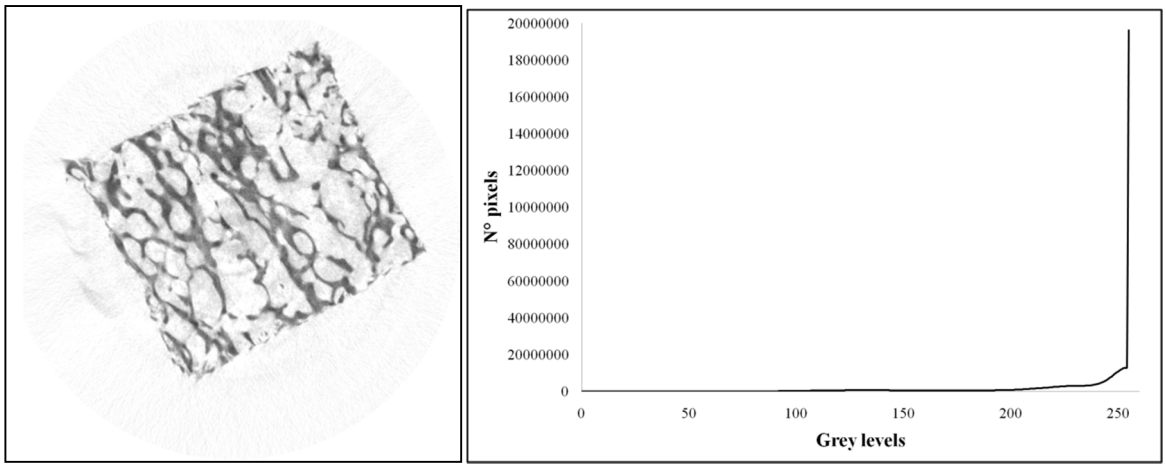

Figure 52. a) Slice of one of the trabecular bone specimens under investigation; b) Grey levels histogram of the specimen calculated considering all of the 400 slices of the specimen

The presence of this peak doesn't allow a good analysis of the histogram so another code has been implemented in LabVIEW in order to eliminate this region from the images. Also if the images are modified by this artifice, the result on the bone volume calculation is not affected because it is unquestionable that the grey level 255 is not representative of bone.

This region is eliminated by the first step of the code implemented rotating and cutting the images, as it is reported in the image below.

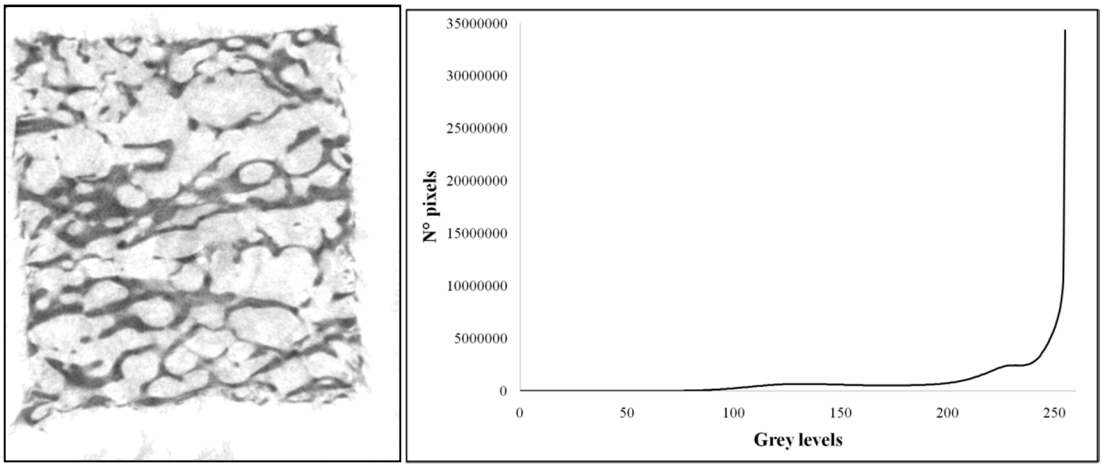

Figure 53. a) Slice of one of the trabecular bone specimens after the first elaboration, it has been rotated and cut; b) Grey levels histogram of the specimen calculated considering all of the 400 slices elaborated

Despite of this first elaboration, slices still present a very wide area of pixels of useless information so another elaboration is required. The second elaboration allows to surround the interesting area of the specimen and eliminate the remaining area without any loss of information. Pixels belonging to the not interesting area are transformed into white pixels.

In order to better understand this process, in the image shown in Figure 54these pixels are colored in black, rather than white.

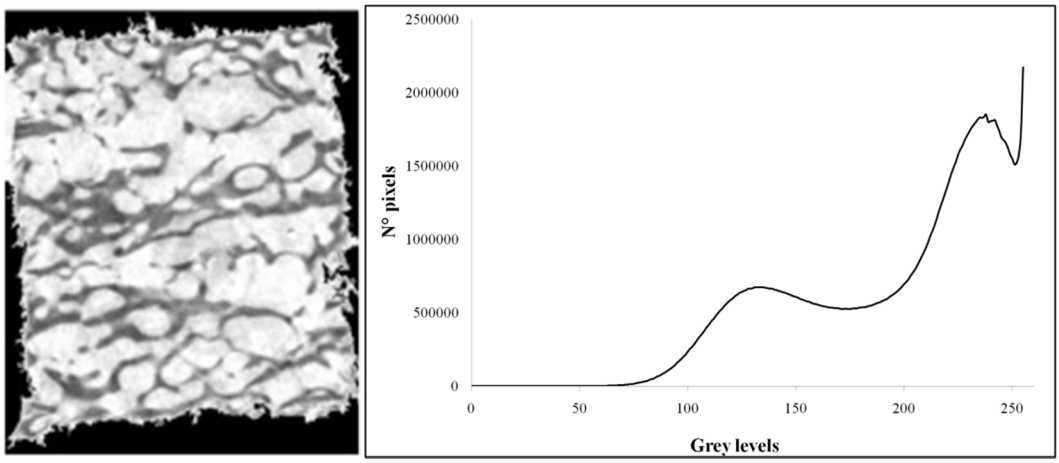

Figure 54. a) Slice of one of the trabecular bone specimens after the second elaboration; b) Grey levels histogram of the specimen calculated considering all of the 400 slices elaborated

As result of this processing, the curve representing "non-bone" population has been significantly limited because all the gray levels in the external zone due to the artifacts, lines of backprojection and noise are transformed into level 255. This is the reason of the peak in 255 and it can be eliminated limiting the histogram at the minimum value that precedes the peak value. In Figure 55 is reported the final histogram used for the subsequent analysis.

Figure 55. Grey levels histogram of the specimen object of the subsequent analysis. The peak at the level 255 has been eliminated since it is not useful for the analysis

Grey levels histogram analysis

As reported in the paragraph 4.3, from the image of a bone specimen, three regions can be distinguished: bone, empty space among trabeculae and a third border region representing pixels of the partial volume effect. This distinction is confirmed from the observation of the histogram in Figure 55.

From Laidlaw's theory, in regions containing a single material (bone or air in this case), the curve can be approximated to a Gaussian defined by the characteristic parameters "c" and "s", respectively the expected value and the standard deviation:

$$f_{single}(v, c, s) = \left(\prod_{i=1}^{n} \frac{1}{s_i\sqrt{2\pi}}\right) exp\left(-\frac{1}{2}\sum_{i=1}^{n}\left(\frac{v_i - c_i}{s_i}\right)^2\right) \quad (4.12)$$

where v_i, c_i and s_i are scalar component of v, c, s.v is the independent variable of the set of experimental data, in this case it represents the grey levels of the image so it varies from 0 to 255.

A region containing more than one material can be approximated by a curve which is the result of the superimposition of many normal distributions with the same standard deviation "s" and expected value ranging from the expected value of one material (c_{bone}) to the expected value of

the other material (c_{air}) in step "*dt*", where *t* is the percentage of the second material in the mixture:

$$f_{mixture}(v; c_1, c_2, s) = \int_0^1 f_{single}(v, (1-t)c_1 + tc_2, s)dt \quad (4.13)$$

These basis functions, which approximate the total histogram of the specimen, were calculated using the Levenberd-Marquardt algorithm[70]. It is a standard technique for solving problems with nonlinear least squares, which iteratively searches the minimum of a function expressed as a sum of squares of non-linear functions. Given a set of empirical data *(Xi, Yi)* and a set of input parameters, components of the vector *β*, the algorithm "LMA" works searching the optimal parameters such that the function approximating the experimental data *f(X; β)* minimizes the sum of the squared differences among the experimental measurement and the value assumed by the approximating function.

$$S(\beta) = \sum_i [Y_i - f(X_i, \beta)]^2 \quad (4.14)$$

Each parameter of the vector *β* is initially set to the value which is assumed to be the optimum, then the value of the parameters at each step is updated by the iterative process. The next step assumes a new value of *β = (β + δ)* and the new function will be:

$$f(X_i, \beta + \delta) \sim f(X_i, \beta) + J_i\delta \quad (4.15)$$

where J_i is the gradient of f respect to β:

$$J_i = \frac{\partial f(X_i; \bar{\beta})}{\partial \bar{\beta}} \quad (4.16)$$

Three different conditions can be established in order to stop the iterative process:

- The square error falls below a predefined limit "ε_1".
- The variation in δ between two consecutive steps is less than the limit established "ε_2".
- the maximum number of iterations.

The components of the vector *β* allows to find the functions of best fit. Then, assuming that these functions can be associated to Gaussian-like functions, the parameters required for their evaluation will be the expected value *c*, the standard deviation *s* and the amplitude *A*. The implemented code allows to find these parameters working separately on the two parts of the histogram so a limit among the maximums of the curves must be define. The maximum value is detected in both and consequently the amplitude and the mean value of the two Gaussians are found. The estimation of the standard deviation is a little more difficult and the process is different for the two distributions.

Considering a Gaussian, it is known that the 99.7% of the specimens is distributed in the range centered in the expected value μ and large six times the standard deviation σ. Because of the symmetry of the Gaussian, the 99.7% of the specimens of its first half is distributed in the range: $(\mu - 3\sigma) \div \mu$. The mean value μ is the x-axis value corresponding of the maximum of the curve, adding all the values from level *0* to level μ, the total number of specimens contained in the first half of the Gaussian is calculated. To calculate the number of samples in the range $0 \div (\mu - 3\sigma)$, this value must be multiply for 0.003. In this way the value of x-axis l which is 3σfar from the expected value μ is calculated. From the values μ and l, the standard deviation σ can be calculated as:

$$\sigma = \frac{(\mu - l)}{3}$$

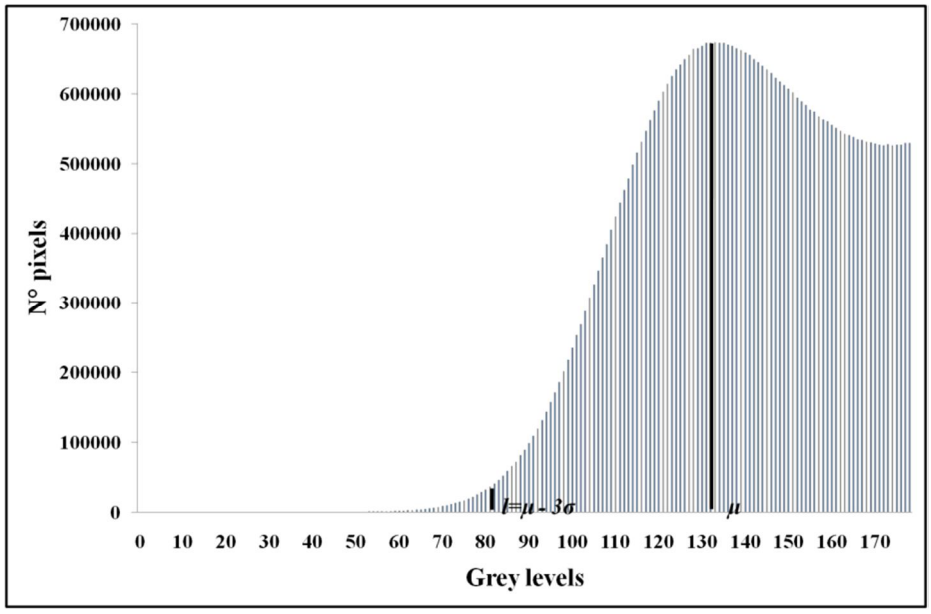

Figure 56. First part of the histogram considered for the calculation of the expected value, standard deviation and amplitude of the first distribution

This computation can be used for the first curve which is asymptotic to the x-axis, but not for the second curve. In this case, the computation of σ requires to take into account the Full Width at Half Maximum which is the 50% of the amplitude. Calculating its x-axis corresponding value l, the standard deviation is:

$$\sigma = \frac{(\mu - l \times 2)}{2.335}$$

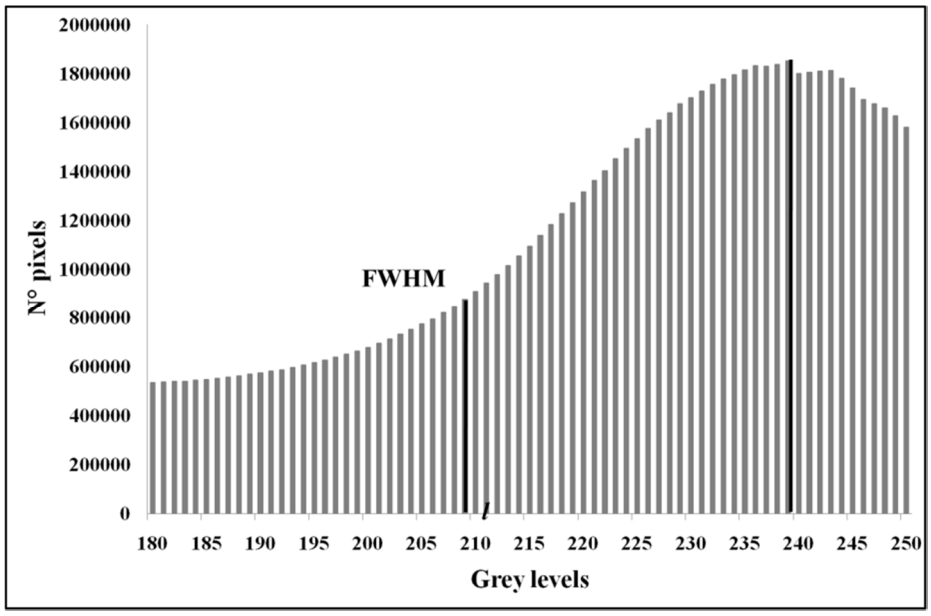

Figure 57. Second part of the histogram considered for the calculation of the expected value, standard deviation and amplitude of the second distribution.

The code implemented for the fitting of the histogram requires as input the original histogram and the set of β parameters, as results three curve representing the different distributions are available.

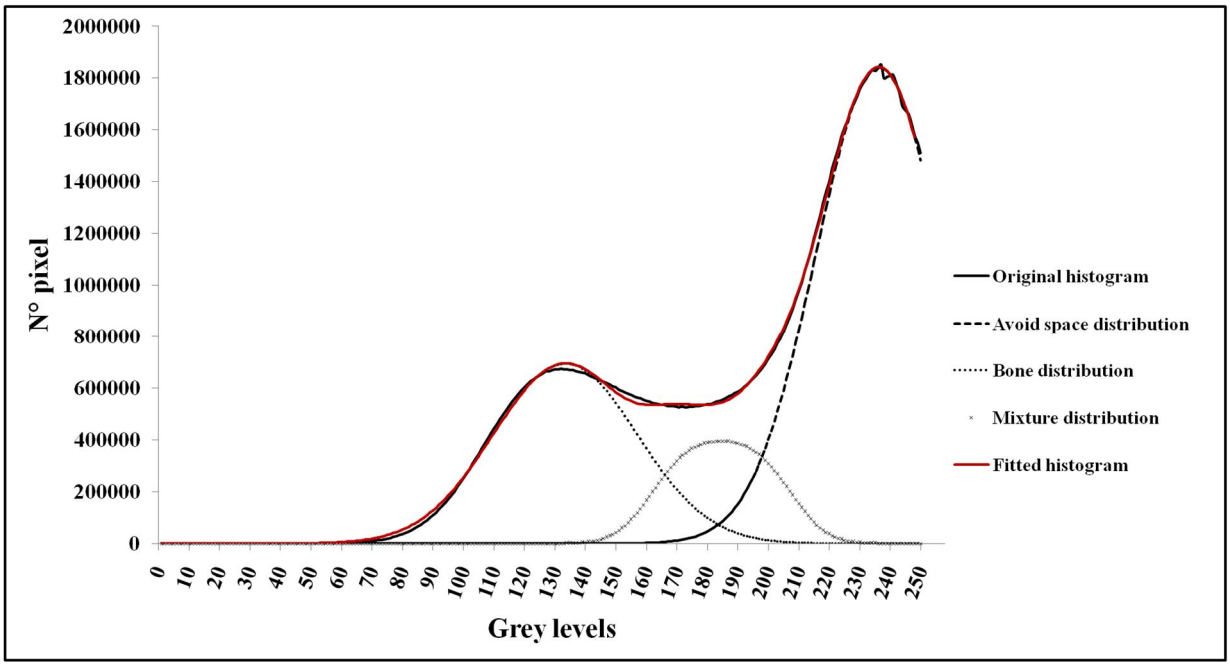

Figure 58. Results of the implemented code: original histogram, distributions of the three populations and the fitted histogram

Assuming that the third distribution represents the partial volume effect so pixels at the border region of bone and assuming that probabilistically they can be equally associated to bone or not, the number of pixels representing bone are calculated as the sum of pixels belonging to the bone distribution plus the 50% of pixels belonging to the third mixture distribution[71].

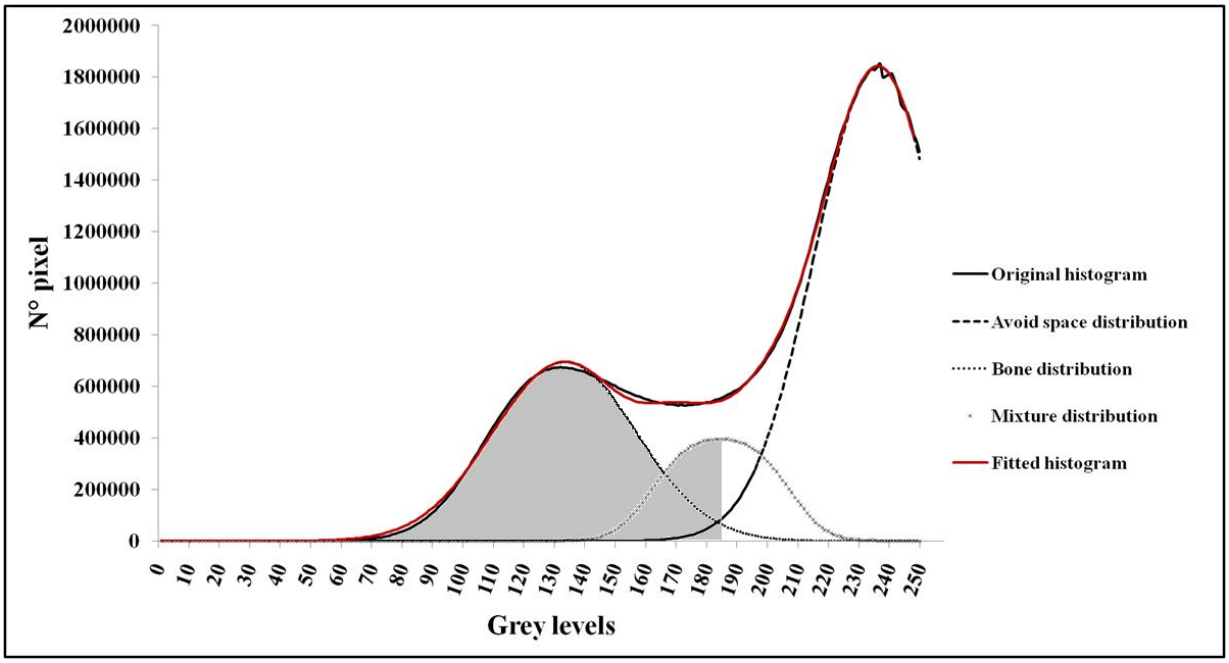

Figure 59. Calculation of the bone volume from the sum of the calculated distributions

4.4.2 Pycnometer as reference method for bone volume measurement

The characteristic porous structure of trabecular bone makes difficult the measurement of its volume. The helium pycnometer allows to obtain an accurate measurement, the volume of solid particles can be calculated with a relative standard uncertainty less than 0.25%[72]. The helium pycnometer requires the following assumptions:

- The behavior of helium is approximated to the behavior of an ideal gas.
- Samples are rigid.
- The pycnometer is waterproof, therefore the gas quickly reaches the condition of thermodynamic equilibrium.

If these conditions are satisfied, starting from the measure of the pressures involved, the "Ideal Gas Law" can be used to calculate the volume of the tested specimen.

An helium pycnometer is composed of:

1. A chamber containing the sample.
2. A chamber containing a piston.

3. A pressure transducer.

4. A valve that regulates the introduction of helium.

5. Pneumatic tubes for the interconnection of the various chambers.

All these components are placed in a temperature controlled chamber, the temperature is maintained constant so that the gas expansion or compression occurs isothermally.

The gas introduced comes from a pressurized environment, external to the chamber and fixed at a controlled temperature.

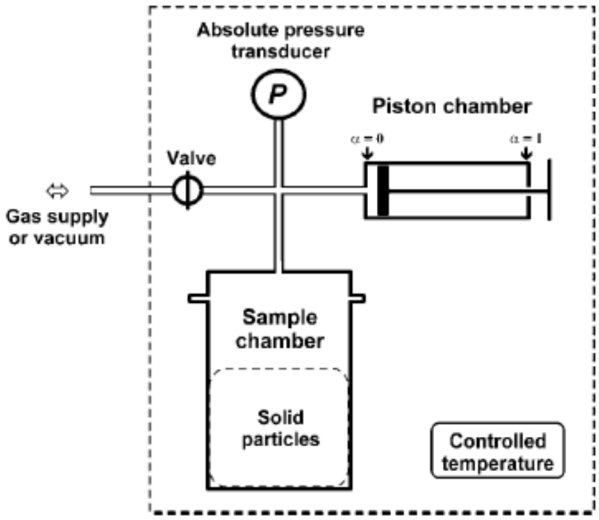

Figure 60. A schematic configuration of a gas pycnometer

The piston is initially placed in the position α_i. Opening the valve, the helium (He) enters in the chamber containing the specimen until the occupation of the entire available volume, including the volume provided by the microporosity of the trabecular bone tissue. The valve is then closed. After the time necessary for the gas to reach the equilibrium condition, the measurement obtained by the pressure transducer is used as a measure of the initial pressure P_i of the gas.

Maintaining the valve closed, the piston is placed in another position α_f. After once again the time required to reach equilibrium conditions, the measure obtained by the pressure transducer is the final pressure P_f of the gas.

The final pressure of the gas in the pycnometer is expressed by the relation:

$$P_f = P_i \left(\frac{T_f}{T_i}\right)\left(\frac{V_c - V_s + \alpha_i V_p}{V_c - V_s + \alpha_f V_p}\right) \quad (4.17)$$

where:

• Vc is the sum of the volume of the sample chamber, the internal volume of the pressure transducer and the volume of the tubes.

- *Vs* is the volume of the sample.
- *Vp* is the maximum volume offered by the piston chamber.
- $\alpha$is the index of the position assumed by the piston.
- *Ti* and *Tf* are severally the initial and final temperatures.

Assuming isothermal condition, the volume of the sample *Vs* is given from the relation:

$$V_s = V_c + V_p\tau \tag{4.18}$$

where:

$\tau = -\left(\frac{P_{min}}{P_{max}-P_{min}}\right)$, *Pmin = min(Pi, Pf)* and *Pmax = max(Pi, Pf).*

The expression of the final pressure P_f is obtained considering the law of Boyle-Mariotti in condition of constant temperature

$$PV = cost \tag{4.19}$$

$$P_iV_i = P_fV_fP_f = P_i\left(\frac{V_i}{V_f}\right) \tag{4.20}$$

Replacing: $\begin{cases} V_i = V_c - V_s + \alpha_i V_p \\ V_f = V_c - V_s + \alpha_f V_p \end{cases}$

$$P_f = P_i\frac{\left(V_c - V_s + \alpha_i V_p\right)}{\left(V_c - V_s + \alpha_f V_p\right)} \tag{4.21}$$

from which the volume of the sample is:

$$V_s = V_c + V_p\frac{\left(\alpha_i V_i - \alpha_f V_f\right)}{\left(P_i - P_f\right)} \tag{4.22}$$

4.4.3 Results

The implemented algorithm allows to fit each histogram with two Gaussian distributions and a distribution relative to the mixture. A typical histogram and the distributions for one of the analyzed specimens is reported in Figure 58.

As described above, volume of the specimens is calculated as the sum of voxels in the bone distribution plus the 50% of voxels of the third distribution. Volumes calculated by this method are reported in Table 2, together with those measured by the pycnometer (mean and standard deviation) and by implementing the Otsu algorithm for the definition of the threshold value.

Samples	Reference volume (Pycnometer)	Dev. st.	Computed volume (implemented method)	Percentage difference (pycnometer-implemented method)	Volume (Otsu algorithm)	Percentage difference (pycnometer-Otsu)
	mm^3	mm^3	mm^3	%	mm^3	%
Sample1	192.3	10.4	238.6	-24.1	80.7	58.0
Sample2	241.4	3.1	254.2	-5.3	70.3	70.9
Sample3	68.5	2.9	59.1	13.7	59.0	13.8
Sample4	280.2	2.6	291.8	-4.1	244.0	12.9
Sample5	480.7	4	547.8	-14.0	279.8	41.8
Sample6	436.9	2.8	311.5	28.7	197.2	54.9
Sample7	55.9	3.3	65.8	-17.8	40.9	26.9
Sample8	111.6	4.7	130.7	-17.1	69.9	37.4
Sample9	112.8	3.1	120.7	-7.0	55.6	50.7
Sample10	146.9	2.4	165.8	-12.9	71.0	51.6
Sample11	93.7	3	110.8	-18.3	41.4	55.8
Sample12	65.1	1.5	52.6	19.1	27.2	58.2
Sample13	70.3	1.2	85.4	-21.4	33.4	52.5
Sample14	105.9	1.5	100.4	5.2	50.1	52.7
Sample15	161.5	4	165.5	-2.5	61.2	62.1
Sample16	84.1	2.9	99.4	-18.2	50.5	40.0
Sample17	93.7	0.9	82.6	11.9	63.3	32.4
Sample18	67	0.4	66.2	1.2	35.8	46.6
Sample19	96.7	1.7	93.7	3.2	33.9	65.0

Table 2. Volume calculated with different method: pycnometer, new method implemented and Otsu algorithm

Comparing these values, an excellent correlation can be established between volumes calculated with the implemented method and the pycnometer measurements, an angular coefficient of the linear equal to 0.956 shows a slight underestimation of computed vs. measured volume.

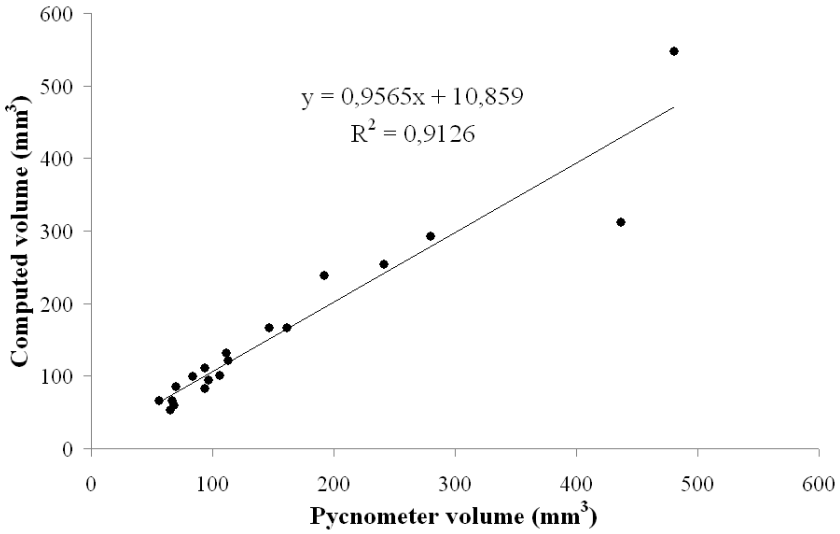

Figure 61. Correlation between reference value measured by the pycnometer and volumes calculated with the new method

Conversely, the comparison of volumes calculated binarizing images with the threshold value calculated by Otsu algorithm implementation yield an heavy underestimation, that is 50% of the volumes measured by pycnometer.

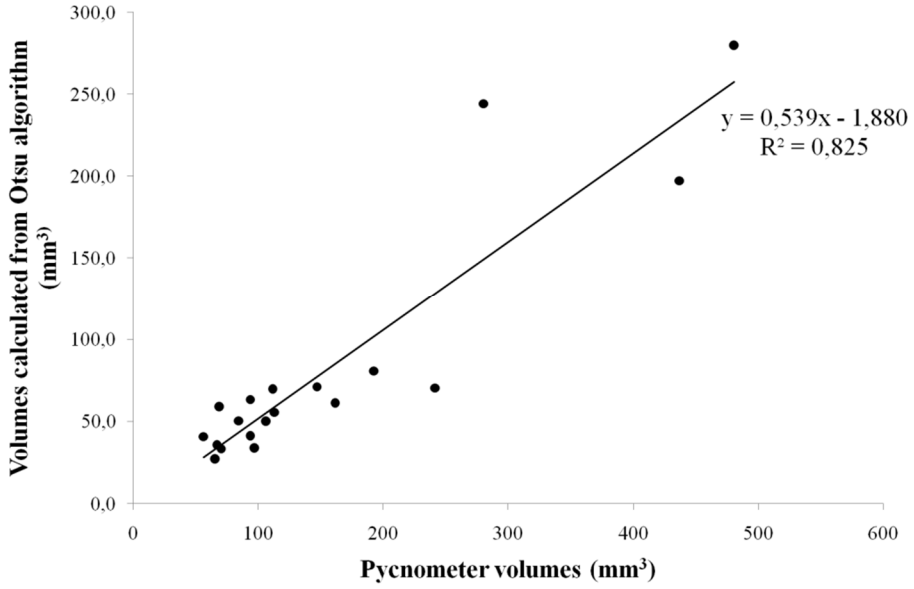

Figure 62. Correlation between reference value measured by the pycnometer and volumes calculated with the implementation of Otsu algorithm for the threshold definition

The accuracy of the implemented method for the calculation of bone samples volume has been verified comparing the obtained volumes with those resulting from the implementation of the Otsu algorithm. An example of the comparison of the three measurements is reported in the graph in Figure 63.

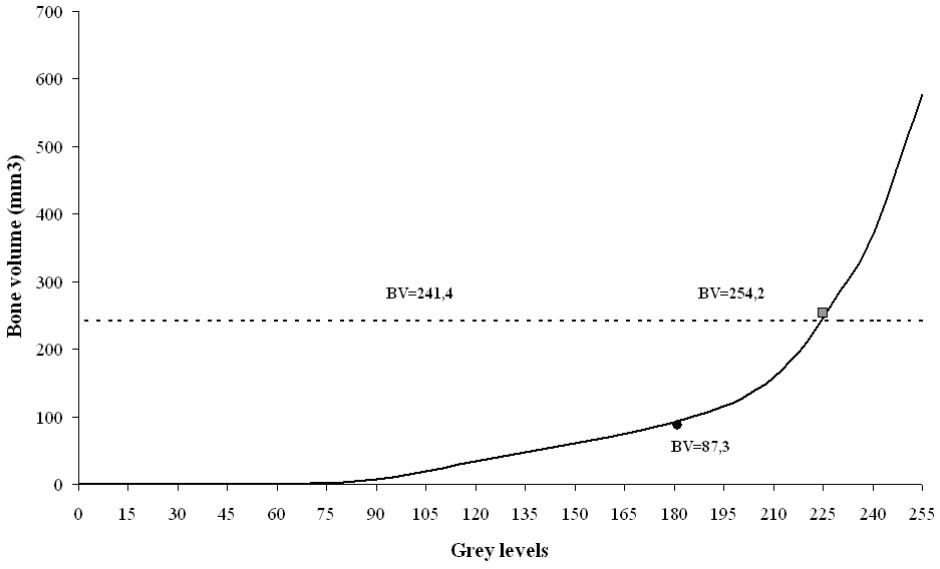

Figure 63. Comparison of volume values calculated with pycnometer (dotted line), implementation of Otsu algorithm (black circle) and the method object of this study (grey square)

Considering the value obtained by pycnometer as reference, it can be observed that the volume calculated with this new method is more accurate than the other method.

After that, since the Micro-CT allows to obtain histomorphometric parameters of the specimens, the relation between values of trabecular separation and trabecular density with the bone volume values is evaluated.

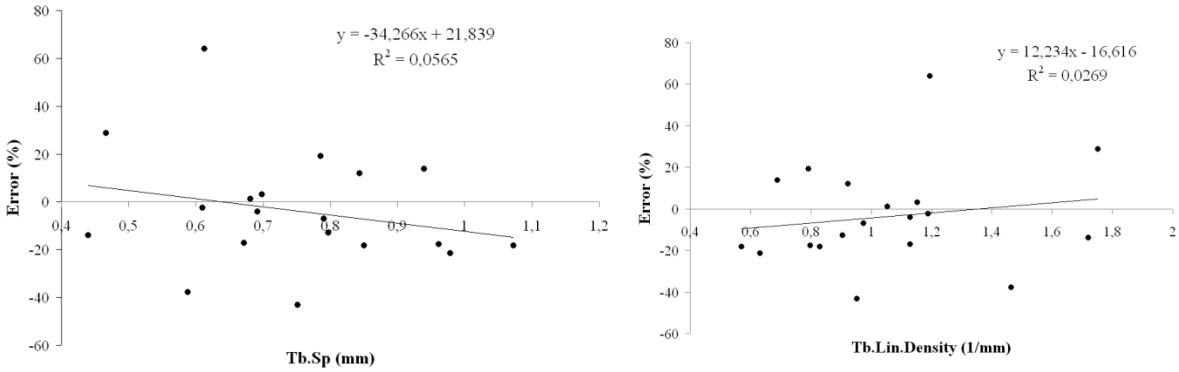

Figure 64. Correspondance between percentage error of the new method respect to the pycnometer values and trabecular parameters of bone samples: Trabecular separation and Trabecular Linear Density

The results of this evaluation, reported in Figure 64, show a none significant correspondance between the percentage error and the parameters that describe the bone architecture.

Both of the methods focus on the histogram analysis, however the Otsu method leads to define a threshold for the image processing, this new method avoids the problem of the threshold definition allowing to extract bone volumetric information directly from the histogram.

The measurement of this parameter directly from the Micro-CT images could be useful in many studies on bone, such as the analysis of bone diseases or a widely comprehension of bone morphometric characterization but the main advantage of this new method is the possibility of a non invasive measure of bone volume. This characteristic could be important for in-vivo studies on laboratory cavies.

CHAPTER 5

Numerical simulation of the bone remodeling process

Bone is a structural material, but unlike traditional structural materials, bone is a living tissue subjected to a process of continuous remodeling. The remodeling process is necessary in order to make bone capable of adapting to its environment and in particular to external load. Wolff[73] has been the first who affirmed that internal structure of bone is strongly related to external forces. Trabecular bone achieved its main function, mechanical load transfer, by the optimization of its internal structure under the influence of external forces. The trabecular architecture of cancellous bone varies and trabeculae arranged in the direction of the principal mechanical loads in order to better support loads. It is known that an intensive load causes an increase in bone mass[74], conversely a reduced load or, mostly the inactivity, a decrease in bone mass[75]. Moreover, an excessive loss of bone, such as in pathologies like osteoporosis, leads to an increasing fracture risk. Osteoporosis is a pathology of high incidence in the population so understanding the adaptive behavior of bone tissue under environmental load is an important issue in order to prevent osteoporosis and to improve physical and pharmaceutical treatment methods, as well as prosthetic designs. Different approach can be used to improve the knowledge in bone behavior. In vivo experiments allow to obtain useful information, nevertheless they are hard to control and they allow to study only the earliest stages of adaptive responses. The most significant processes occur in months or even years so an alternative approach was found in the implementation of computer simulations.

5.1. State of art

The mass and geometry of bone is greatly determined by its loading environment. A change in bone's loading environment leads the bone tissue to adapt, possibly changing its shape and

itsdensity. Many numerical models based on the use of a mechanical signal for the subsequent change in bone density or geometrical properties. Differences in models can be found in the choice of the mechanical signal considered or in the choice of the parameter used for the description of the adaptation.

Fyhrie and Carter developed a mathematical theory describing the relationship between cancellous bone apparent density, trabecular orientation, and stress. The optimization of two mechanical signals: strain energy density and strength allows to predict both trabecular orientation and apparent density[76].

Carter et al expanded the study of a single loading condition to a multiple loading condition, analyzed by bone in vivo experiments. Three different bone maintenance criteria are studied: continuum model effective stress, continuum model fatigue damage accumulation density, and bone tissue strain energy density. All of these criteria showed a similar mathematical form which allows to relate density and mechanical load. The same model can be applied to many different situations of growth, functional adaptation, injury, and aging of connective tissues[77].

Beauprè et al developed computer simulations using two-dimensional finite element models to simulate the bone remodeling starting from a solid structure of homogeneous bone density. The simulation of normal loading condition confirms an increase in bone mass, then a subsequent reduction in the loading conditions allowed to demonstrate the incidence of bone atrophy. Results of both the conditions showed that similar stress-related phenomena are responsible for both normal morphogenesis and functional adaptation in response to changes in the bone loading[78].

Huiskies et al [79]used Finite Element Model in combination with numerical formulations of bone remodeling theories to predict stress-related adaptive bone behavior, in accordance with Wolff's Law. The mechanical signal used as a feed-back control variable to determine density changes in bone has been the Strain Energy Density (SED):

$$U = \frac{1}{2}\varepsilon_{ij}\sigma_{ij}$$

The Strain Energy Density is obtained from the strain tensor ε_{ij} and the local stress tensor σ_{ij}.The difference between SED calculated and an homeostatic equilibrium SED is used as the driving force for adaptive activity. The relation between the adaptive rate and the mechanical signal SED is defined following a suggestion from Carter (1984)[80], which assumed that bone is lazy in a certain range of mechanical stimulus so in this region there isn't a linear relation between load and material properties.

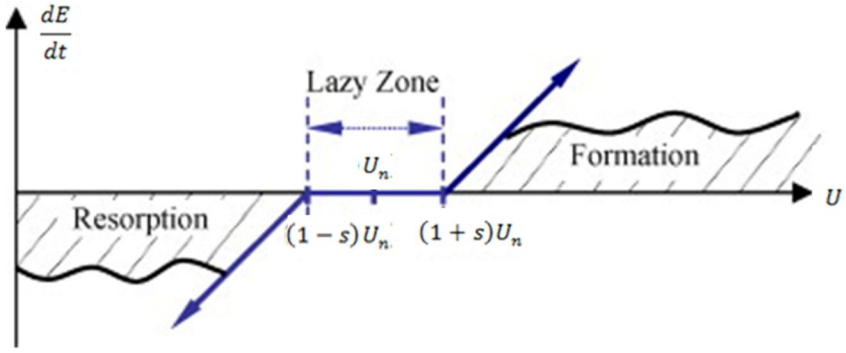

Figure 65. Lazy zone of bone: region in which there isn't reaction of bone to external mechanical stimuli

This implies to consider three different conditions for the adaptive rate-stress relation:

$$\frac{dE}{dt} = \begin{cases} C_e(U-(1+s)U_n), & U > (1+s)U_n \\ 0, & (1-s)U_n \le U \le (1+s)U_n \\ C_e(U-(1-s)U_n), & U > (1+s)U_n \end{cases}$$

E is the Young Modulus, C is a constant, U is the actual Strain Energy Density and U_n is the equilibrium Strain Energy Density.

Mullender [81] used a cell based model to describe the self-organizational bone regulation process. Osteocytes are considered as sensors of the mechanical stimulus and they react producing a stimulus for the bone mass regulation, which diminishes exponentially with the distance of the sensor position. Considering bone composed of N sensor cells, uniformly distributed on its volume, each sensor measures the strain energy density per unit of mass in its position:

$$S_i = \frac{U_i}{\rho_i}$$

The density in each cell $\rho(x,t)$is function of the signal measured from the other cells and the distance of these cells from the position x

$$\frac{d\rho(x,t)}{dt} = \tau\Phi(x,t)$$

τ is the time constant regulating the rate adaptive process and:

$$\Phi(x,t) = \sum_{i=1}^{N} f_i(x)(S_i - k)$$

k is the reference value for the Strain Energy Density and $f_i(x) = e^{-[d_i(x)/D]}$is the spatial function. The variation of the density ρ is limited by a maximum value ρ_{max} and it is related to the Young Modulus according to the relation suggested by Rice (1988)[82]:

$$E(x,t) = C\rho(x,t)^{\gamma}, \qquad C, \gamma \text{ are constants}$$

Results obtained starting from an initial density situation showed transformation in bone morphology according to Wolff's Law[83].

5.2. Methods

This chapter presents a method for using control theory and finite element analysis to simulate shape and density adaptations in bone. A combination of two software programs are employed: MATLAB (Version R2010a, The MathWorks Inc., Natick,MA), that is a numerical coding program widely used in engineering research, and COMSOL Multiphysics (Version 3.5, COMSOL Inc., Burlington, MA) used for the finite element analysis (FEA). COMSOL was chosen over other FEA packages for its ability to simultaneously solve multiple physics problems. The interfacing of these two software allowed to develop the model.

The first step of the simulation is a finite element analysis on an initial situation. After the definition of structure information: geometry, material properties, boundary conditions and loading conditions, stresses and strains have been calculated. The stress calculated is used as input for the control process of adaptation. The remodeling rules used to control adaptation are adjusted based on the theories reported in the paragraph above. Results of this first analysis have been used as input of specially algorithm written in MATLAB code to implement the equations of the remodeling. At each iterative step, Strain Energy Density is used to change the density of the structure.

Assuming osteocytes as the bone cells which detect the mechanical stimulus and react causing local material adaptation, the model is composed of N cells representing osteocytes. Each cell is characterized by an apparent density value which is update at each step, depending on the mechanical stimulus sensed by the cell. The relation stress-material property is defined by the following formula:

$$\frac{d\rho}{dt} = C_{\rho}(SED - SED^{*}) \qquad for \quad \rho < \rho_{max} \tag{5.1}$$

Where C_ρ is a constant, *SED* is the strain energy density measured by each sensor cell and the reference value *SED** is calculated as the average *SED* of the initial condition.

The Young Modulus E of each cell is calculated as a power of the apparent density ρ, according to the following formula:

$$E = C\rho^{\gamma} \tag{5.2}$$

where C is a constant of proportionality and γ is a constant that can assumed value 2 or 3. The value 3 is chosen according to Mullender[81].

In a subsequent analysis, the idea of consider the influence of the neighboring cells expressed by Huiskies. et all[83]is considered. In this case, the relation regulating the bone remodeling process becomes :

$$\frac{d\rho(x,t)}{dt} = \tau \sum_{i=1}^{N} e^{-[d_i(x)/D]}(SED_i - SED^*) \qquad for \quad \rho < \rho_{max} \tag{5.3}$$

The model implemented was tested in a two-dimensional plate model. A compressive load distribution of 10 N/mm^2, decreasing linearly over the top edge is considered. Bone is considered isotropic, characterized by an initial uniform density distribution equal to 870 Kg/m^3. The maximum value for the density is set to 1740 Kg/m^3 and the time constant value for τ is 1(Kg m^{-3})^2/(MPa time-unit). The D parameter, regulating the influence of neighboring sensors, is set at D=0.025 mm.

The same analysis has been done on a more realistic model of a femur. A radiographic image of a human femur has been analyzed by a proper code developed in MATLAB in order to extrapolate the structure of the femur. In this case too, the model has been divided in 1286 cells in order to simulate the presence of the osteocytes sensor cells. The external forces were chosen to represent the monopodal stance phase and were obtained from biomechanical calculations: the load changes over the weight-bearing area according to a cosine function of the polar angle (Figure 66)[84][85][86][87].

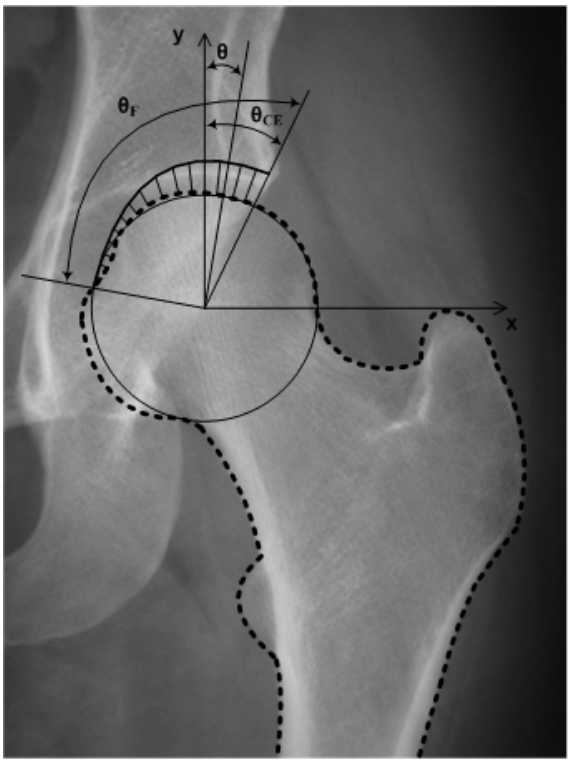

Figure 66. Radiographic image utilized for modeling the healty femur together with the load distribution and angles according to Brinckmann 2002, Nordin & Frankel 2001, Van Rietbergen 2003. The dashed line indicates the femur's contour drawn extrapolated for the FE analysis.

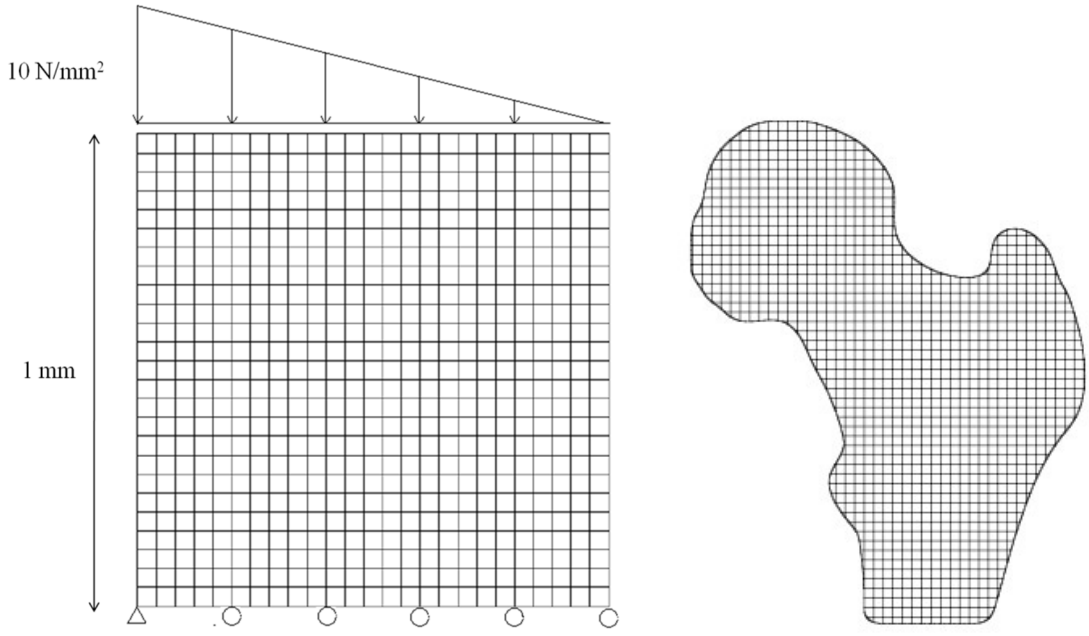

a) b)

Figure 67. a)Two-dimensional bone structure of 1x1 mm (40 μm thick) discretized in 625 sensors cells and subjected to a compressive load; b)Bone femur structure discretized in 1286 sensors cells and subjected to a compressive load.

5.3. Results and conclusions

The first configuration of a square structure composed of 625 cells has been analyzed implementing two different remodeling process. The first one changes the density, and consequently the elastic modulus, of each sensor cell considering the difference between the Strain Energy Density sensed by the cell and the average SED calculated from the initial condition. The second remodeling process has been implemented considering the adaptation of each cell density including the influence of SED sensed from the neighboring cells.

The bone structure, initially considered homogeneous and isotropic, after the application of the compressive load becomes heterogeneous and anisotropic. Moreover, the second simulation shows a more accurate description of the trabeculae arrangement in the sense of Wolff's law.

In the first simulation, one hundred and fifty iterations have been required to converge to the stable configuration reported in Figure 68. The second simulation requires less iterations than the first one, after one hundred iterations the structure achieved the stability.

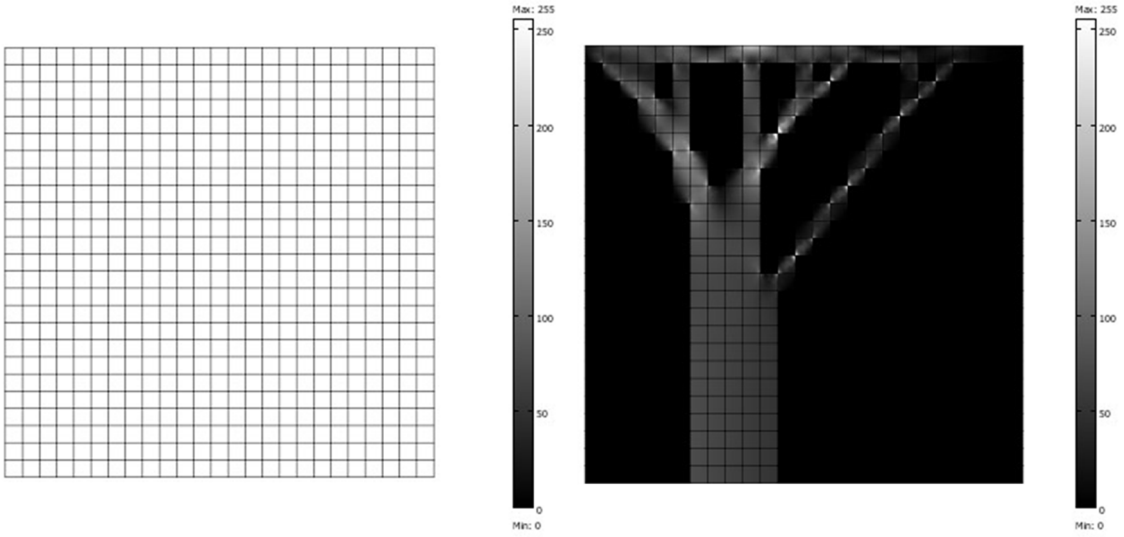

Figure 68. Initial mass distribution with density value of 870 Kg/m^3 and final stable configuration of trabecular arrangement after compressive load. On the left is reported the color legend. The grey value 255 corresponds to the maximum density value set at 1740 Kg/m^3, the minimum value 0 corresponds to the minimum density value set at 17.4 Kg/m^3.

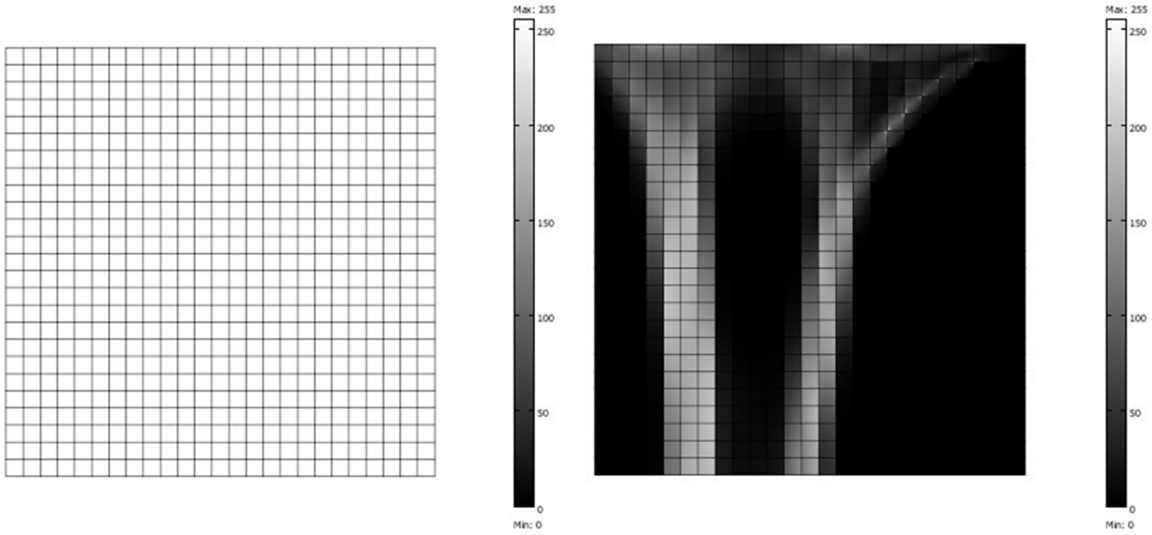

Figure 69. Initial mass distribution with density value of 870 Kg/m^3 and final stable configuration of trabecular arrangement after compressive load. On the left is reported the color legend. The grey value 255 corresponds to the maximum density value set at 1740 Kg/m^3, the minimum value 0 corresponds to the minimum density value set at 17.4 Kg/m^3. The spatial influencing parameter D is set at 0.025 mm.

In Figure 70 is reported the trabecular arrangement stable configuration for the femur model. The same initial uniform density value equal to 870 Kg/m^3 has been defined and also in this case, one hundred iterations allows to achieve the stability.

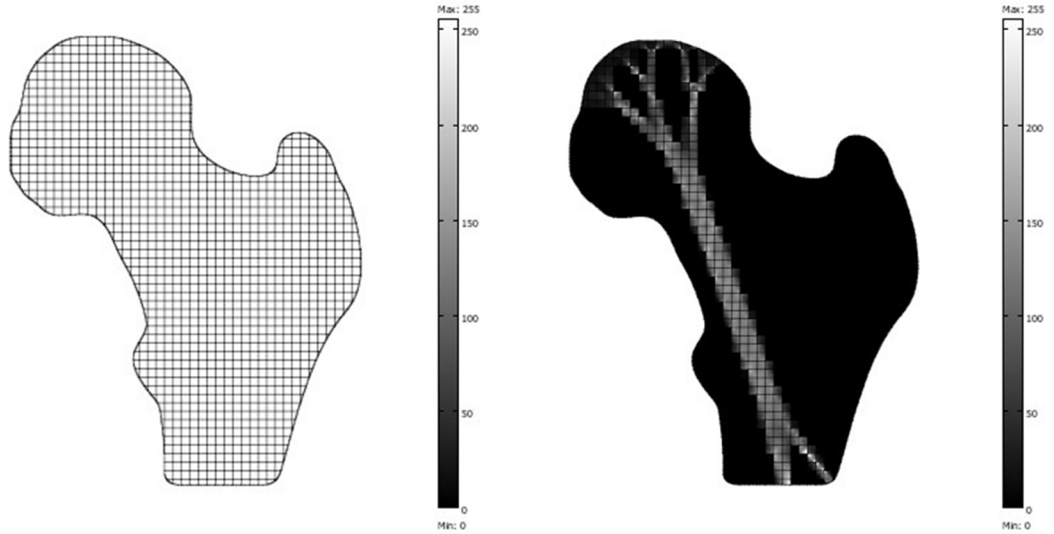

Figure 70. Initial mass distribution with density value of 870 Kg/m^3 and final stable configuration of trabecular arrangement after compressive load. On the left is reported the color legend. The grey value 255 corresponds to the maximum density value set at 1740 Kg/m^3, the minimum value 0 corresponds to the minimum density value set at 17.4 Kg/m^3.

CONCLUSION

Osteoarthritis and osteoporosis are bone diseases of high incidence in the population. The reduced quality of life for those with osteoporosis is enormous. Osteoporosis can result in disfigurement, lowered self-esteem, reduction or loss of mobility, and decreased independence. Because of the importance of this topic, in the last years many studies worked on the bone morphometric characterization in the prediction of these diseases. Hystomorphometry has been the traditional technique for bone characterization for many years. It is a good technique despite it requires the damage of samples analyzed. In the last years, the emergence of the microtomographic technique, drives many researchers on improve this new and non invasive technique on bone characterization.

The bone characterization by Micro-CT is based on extrapolate parameters from a post-processing of the images. This process requires a first step, called binarization, which consists on the definition of a proper grey level threshold value to distinguish bone from background. The definition of this threshold is a crucial point because, despite this topic has been the subject of many studies, an accurate procedure to define it is not available yet. In order to overcome the threshold problem in CT images, the main goal of this study is the definition of a new method for the bone volume calculation.

Before dealing with this issue, an accurate study on the system under investigation has been done. This first study allowed the optimization of the system for the bone analysis. Firstly the resolution of the Skyscan 1072 has been studied. A good method for the resolution measurement of an imaging system is the calculation of its Modulation Transfer Function. MTF can be measured by the derivative and the subsequent Fourier Transform of the Edge Spread Function. The measurement of the ESF required the Micro-CT acquisition of a proper edge device. This phantom has been constructed in plexiglass and aluminium in order to severally simulate the attenuation coefficient of biological tissue and bone. From the MTF, the focal spot size of the system has been calculated and a good correlation has been found with the value declared from the Skyscan. The second step of this study has been focused on the analysis of artifacts that usually affect Micro-CT images. One of the main and difficult artifact is the beam hardening. It causes visual distortions on images and also problem on the parameters quantifications. In order to properly correct the effect of beam hardening in the subsequent analysis of bone samples, a disc of Hydroxyapatite has been the object of this study. A Skyscan software dedicated for the reconstruction of the images, based on Feldkamp algorithm, allows the correction of this effect by choosing a proper parameter. To demonstrate the accuracy of this correction and properly

choose this parameter, the back-projection algorithm has been implemented in LabVIEW (Version 8.2). The comparison of this two software for the correction of beam hardening showed a good correlation in the results and found the same optimum value correspondent to the 50% of correction. Hydroxyapatite is the main component of bone so the same value of beam hardening correction is considered in bone subsequent analysis.

After the optimization of the system for bone analysis, to achieve the main goal of this study which is the bone volume calculation of the samples, nineteen samples of bone cube, extracted from femoral heads of eight patients subject to a hip arthroplasty surgery, were acquired by theMicro-CT apparatus Skyscan 1072. The implemented algorithm extrapolates bone volumetric information by the analysis of the grey level histogram of the reconstructed images. Volume values of the samples were also calculated with an Helyum pycnometer, taken as a reference. Moreover, in order to compare the accuracy of this new method with one of the method based on the definition of a threshold, the Otsu algorithm for the detection of the threshold has been implemented in Labview (Version 8.2) and the relative volumes have been calculated. A better correlation between the new method and the pycnometer datasets were demonstrated, respect to the Otsu datasets. The histogram processing can be defined a viable method for an accurate and non destructive bone volume calculation. The measurement of this parameter directly from the Micro-CT images could be useful in many studies on bone, such as the analysis of bone diseases or a widely comprehension of bone morphometric characterization but the main advantage of this new method is the possibility of a non invasive measure of bone volume. This characteristic could be important for in-vivo studies on laboratory cavies.

The last part of the research has been dedicated on implementing a numerical simulation of bone remodeling process. It is known that bone mass and trabecular architecture adapt respect to the external forces in order to make bone capable to support mechanical loads associated with daily activities. How the characteristics of external loads are sensed in the bone, and how they are translated to structural adaptation of the tissue is a bone complex research topic. This study required the combination of two software: COMSOL Multiphysics (Version 3.5, COMSOL Inc., Burlington, MA) for the Finite Element Analysis and MATLAB (Version R2010a, The MathWorks Inc., Natick,MA) for the implementation of the iterative process. Two different models have been implemented in this study, firstly a simple two-dimensional based-cell model composed of 625 cells where each cell has been treated as a sensor able to sensed the mechanical stimulus and react changing its material properties (density and Young Modulus) and then a two-dimensional model of a femur, extrapolated from the radiographic image of human femur. Both

the model shown the relation between trabecular morphology and mechanical external load and subsequent density of sensor cells. The case of monopodal load has been implemented in this research, future developments of the model could interest the simulation of other load case, such as the microgravity condition. Understanding how bone reacts in microgravity condition is an important issue since it can be useful for the definition of therapeutic strategy.

REFERENCES

[1]. Canalis E et al. *Growth factors and the regulation of bone remodeling*. J Clin Invest; 81: 277, 1988

[2]. Marotti G. *The structure of bone tissues and the cellular control of their deposition*. Ital. J. Anat. Embryol.; 101: 25, 1996

[3]. Marks SC, Popoff SN. *Bone cell biology: regulation of development, structure and function in the skeleton.* Am. J. Anat.; 183: 1, 1988

[4]. Little K. *Bone behaviour*. Academic Press , New York , USA , 1973

[5]. Horton W. A. *The biology of bone growth*. Growth Genet. Horm.; 6(2):1–3,1990

[6]. Bruder S P, Caplan A I. *Cellular and molecular events during embryonic bone development.* Connect. Tissue Res.;20:65–71. 1989

[7]. Hatori M, Klatte K J, Teixeira C C, Shapiro I M. *End labeling studies of fragmented DNA in avian growth plate: Evidence for apoptosis in terminally differentiated chondrocytes*. J. Bone Miner. Res.;10:1960–1968.1995

[8]. Owen M. *Histogenesis of bone cells*. Calcif Tissue Res; 25: 205, 1978.

[9]. Keller T. S.,2, Mao Z., Spengler D. M. *Young's modulus, bending strength, and tissue physical properties of human compact bone*. Journal of Orthopaedic; 8(4):592-603. 1990

[10]. Internal Fixation in Osteoporotic Bone. Yuehuei H. An

[11]. C.Cowin*Bone Mechanics Handbook*. New York Washington, DC.

[12]. Hahn M, Vogel M, Pompesius-Kempa M, Delling G *Trabecular bone pattern factor, a new parameter for simple quantification of bone microarchitecture*. Bone; 13: 327-330. 1992

[13]. Odgaard A *Three-dimensional methods for quantification of cancellous bone architecture*. Bone; 20 (6): 315-328. 1997

[14]. Parfitt AM, Drezner MK, Glorieux FH, Kanis JA, Malluche H, Meunier PJ, Ott SM, Recker RR *Bone Histomorphometry: standardization of nomenclature, symbols and units.* Journal of Bone and Mineral Research; 2 (6): 595-610.1987

[15]. Marcus R, Majumder S. *The nature of osteoporosis.* In: Marcus R, Feldman D, Kelsey J (Ed.). Osteoporosis. 2. ed. San Diego: Academic Press; p. 3-17.2001

[16]. McNamra LM, Prendergast PJ, Schaffler MB. *Bone tissue properties are altered during osteoporosis.* J Mus Neur Inter; 5:342-3.2005

[17]. National Collaborating Centre for Chronic Conditions (UK). Osteoarthritis. National clinical guideline for care and management in adults. London: Royal College of Physicians (UK); 2008. (NICE Clinical Guidelines, No. 59).

[18]. Patel V, Issever AS, Burghardt A, Laib A, Ries M, Majumdar S. *Micro-CT evaluation of normal and osteoarthritic bone structure in human knee specimens.* J Orthop Res; 21(1):6-13.2003

[19]. Sambrook P, Naganathan V. *What is the relationship between osteoarthritis and osteoporosis?* BaillieresClinRheumatol;11(4):695-710.1997

[20]. Cicuttini F, Wluka A, Davis S, Strauss BJ, Yeung S, Ebeling PR. *Association between knee cartilage volume and bone mineral density in older adults without osteoarthritis.* Rheumatology;43(6):765-9.2004

[21]. Dougherty G. *Quantitative CT in the measurement of bone quantity and bone quality for assessing osteoporosis.* Med EngPhys;18(7):557-68.1996

[22]. Legrand E, Chappard D, Basle MF, Audran M. *Evaluation of trabecular microarchitecture. Prospects for predicting the risk of osteoporosis and fracture.* Rev RhumEngl Ed 1999;66(11):543-7.

[23]. Ding M, Odgaard A, Hvid I. *Changes in the three-dimensional microstructure of human tibialcancellous bone in early osteoarthritis.* J Bone Joint Surg Br;85(6):906-12.2003

[24]. Fazzalari NL, Parkinson IH. *Femoral trabecular bone of osteoarthritic and normal subjects in an age and sex matched group.* Osteoarthritis Cartilage;6(6):377-82.1998

[25]. Parfitt AM, Mathews CH, Villanueva AR, Kleerekoper M, Frame B, Rao DS. *Relationships between surface, volume, and thickness of iliac trabecular bone in aging and in osteoporosis. Implications for the microanatomic and cellular mechanisms of bone loss.* J Clin Invest;72(4):1396-409.1983

[26]. Chappard C, Peyrin F, Bonnassie A, Lemineur G, Brunet-Imbault B, Lespessailles E, Benhamou CL. *Subchondral bone micro-architectural alterations in osteoarthritis: a synchrotron micro-computed tomography study.* Osteoarthritis Cartilage;14(3):215-23.2006

[27]. Lemaire, V., Tobin, F.L., Greller, L.D., Cho, C.R., and Suva, L.J. *Modeling interactions between osteoblasts and osteoclasts activities in bone remodeling,* J. Theoretical Biology, 229, pp. 293–309, 2004.

[28]. Maldonado, S., Borchers, S., Findeisen, R., and Allgower, F., *Mathematical Modeling and Analysis of Force Induced Bone Growth,* Proceedings of the 28th IEEE, EMBS Annual International Conference, New York City, USA, Aug. 30 to Sept. 3, 2006.

[29]. James A. Pennline *Simulating Bone Loss in Microgravity Using Mathematical Formulations of Bone Remodeling* Glenn Research Center, Cleveland, Ohio.

[30]. The Essential Physics of Medical Imaging . Di Jerrold T. Bushberg

[31]. Branca F.P., *Fondamenti di ingegneria clinica. Volume 1*. Sprinter-Verlag Italia, Milano 2000

[32]. Bedini R., Ioppolo P., Pecci R., Filippini P., Chiazza S., Bianco A., Columbro G., *Osservazioni di osso equino al microscopio elettronico a scansione e alla microtomografia 3D.* Roma: Istituto Superiore di Sanità; 2005 (Rapporti ISTISAN, 05/37).

[33]. Principles of CT and CT Technology. Lee W. Goldman

[34]. Computed Tomography: Principles, Design, Artifacts, and Recent Advances. Jiang Hsieh

[35]. Computerised Micro-tomography: Non-invasive Imaging and Analysis of Biological Samples, with Special Reference to Monitoring Development of Osteoporosis in Small Animals. Volume 656 di Linköping University medical dissertations

[36]. Dal Pozzo G. *Compendio di tomografia computerizzata e TC spirale*. Torino: 1999

[37]. Branca F.P., *Fondamenti di ingegneria clinica. Vol*.2 Sprinter-Verlag Italia, Milano 2008

[38]. Kak A. C. & Slaney M. *Principles of computerized tomographic imaging*. New York, USA, IEEE Press 1999

[39]. Feldkamp, L.A., Davis, L. C. & Kress, J.W. *Practical cone-beam algorithm*. J. Optic. Soc. Am. A 1, 612-619.1984

[40]. Barret, J.F. and Keat, N., *Artifacts in CT: Recognition and Avoidance*. Radiographics 24(6), 1679-1691. 2004

[41]. Brooks R. A. & Di Chiro G. *Beam hardening in x-ray reconstructive tomography*. Phys. Med. Biol. 1976

[42]. Herman G. T. *Correction for beam hardening in computed tomography*. Phys. Med. Biol. 1979

[43]. Sijbers, J. and Postnov, A., *Reduction of ring artefacts in high resolution micro-CT reconstructions.* Physics in Medicine and Biology 49(14).2004)

[44]. Hsieh J. Image artifacts: appearances, causes and corrections. Computed tomography: principles, design, artifacts and recent advances. Bellingham, Wash: SPIE Press, 2003; 167-240.

[45]. Seeram E. Image quality. Computed tomography: physical principles, clinical applications and quality control. 2nd ed. Philadelphia, Pa: Saunders, 2001; 174-199.

[46]. Micro-Computed Tomography for the Evaluation of Bone Architecture Gopinath Mani, Biomedical Engineering, The University of Texas at San Antonio/The University ofTexas Health Science at San Antonio.

[47]. H. Illers, E. Buhr, S. Gu¨nther-Kohfahl, U. Neitzel. *Measurement of the modulation transfer function of digital x-ray detectors with an opaque edge-test*. Vol. 114, Radiation Protection Dosimetry, Nos 1-3, pp. 214–219.2005

[48]. S.Dorè , R.E. Kearney. *Experimental evaluation of computerised tomography point spread function variability within the field of view: parametric models*. Med. Biol. Eng. Comput., 42, pp. 591-597.2004

[49]. Trefler M. Gray J. E. *Characterization of the imaging properties of x-ray focal spots*. Applied Optics.Vol. 15, No. 12, pp. 3099-3104. 1976.

[50]. Groh G. Klotz E. Weiss H. *Simple and Fast Method for the Presentation of the Two-Dimensional Modulation Transfer Function of X-Ray Systems.* Applied Optics, Vol. 12, Issue 7, pp. 1693-1697. 1973

[51]. Samei E. Flynn M.J. Reimann D. A. *A method for measuring the presampled MTF of digital radiographic systems using an edge test device*. Michigan. 1997. 88

[52]. Illers H. Buhr E. Günther-Kohfahl S. Neitzel U. *Measurement of the modulation transfer function of digital x-ray detectors with an opaque edge-test device*. Radiation Protection Dosimetry. Vol. 114, Nos 1-3, pp. 214–219.2005

[53]. Buhr E. Günther-Kohfahl S. Neitzel U. *Accuracy of a simple method for deriving the presampled MTF of a digital radiographic system from an edge image*. Med. Phys. 30, 2323–2331. 2003

[54]. D. A. Reimann, V. Chaudhary, M.J. Flynn, and I.K. Sethi. *Parallel Implementation of Cone-Beam Tomography*. International Conference on Parallel Processing, II, pp. 170-173. 1996.

[55]. J. Muller-Merbach, "*Simulation Of X-Ray Projections For Experimental 3D Tomography*" ISSN 1400-3902 Report No. LiTH-ISY-R-1866, March 31, 1996.

[56]. A. Shih, G. Wang, P. Cheng, *Fast algorithm for X-ray cone-beam micro-tomography*. Microscopy and Microanalysis, 7, pp.13–23, January, 2001.

[57]. I. Goddard, M. Trepanier. *High-speed cone-beam reconstruction: an embedded systems approach.* Proc. SPIE Vol. 4681, p. 483-491, Medical Imaging 2002: Visualization, Image-Guided Procedures, and Display, Seong K. Mun; Ed.

[58]. N. Sorokin, "An FPGA-based 3D Backprojector," Dissertation, Universität des Saarlandes, 2003.

[59]. T. Lei, W. Sewchand, "Statistical approach to X-ray CT imaging and its application in image analysis", IEEE on Medical Imaging, 1992.

[60]. A. Odgaard. *Three dimensional methods for quantification of cancellous bone architecture*. Bone, 1997.

[61]. S. Schweizer, et al. "Preparation and characterization of calibration standard for bone density determination by micro-computed tomography", The Analyst, 2007.

[62]. A. A Postnov, et al. *Quantitative Analysis of Bone Mineral Content by x-ray Micro-tomography*, INSTITUTE OF PHISICS PUBLISHING, Phisiol. Meas. 24, pp. 165-178.2003

[63]. A. Nazarian, et al. *Quantitative Micro-Computed Tomography: A non-invasive method to assess equivalent bone mineral density*. Bone. 43; pp. 302-311.2008

[64]. Marinozzi F., Marinozzi A., Bini F., Zuppante F., Pecci R., Bedini R. *Variability of morphometric parameters of human trabecular tissue from coxo-arthritis and osteoporotic samples.* Ann. Ist. Super.Sanità; 48(1):19-25. 2012

[65]. Tan Y., Kiekens K., Kruth, Voet A., Dewulf W. 2011. *Material Dependent Thresholding for Dimensional X-ray Computed Tomography. International Symposium on Digital Industrial Radiology and Computed Tomography* - Mo.4.3.

[66]. Ding M., Odgaard A., Hvid I. *Accuracy of cancellous bone volume fraction measured by micro-CT scanning*. J. Biomechanics;32(3):323-6.1999

[67]. Kim C. H., Zhang H., Mikhail G., von Stechow D., Muller R., H. Kim H., Guo X. E. *Effects of thresholding techniques on micro-CT-based finite element model of trabecular bone*. Journal of Biomechanical Engineering;129(4):481-6.2007

[68]. D. H. Laidlaw, K. W. Fleisher, A. H. Barr. *Partial Volume Bayesian Classification of Material Mixtures in MR Volume Data Using Voxel Histograms.* IEEE TRANSACTION ON MEDICAL IMAGING [VOL.17, NO.1]; pp. 74-86.1998

[69]. Bedini R, Marinozzi F, Pecci R, Angeloni L, Zuppante F, Bini F, Marinozzi A. *Analisi microtomografica del tessuto osseo trabecolare: influenza della soglia di binarizzazione sul calcolo dei parametri istomorfometrici*. Roma: Istituto Superiore di Sanità; 2010 (Rapporti ISTISAN, 10/15).

[70]. Manolis I. A. Lourakis. *A Brief Description of the Levenberg-Marquardt Algorithm Implemened by levmar*. Institute of Computer Science Foundation for Research and Technology 2005;Crete, GREECE.

[71]. Marinozzi F., Bini F.,Zuppante F., Bedini R., Marinozzi A., Pecci R.*Bone volume measurement of human femur head specimens by modeling the histograms of micro-CT images.* Paper presented at CompImage 2012 – Computation Modeling of Objects Presented in Images: Fundamentals, Methods and Applications; 3rd Edition, Rome.

[72]. Tamari S., Aguilar-Chávez A. *Optimum design of the variable-volume gas pycnometer for determining the volume of solid particles*. Meas. Sci. Technol.; 15:1146-1152.2004

[73]. Wolff, J., 1986. The Law of Bone Remodeling, Berlin: Springer-Verlag.

[74]. Courteix, D., Lespessailles, E., Loiseau Peres, S., Obert, P., Germain, P. and Benhamou, C.L. *Effects of physical training on bone mineral density in prepubertal girls: a comparative study between impact-loading and non-impact-loading sports.* Osteopor. Int., 8, pp 152-158. 1998

[75]. Zerwekh J.E., Ruml L.A., Gottschalk F. & Pak C.Y.C. *The effects of twelve weeks of bed rest on bone histology, biochemical markers of bone turnover, and calcium homeostasis in eleven normal subjects*. J.Bone Min. Res. 13, pp 1594-1601. 1998.

[76]. Fyhrie DP, Carter DR. *A unifying principle relating stress to trabecular bone morphology*. J Orthop Res.;4(3):304-17. 1986

[77]. Carter DR, Fyhrie DP and Whalen RT. *Trabecular bone density and loading history: Regulation of connective tissue biology by mechanical energy*. J Biomech. 20,785-794. 1987

[78]. Beaupré GS, Orr TE and Carter DR. *An approach for time-dependent bone remodeling-theoretical development*. J Orthop. Res., 8(5), 651-661. 1990b

[79]. Huiskes R, Weinans H, Grootenboer HJ, Dalstra M, Fudala B and Slooff TJ. *Adaptive bone-remodeling theory applied to prosthetic-design analysis.* J Biomech 20:1135-1150. 1987

[80]. Carter DR. *Mechanical loading histories and cortical bone remodeling*. Calcif. Tissue Int., 36 (Suppl.I), S19-24. 1984

[81]. Mullender M.G., Huiskes R. and Weinans H. *A physiological approach to the simulation of bone remodeling as a self-organizational control process*. J. Biomechanics, Vol. 27, No. 11: 1389-1394. 1994

[82]. Rice J. C., Cowin S. C. and Bowmann J. A. *On the dependance of the elasticity and strenght of cancellous bone on apparent density*. J. Biomechanics 21,155-168. 1988

[83]. Weinans H., Huiskes R. and Grootenboer H.J.*The behavior of adaptive bone-remodeling stimulation models.* J. Biomechanics 25, 1425-1441. 1992

[84]. Brinckmann P., Frobin W., Leivseth G. *Muscoloskeletal Biomechanics*. Thieme. 2002

[85]. Nordin M. &Frankel V.H. *Basis Biomechanics of the Muscoloskeletal System*. Lippincott Williams&Wilki; 3th edition. 2001

[86]. Van Rietbergen B., Huiskes R., Eckstein F., Rùegsegger P. *Trabecular bone tissue strains in the healty and osteoporotic human femur.* Journal of Bone and Mineral Research 18(10):1781-1788.2003

[87]. Marinozzi F., De Paolis A., De Luca R., Bini F., Bedini R., Marinozzi A. *Stress and strain patterns in normal and osteoarthritis femur using finite element analysis.* Paper presented at CompImage 2012 – Computation Modeling of Objects Presented in Images: Fundamentals, Methods and Applications; 3rd Edition, Rome.